Highly Sensitive Rb Magnetometer for Neutron Electric Dipole Moment Experiments

by

Moushumi Das

A thesis submitted to the Faculty of Graduate Studies of
The University of Manitoba
in partial fulfillment of the requirements of the degree of

Master of Science

Department of Physics and Astronomy
University of Manitoba
Winnipeg

Acknowledgements

I would like to thank my advisor Dr. Jeff Martin, for his help and support during graduate studies.

I am grateful to Dr. Russell Mammei, Dr. Chris Bidinosti and Dr. Blair Jamieson for their valuable suggestions during my research work.

I would also like to thank David Ostapchuk, Michael Loren Lang, Taraneh Andalib and Wolfgang Klassen for their conversation and assistance around the lab during the course of my research.

Abstract

A non-zero neutron electric dipole moment (nEDM) would indicate time-reversal and charge-parity violation. Our collaboration is developing an experiment at TRIUMF to improve the sensitivity to the nEDM by one order of magnitude (10^{-27} e·cm). I developed a highly sensitive magnetometer based on nonlinear magneto-optical rotation (NMOR) in Rb vapour. In the future such magnetometers will serve in an array to form an auxiliary magnetometer system monitoring the stability and uniformity of the magnetic field in the nEDM experiment. The operation of the magnetometer in a free-induction-decay mode was the focus of this thesis. The precision of the field measurement, drifts over time, impact of degaussing, and measurements of transverse fields were studied using the magnetometer.

Contents

List of Figures

Chapter 1

Introduction

This chapter will provide some information on why the neutron electric dipole moment (nEDM) is interesting to measure. Finding a nonzero nEDM would answer questions regarding the matter-antimatter or baryon asymmetry of the universe (BAU). The measurement principle of nEDM experiments and the origin of systematic effects causing false EDM signal. will be explained. This will lead to a discussion on the importance of magnetometry on nEDM experiment.

1.1 CP violation and the Standard Model

Charge conjugation (C), Parity (P) and Time-reversal (T) symmetry are discrete symmetries in physics. C-symmetry describes the symmetry of physical laws under a particle-antiparticle transformation. P-symmetry describes the inversion of spatial coordinates and T-symmetry the direction of time.

CPT-symmetry is believed to be a good symmetry of nature because all relativistic quantum field theories are invariant under successive application of the three discrete symmetries. This is known as the CPT theorem[1].

Parity symmetry was discovered to be violated in the weak interaction through observations of spin correlations in beta-decay. This is due to neutrinos having a particular

handedness. This problem can be fixed proposing that CP-symmetry is a good symmetry of nature. However, CP-symmetry has also been found to be violated in weak decays of kaons and B-mesons [2].

The nEDM is an observable that if found to be non-zero, would indicate a violation of T-symmetry. Assuming the CPT theorem, this is equivalent to CP-violation. The current best measurement of the nEDM gives the upper bound $|d_n| < 3.0 \times 10^{-26}$ e·cm [3, 4]. We now discuss how this result impacts physics within and beyond the standard model.

CP violations in the standard model are arising from two separate sources. The first source is found in the strong interaction, described by the θ term in the quantum chromodynamics (QCD) Lagrangian. This CP violating term in the QCD Lagrangian violates both parity and time symmetry and induces a nEDM of $|d_n| \sim -(0.9 - 1.2) \times 10^{16}\theta$ e·cm [5] with θ being a dimensionless parameter of the standard model. A combination of nEDM and Hg-EDM measurements limit the parameter to be very small $\theta \lesssim 10^{-10}$. The reason for the smallness of θ is currently unknown and this is sometimes called the strong CP problem. The second source of CP violation in the SM arises from a complex phase in the Cabibbo-Kobayashi-Maskawa (CKM) matrix [2, 6]. The phase is responsible for CP violation in K and B meson decays. the CP violation with in the CKM matrix predicts $|d_n| = 10^{-31} - 10^{-32}$ e·cm, well below the current best experimental limit stated above.

1.2 New Physics and the Baryon asymmetry

The T-violating nEDM is considered to be a promising probe for physics beyond the Standard Model, a broad variety of scenarios [7]. Some theories try to make a consistent description of the nEDM and baryogenesis, the origin of the baryon asymmetry in the universe [5].

According to the Big Bang theory, matter and antimatter have been created in equal amounts in the early universe. But the present universe is overwhelmingly made up of matter rather than anti-matter. The amount of baryon asymmetry generated in the standard model

is much smaller than current observations, in the scenario of electroweak baryogenesis [8].

The Sakharov conditions describe a way to explain the evolution of a baryon asymmetry from an initial symmetric condition [9, 10].

- Baryon number violation.
- Violation of C and CP symmetry.
- Interactions away from thermal equilibrium

Although all of these ingredients are available in the standard model in principle, the underprediction of electroweak baryogenesis motivates extensions to the standard model to increase the amount of CP violation in an attempt to fix electroweak baryogenesis. These same new physics scenarios often predict a non-zero nEDM because of the increased CP violation.

1.3 Neutron electric dipole moment and CP violation

Neutron has an intrinsic electric dipole moment (EDM). The neutron EDM is a measure for the distribution of positive and negative charges inside the neutron [5]. The intrinsic EDM of neutrons interacting with external magnetic and electric fields can be described by the following Hamiltonian:

$$H = -\vec{\mu}_n \cdot \vec{B} - \vec{d}_n \cdot \vec{E}, \tag{1.1}$$

where μ_n is the magnetic moment of the neutrons interacting with the magnetic field B, and d_n is the electric dipole moment of the neutron interacting with the electric field E. Since the neutron spin is an axial vector and the electric dipole moment is a vector quantity, both vectors behave differently under P- or T-transformations. The orientation of the electric dipole moment changes under P operation but leaves the magnetic moment unchanged. On the other hand, T-operation affects the spin vector but leaves the electric dipole moment

unchanged. Because of the conservation of CPT symmetry, a non-zero electric dipole moment of the neutron would be a violation of parity (P) and time-reversal (T) symmetry.

1.4 nEDM measurement principle

Ramsey's method of separated oscillatory fields [11] is used to extract the nEDM. In the nEDM experiment, ultracold neutrons (UCN) whose spins are oriented along a uniform magnetic field are stored in a chamber. An electric field is applied parallel to the magnetic field. Using a series of loadings of the cell with neutrons, and application of magnetic pulses followed by polarized UCN detection for each cell loading, the spin-precession (Larmor) frequency of the neutrons is determined.

$$h\nu^{\uparrow\uparrow} = 2\mu_n B + 2d_n E, \tag{1.2}$$

where the arrows are meant to indicate the parallel orientation of the B and E fields. The electric field direction is then reversed and the spin-precession frequency measured again:

$$h\nu^{\uparrow\downarrow} = 2\mu_n B - 2d_n E. \tag{1.3}$$

By taking the difference of the two frequency measurements, the nEDM d_n may be deduced. A serious concern is that if the magnetic field drifts during the frequency measurement, the difference of the two measurements will suffer from a systematic error. Even in the best magnetic environment, field drifts of 1-10 pT over the ∼100 s (per UCN fill) measurement period are likely. In order to make a correction that is more precise than neutron counting statistics, precision magnetometers must be used to measure the magnetic field, correcting these drifts at the level of 10-20 fT level over the same period [12].

1.5 Magnetometry Impact on nEDM

Our collaboration is developing comagnetometers based on ^{199}Hg and ^{129}Xe. My work is on the development of alkali atom (Rb or Cs) magnetometers that will be placed around the nEDM measurement cell. In this section I discuss the important properties of the magnetometry strategy for the nEDM experiment which motivate my work on the alkali atom magnetometers.

1.5.1 Comagnetometer

To correct for magnetic field drifts, the previous best experiment (done at ILL) developed a ^{199}Hg comagnetometer [3, 13]. The ILL EDM spectrometer was moved to PSI and several improvements to the comagnetometer system were made [14].

In the comagnetometer, optical pumping is used to polarize a vapor of mercury atoms which are then leaked into the nEDM measurement cell with the neutrons. After the application of a $\pi/2$ pulse, the atoms start to precess freely around B. The polarized mercury atoms precess in the same volume as the neutrons, hence probing the same space and time-averaged magnetic field. Circularly polarized probe light interacts with precessing atoms and the modulation of light transmission occurs at the Larmor frequency of the atoms. The statistical precision can correct 1-10 pT drifts in B to the required level of precision [14].

1.5.2 Systematic errors and False EDM's

While the comagnetometer is excellent at normalizing slow magnetic field drifts, it was discovered relatively recently that it introduces a potentially devastating systematic error which arises in part due to magnetic inhomogeneities [15]. When precessing particles (neutrons or ^{199}Hg atoms) are confined in the measurement cell in the presence of a magnetic inhomogeneity, there is an electric-field dependent shift on their measured Larmor resonance frequency. Since it is dependent on E, this gives rise to a false EDM signal.

The effect is easiest to understand by considering transverse fields originating from the gradient of a slightly non-uniform $\vec{B}$ field in the axial direction ($\partial B_z/\partial z$). Because $\vec{\nabla}\cdot\vec{B} = 0$, this gives rise to a nonzero radial component to the field B_r. In the presence of E, the species experience an additional magnetic field their rest frame

$$\vec{B}_v = \frac{\vec{v}\times\vec{E}}{c^2}, \tag{1.4}$$

where $\vec{v}$ is the velocity vector. If we consider a particular neutron or atom that bounces around the edge of the cell, circulating in the horizontal plane, $\vec{B}_v$ will also be oriented in the horizontal direction. In the rest frame of the particle, this will give rise to a circulating magnetic field. The rotation frequency of radial field is the same frequency as particles move in the EDM cell. The rotating field, although generally far off-resonance with the NMR frequency of the particle, nonetheless induces a tiny shift on the measured resonant frequency. The shift induced by the far non-resonant field is known as a Ramsey-Bloch-Siegert shift [11, 16], and its strength goes as the square of the rotating field to leading order. The cross-term in the square leads to the problematic frequency shift that reverses sign with E, hence giving a false EDM.

Both the ^{199}Hg atoms and the neutrons experience this effect. In the case of the UCN, they are moving so slowly that the process is adiabatic, and is therefore related to geometric phases in the same way as Berry's phase [14].

But the false EDM is generally larger for the ^{199}Hg atoms because of their larger (thermal) velocity. The method developed at ILL to correct for this problem uses the height difference between the UCN and comagnetometer atoms to measure the vertical gradient by the difference of their frequencies compared to the ratio of gyromagnetic ratios (which has been measured very precisely [17]) [3, 4].

Our collaboration is pursuing multiple alternate ways of coping with the false EDM. One of these is the dual comagnetometer concept based on ^{199}Hg and ^{129}Xe. By taking a particular

combination of the ^{199}Hg and ^{129}Xe precession frequencies, the false EDM can be cancelled out [18]. Another method we are pursuing is to use two separate EDM measurement cells that are stacked vertically. By comparing precession frequencies in the top and bottom cells, the vertical gradient can also be accessed.

Finally, we plan to measure gradients by placing a number of precision alkali magnetometers around the nEDM cell. It is this application that relates most to this thesis. This method of gradient determination has been shown by the PSI group to correctly sense the false EDM signal of Hg [19].

1.5.3 Internal alkali atom magnetometers

Based on the considerations above, the alkali atom magnetometers surrounding the nEDM measurement cells have two principal goals:

1. Determine the magnetic field to a statistical uncertainty competitive with the Hg comagnometer over the timescale of the frequency cycle measurement, i.e. measure to the statistical precision of 10-20 fT in 100 s. The field measurement should also be systematically robust, i.e. it should only respond to changes in B and not be susceptible to any other drifts.

2. Determine the homogeneity of the magnetic field, with a particular focus on the largest gradient term in the false EDM, which arises due to $\partial B_z/\partial z$. The typical scale of the gradient is expected to by 0.1-1 nT/m in the experiment. Drifts in the gradient should also be considered.

This thesis relates primarily to the first goal of developing a magnetometer system and characterizing carefully its precision and reducing the potential for any possible systematic errors or drifts. This is based on a prototype system previously reported in Ref. [20], but with several improvements. The technology relies on nonlinear magneto-optical rotation

(NMOR) of the plane of polarization of incident light in an atomic vapour, and it will be discussed in more detail in the next chapter.

The technology is very similar to devices developed for the planned Munich-ILL nEDM experiment [21]. It is somewhat technically different from the PSI nEDM experiment, which uses radio frequency (RF) atomic magnetometers, or magnetometers operated in the Mx configuration. [22].

An advantage of our strategy is that our NMOR magnetometers require only light and atoms to operate. In this sense our technique is "all-optical" i.e. requiring no RF. A concern with our technology choice is whether it can reach the required statistical precision and a principal result of this thesis is that it can. Aside from this, we also pursued a strategy being developed by the PSI and Munich group which uses free-induction decay, where all pumping (either light or RF) is switched off during the precision frequency measurement phase.

The principal contribution of this thesis work is therefore studies of the precision and long-term stability of all-optical NMOR-based magnetometers, operated using a free-induction-decay technique.

Chapter 2

Atomic Magnetometry

In the following chapter, there will be given an introduction into the quantum mechanical structure and interactions of a Rb atom with special focus on the hyperfine structure and the Zeeman splitting of the energy levels in an external magnetic field. In the second section of this chapter, the principle of atom-light interactions including optical pumping will be explained. After introducing basic concepts of alkali atom quantum mechanics, the phenomenology of nonlinear magneto-optical rotation (NMOR) will be discussed, which is the basis for the operation of an atomic magnetometer as it will be used for the nEDM setup.

2.1 Atomic structure of Rb

Alkali-metal atoms have single electron in their outer shell. For this reason they are often used for optical pumping. All sable alkali isotopes have a nuclear spin. Because of the nuclear spin the energy level of these alkali atom becomes complicated. The ground state structure of the Rb atom is $n = 5$, $L = 0$ (s-state) and $j = 1/2$, i.e, $5^2S_{1/2}$. The lowest excited states ($L = 1$) are the $5p$ states. According to quantum theory of angular momentum these $5p$ states have total electron angular momentum $J = L + S$ where L is the orbital angular momentum and S is the electron spin angular momentum. Fine structure splitting occurs due to spin orbit coupling. The lowest excited states $5P$ ($L = 1, S = 1/2$) split into $5^2P_{1/2}$

and $5^2P_{3/2}$ due to the fine structure splitting. The hyperfine structure is a result of the coupling between J and the total nuclear angular momentum I. The total atomic angular momentum F is then given by $F = J + I$ and the magnitude of F must lie in the range $J - I \leq F \leq J + I$.

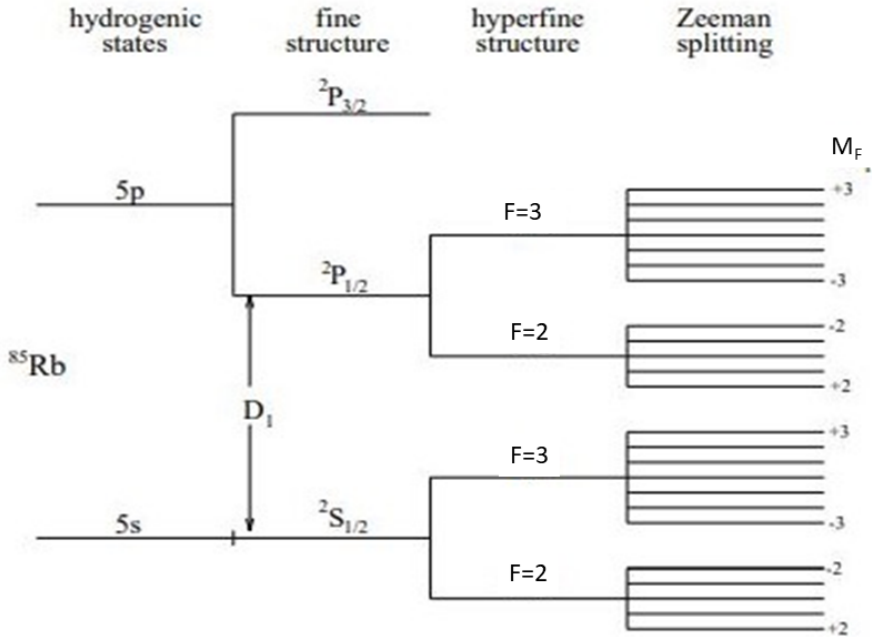

Figure 2.1: Energy level splitting of the ground state and first excited state of ^{85}Rb. The fine structure splits the first excited state into levels with $J = 1/2$ and $J = 3/2$, and the hyperfine structure further splits the energy levels due to the nonzero nuclear spin. The splittings are not drawn to scale [23]

.

For the ground state of ^{85}Rb, $J = 1/2$ and $I = 5/2$, so $F = 3$ or $F = 2$. And for the excited state $5^2P_{1/2}$ which has nuclear angular momentum $I = 5/2$ and $J = 1/2$ the allowed values of F are 3 and 2. The atomic energy levels are shifted according to the value of F. In quantum mechanics, a set of rules tell us the allowed transition between states which are known as selection rules. The rules are that the total orbital angular momentum change should be $\Delta L = \pm 1$ and the change in magnetic quantum number should be $\Delta M_L = 0, \pm 1$. According to selection rules the transitions from the state $L = 0$ to $L = 1$ are possible. Transmission corresponding to the energy difference between the $5^2S_{1/2}$ and $5^2P_{1/2}$ levels of rubidium is termed the D1 line; its wavelength is roughly 795 nm [24]. The $5^2P_{3/2}$ state

is separated from the $5^2S_{1/2}$ state by an energy corresponding to 780 nm wavelength, it is called the D2 line. Our Rb atomic magnetometer is based on exciting the D1-line transition by optical pumping. Linearly polarized laser beam is used to induce transitions of electrons from one energy level to another via optical pumping. In this case, the laser beam is tuned to the transition frequency and of sufficient power to perturb the equilibrium distribution of the ground state energy levels. The gyromagnetic ratio of ^{85}Rb is 4.667415 Hz/nT [17].

2.2 Linear and nonlinear magneto-optical rotation

In the presence of an axial magnetic field, when a linearly polarized light passes through an atomic medium the plane of polarization rotates. This kind of effect is known as the Faraday effect. A resonant enhancement of the Faraday rotation has been discovered by D. Macaluso and O. M. Corbino in 1898 which is known as nonlinear magneto-optical rotation (NMOR) or nonlinear Faraday rotation [25]. Consider an example system of $F = 1$ to $F' = 0$ transition (Fig 2.2). Linearly polarized light can be decomposed into two counter-rotating circularly polarized components $\sigma^{\pm}$. The transferable angular momentum is +1 for left circular polarization, -1 for right circular polarization.

In the absence of a magnetic field, the $M = \pm 1$ sublevels are degenerate and the optical resonance frequencies for the two circular polarizations coincide. But in the presence of magnetic field the Zeeman sublevels $M = \pm 1$ shift in energy by an amount $g\mu B/\hbar$ where g is the Land'e factor and μ is the Bohr magneton. This Zeeman splitting therefore leads to a difference between the resonance frequencies for for σ^+ and σ^- light. The left circularly polarized light experiences refractive index n_+ and the refractive index for right circularly polarized light is n_-. In this case, optical rotation arises due to the difference in the refractive index [26]

$$\phi = \pi(n_+ - n_-)\frac{l}{\lambda}, \tag{2.1}$$

where l is the length of the medium traversed and λ is the wavelength of light. The difference

between n_+ and n_- is shown in Fig.2.3 . On resonance, the rotation is related to the Zeeman shift in the $M = \pm 1$ sublevels. For light with spectral width of the absorption line much smaller than the transition width, and for zero frequency detuning from the resonance, the optical rotation can be estimated as [26]

$$\phi \approx \frac{(2g\mu B)/\hbar\tau)}{(1 + ((2g\mu B)/(\hbar\tau))^2)} \frac{l}{l_0}, \tag{2.2}$$

where $2g\mu/\hbar$ is correlated to Zeeman splitting, τ is the Doppler width of the absorption line (of order GHz), and l_0 is the absorption length in the medium.

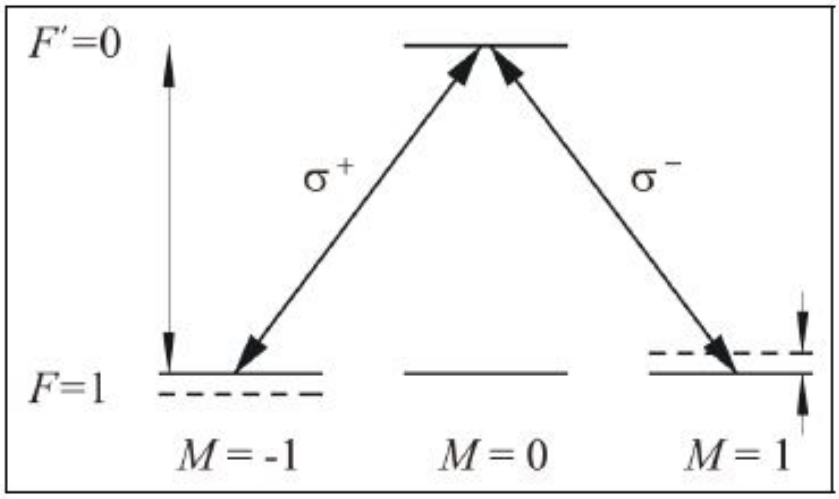

Figure 2.2: Illustrative example of F = 1 to $F' = 0$ atomic transition with Zeeman splitting in the presence of a magnetic field. Image has taken from [27]

.

In NMOR, the optical properties of the medium are modified by the laser light, resulting in nonlinear effects such as hole-burning and the creation of a coherent dark state. Hole burning is the nonlinear effect leading to enhanced Faraday rotation. Spectral holes, or Bennett-structures, are dips in the velocity distribution of a group of atoms produced by pump laser beam. The Faraday rotation produced by atoms with such velocity distribution can be thought of as rotation produced by the Doppler distributed atoms without the hole minus the rotation that would have been produced by the pumped out atoms.

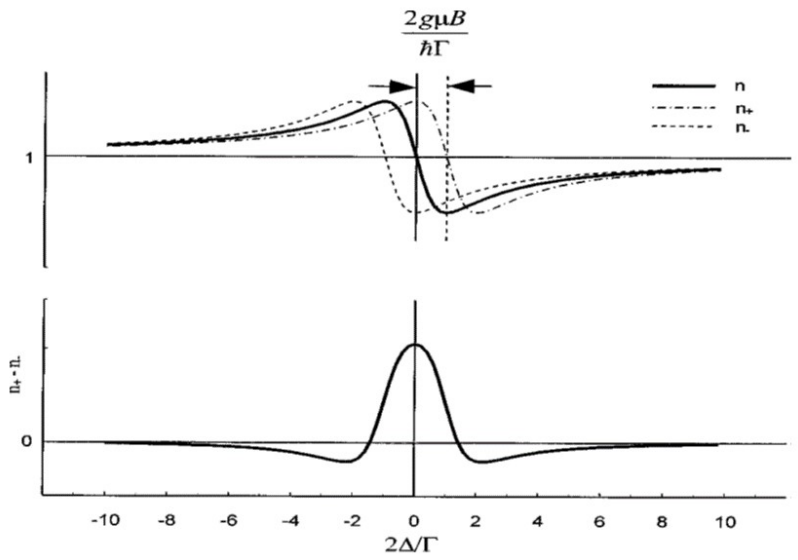

Figure 2.3: The dependence of the refractive index on light frequency detuning D in the absence (n) and in the presence ($n_{\pm}$) of a magnetic field. Shown is the case of $2g\mu B = \hbar\tau$ and a Lorentzian model for line broadening. The lower curve shows the difference in refractive index for the two circular polarization components. This is the characteristic spectral profile of Macaluso Corbino optical rotation. Image taken from [26]

Optical pumping is a process by which light modifies the quantum state of the medium it is transmitting through. Coherent population trapping can be described as the pumping of the atomic system in a particular state, the coherent superposition of the atomic states, which is a nonabsorbing state. The exciting radiation creates an atomic coherence, such that the atom's evolution is prepared exactly out of phase with the incoming radiation and no absorption takes place. In the presence of a magnetic field, the atomic alignment axis created by the coherent population trapping precesses around the direction of the field with the Larmor frequency.

2.3 Magnetometry using NMOR

Nonlinear magneto-optical rotation (NMOR), is a promising technique for a new generation of ultrasensitive atomic magnetometers. NMOR magnetometers have the advantages of operating near room temperature and of being all optical (i.e., they do not require magnetic

field compensation or excitation). Magnetometers based on nonlinear magneto-optical rotation (NMOR) feature parallel pump and probe beams and measure the magnetic field along the direction of beam propagation [27] , and they can achieve sensitivity on the order of 1 fT/$\sqrt{\text{Hz}}$ [28].

Several dispersion-like features in the magnetic field dependence of the nonlinear magneto-optic effect were observed [29] in an experiment performed on rubidium atoms contained in a vapor cell with anti-relaxation coating. The narrowest feature has effective resonance width $\Delta B \sim 280$ nT is the peak-to-peak separation. The observed nontrivial dependence of the magneto-optic effect on transverse magnetic fields is discussed.

Budker et al. [30] demonstrated that the frequency modulated (FM) NMOR technique is useful for increasing the dynamic range of NMOR-based magnetometers. It is possible to achieve the sensitivity of the device in the range of 10^{-15} T/$\sqrt{\text{Hz}}$ [31] (comparable to the most sensitive superconducting quantum interference (SQUID) sensors).

Studies have been reported by Pustelny et al. [32, 33] an all-optical magnetometric technique based on nonlinear magneto-optical rotation with amplitude-modulated (AM) light. To extend the magnetometer sensitivity to magnetic fields where Larmor precession is much faster than the ground state relaxation rate, it is necessary to synchronize the optical pumping rate with Larmor precession which can be achieved by modulating the light. In AM NMOR, the atoms need to be pumped repeatedly. When this modulation frequency is the same as the harmonic frequency of the atoms we observe NMOR signal. Optimization of modulation waveforms is possible in AM NMOR which offer better control of the atomic dynamics and observed signals. The method enables sensitive magnetic-field measurements in a broad dynamic range. The sensitivity of 4.3×10^{-7} μT/$\sqrt{\text{Hz}}$ at 1 μT and the magnetic field tracking in a range of 4 μT has been achieved [32].

Patton et al. [34] showed that an all-optical magnetometer is also capable of measuring the direction of a magnetic field along with field magnitude . This study has been conducted using nonlinear magneto-optical rotation in cesium vapor. Vector capability is added by

effective modulation of the field along orthogonal axes and subsequent demodulation of the magnetic-resonance frequency. The sensor exhibits a demonstrated rms noise floor of 65 fT/$\sqrt{\text{Hz}}$ in measurement of the field magnitude and 0.5 mrad/$\sqrt{\text{Hz}}$ in the field direction. Applications for this all-optical vector magnetometer would include magnetically sensitive fundamental physics experiments, such as the search for a permanent electric dipole moment of the neutron.

NMOR based atomic magnetometers can also be operated in self-oscillation mode [35, 36] originally proposed by Bloom [37]. It is possible to achieve a sensitivity of at least 5 pT/$\sqrt{\text{Hz}}$ by operating NMOR based magnetometer in this mode. Being a quite fast process and having a high bandwidth are the main features of this self-oscillation scan.

Pustelny et al. [38] showed that when the magnetic field is along the light propagation direction, the main resonance occurs at twice the Larmor frequency ($2\Omega_L$). This resonance appear because of the symmetry of the optically pumped state. In this case, the amplitude of resonance signal decreases with increasing tilt angle . However, If we tilt the magnetic field direction towards the light polarization axis a new resonance appears at Ω_L along with the main resonance at $2\Omega_L$ if linearly polarized light is used. The amplitude of the new resonance signal at Ω_L increases as the angle between B and the light propagation direction increases while main resonance amplitude at $2\Omega_L$ decrease with increasing tilt angle. However,when the tilt angle is larger than some certain angle the resonance amplitude measured at Ω_L also start to decrease and reaches zero when the magnetic field is directed along the y axis. It could be possible to evaluate the magnitude of the magnetic field from the ratio of the resonance amplitudes at Ω_L and $2\Omega_L$. The ratio of the resonance amplitudes at Ω_L and $2\Omega_L$ can be used to evaluate the magnitude of the B-field at the measuring point.

Along with FM NMOR and AM NMOR, in order to achieve further sensitivity in magnetic field measurement another way of operating atomic magnetometer has been studied by M. Sturm [21]. In his study an all optical magnetometer has been operated in Free Induction Decay (FID) mode where the Cs atoms have to be excited once and afterwards the decaying

processes (damped oscillation) of the coherence state is observed (similar to NMR). The sensitivity depends on the T_2 time, which is the decay time of the macroscopic polarization moment.

2.4 Rb magnetometry based on NMOR

A scalar magnetometer requires coherent precession of the spin ensemble, so a resonant excitation must be applied in order to force some large fraction of the atoms to precess together with a common phase. Otherwise the phase of individual atoms is random, and the total transverse spin of the ensemble averages to zero [25] . The sensitivity of an NMOR based atomic magnetometer depends on the lifetime of the polarization state. So in this case, it is important to use ground-state polarization since it has a longer lifetime than the excited states.

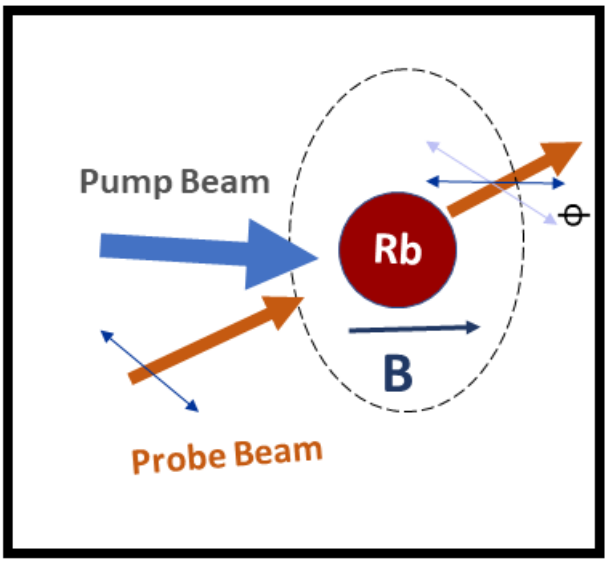

Figure 2.4: The schematic diagram of the optical magnetometry technique. A linearly polarized pump beam is sent through the vapor cell containing natural Rubidium placed in a homogeneous magnetic field B. The polarization rotation of a linearly polarized probe beam is used to measure the magnetic field.

The working principle of a Rb magnetometer can be described as three step process

- Resonant light polarizes Rb atoms via optical pumping. Magnetic moments of the atoms are oriented with respect to the axis of alignment.

- Aligned magnetic dipole moments experience a torque and precess around the axis of the field at the Larmor frequency and the medium becomes birefringent.

- A linearly polarized probe beam propagating parallel to the pump beam is passed through the alkali vapor, the plane of polarization of the probe beam rotates by an angle proportional to the spin component along that direction, and we detect this rotation in order to observe the spin behavior. Optical polarization rotation of a probe beam is used to measure magnetic field.

In the next chapter we will discuss each component and its use for our Rb NMOR magnetometry setup.

Chapter 3

Overview of Rb magnetometer and apparatus

The purpose of this Chapter is to describe the experimental apparatus used at UW. The system is composed of three main parts:

- A tunable laser system, operating near the Rb D1 line. Pump, probe, and laser characterization beams all come from this light source. The beams are analyzed using various sensitive photodiode sensors.
- A paraffin-coated natural Rb cell. The cell provides a vapour pressure of Rb atoms whose spin state can remain coherent after many wall bounces. The long coherence time is important for the best magnetometer sensitivity.
- A magnetic shielding and field generation system. The magnetometer is being operated in magnetic fields that are considerably smaller than Earth's field. An aspect of the research also is to use the magnetometer to learn about magnetic field stability.

In this Chapter, I start with a more detailed overview of the overall experiment. I then discuss each of the major components of the apparatus in more detail.

In Chapter 4, I will cover the initial characterization of a few different modes of operation

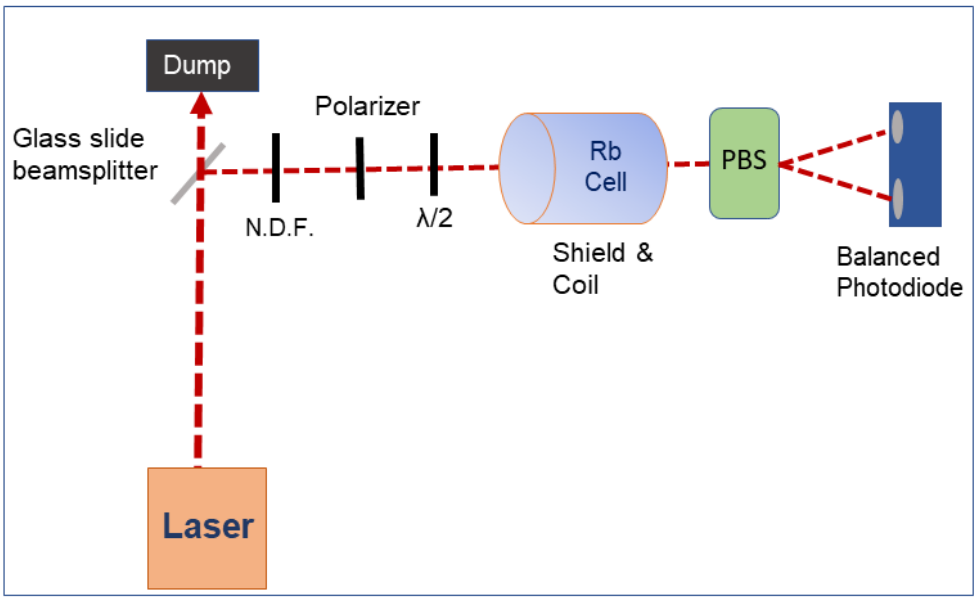

Figure 3.1: Schematic diagram of experimental setup for zero field NMOR measurements (discussed in the text). $\lambda/2$ - half wave plate, N.D.F - neutral density filter, PBS - polarizing beam splitter.

of the magnetometer. (As discussed in Chapter 2, there are several different ways in which the magnetometer can be operated dependent with different advantages and disadvantages to each.)

In Chapter 5, I discuss the advances made in the understanding of the magnetometer performance, mostly in relation to the development of the Free-Induction-Decay mode of operation.

3.1 Overview

Fig. 3.1 schematically depicts a top view of the Rb magnetometer, as it may be used for measurements of the magnetic field within a few hundred pT of zero. The field is averaged over the vapour cell volume. This mode was used, for example, in Ref. [39] to measure the axial magnetic shielding factor of the passive magnetic shielding system. The effect of transverse fields and gradients on this kind of measurement were studied in Ref. [29]. In this thesis, this operation mode was not normally used because we desired to develop the system

for larger magnetic fields. But it is nonetheless instructive to demonstrate the starting point of my thesis research. We also used this mode to study our process of degaussing of the magnetic shields, which was also being developed.

An external cavity diode laser produces light near the Rb D1 transition. The laser is tuned near the ^{85}Rb $F_g = 3$ to $F' = 2, 3$ Doppler-broadened absorption minima. A microscope slide is used as a beamsplitter in order to divert a reduced power into the experiment. The power is further reduced using neutral density filters (indicated by N.D.F. in Fig. 3.1). A linear polarizing sheet is oriented at a 45° angle relative to the vertical direction. Since the laser beam is polarized, this further reduces the power by a factor of two. The laser power after this point is normally in the range of 2-20 μW. A $\lambda/2$ plate is used to adjust the incident plane of polarization.

The beam then passes through a paraffin-coated cell containing Rb vapour. The cell is within a magnetic shielding and field generation system that produces a uniform field along the beam axis. The plane of polarization of the laser light will rotate slightly as it passes through the cell because of non-linear magneto-optical effects. A balanced polarimeter is used to analyze the optical rotation of the laser light resulting from the interaction of the laser light with the atoms in the cell. The polarimeter consists of a polarizing beam splitter (a Wollaston prism) which splits the beam into its vertical and horizontal polarization components. Each component is sensed by a Newport 2307 balanced photo-receiver which outputs the difference in light intensities. If the polarizer is set at a 45° angle and aligned with the axis of the $\lambda/2$-plate, and in the absence of any optical rotation, the balanced photodiode would output zero volts. If the plane of polarization is rotated by passage through the cell, it will be sensed by the differential photodiode signal. This is discussed further in Section 3.9.

Results of the operation of the zero-field magnetometer are discussed further in Sections 4.1 and 3.7.2. In order to measure fields farther from zero, a pump-probe technique is used, where the amplitude of the pump beam is modulated.

Fig. 3.2 shows the schematic layout of the apparatus used for studying the non-linear

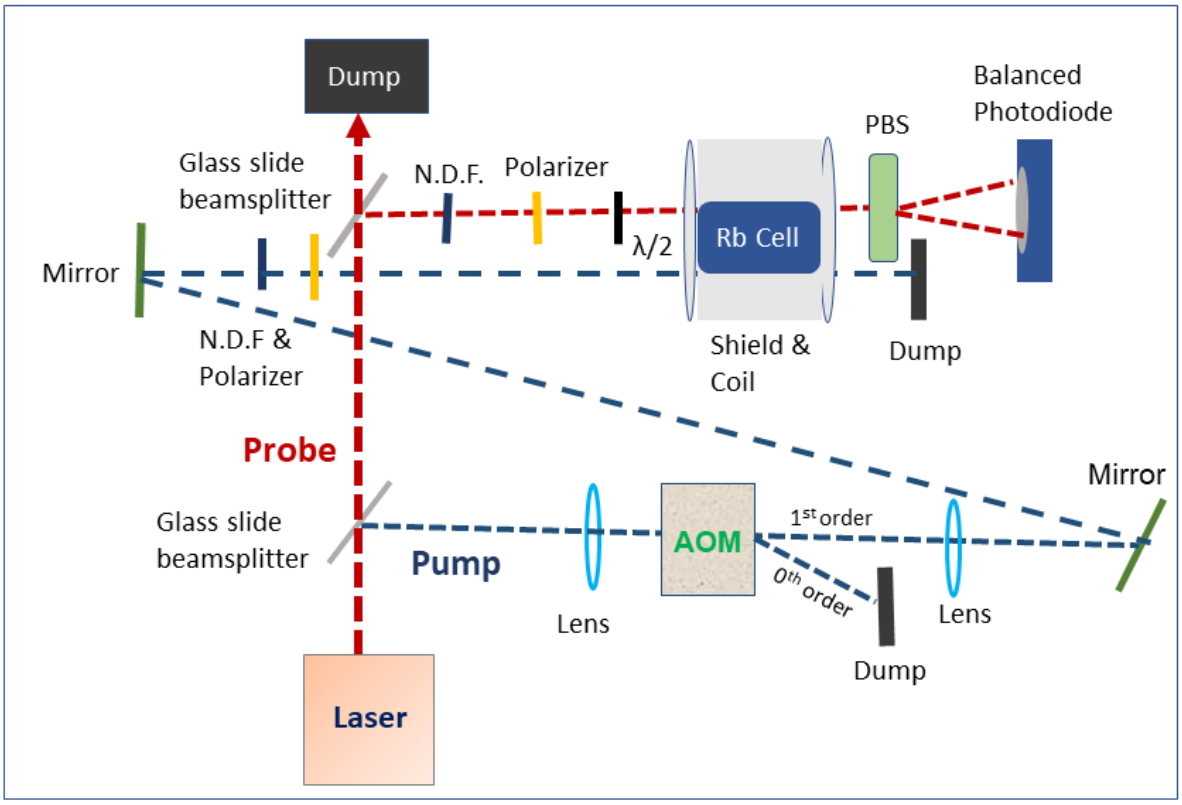

Figure 3.2: Schematic diagram of the experimental setup for measuring the rotation of the polarization plane with amplitude modulated (AM) light. AOM stands for acousto optic modulator, $\lambda/2$ - half wave plate, N.D.F - neutral density filter, PBS - polarizing beam splitter.

Position	Laser Power(μW)
AOM	4000
Pump beam (time averaged)	60
Probe beam	22
After Cell	18

Table 3.1: Adjusted laser power at several positions in the experiment.

magneto-optical effects with the amplitude modulated light. This experimental setup is used in forced oscillation scan and FID NMOR discussed in Section 4.2 and 4.3.

Pump and probe beams are created from the main beam using microscope slides as beam splitters. The typical light power of the pump beam is 40 μW (time-averaged) and the typical light power of the probe beam is 20 μW. An acousto-optic modulator (AOM) is used to modulate the amplitude of the pump beam, normally as a square wave with low duty cycle. The details of the working principle of AOM is discussed in Section 3.5. The pump beam is focused into the AOM and re-parallelized afterward using two lenses of the same focal length. Before interacting in the Rb cell, the pump beam then passes through an N.D.F to adjust the beam power, and then a linear polarizer. After that the linearly polarized light beam interacts with Rb atoms. Since the coherence of the atoms is preserved for long periods of time ($\sim$ s) by the paraffin coating, the pump and probe beams need to overlap in the cell.

The probe beam follows essentially the same path as for the zero-field magnetometer. The nonlinear Faraday rotation signals are analyzed by a balanced polarimeter. A Wollaston prism (labelled as PBS in Fig. 3.2) is used to split the beam into its perpendicular polarization axes which are then analyzed individually by a differential photodiode.

In this case, the optical rotation is also modulated near the pump modulation frequency. A lock-in amplifier is used to demodulate the signal. Table 3.1 shows the typical beam power at several positions in the experimental setup.

3.2 External Cavity Diode Laser

In our NMOR based optical magnetometry setup, laser light is provided by an external cavity diode laser (ECDL). ECDLs emit a single mode laser light with a very narrow linewidth ($\sim$ 100 kHz). Semiconductor laser diodes normally contain a high reflectivity rear facet and a front facet with reflectivity of only a few percent. The diode cavity is known as the intrinsic or internal cavity. The external cavity is formed by the diffraction grating and the diode rear facet. Since the feedback from the grating is generally greater than that of the front facet, the external cavity determines the lasing wavelength. As the wavelength is varied, competition between the frequency determined by the internal and external cavities, and the dispersion of the grating diffraction, leads to mode hops. The laser frequency depends on the cavity length and hence on the thermal expansion coefficient of the cavity material. Micrometer screws enable manual coarse tuning, while precise scans without mode hops are performed by a piezo actuator. The length of the external resonator and the grating profile can be changed by scanning the piezo actuator. The internal resonator should also need to scan to suppress mode-hops and for the improvement of the mode-hop-free tuning range. This can be done by applying a ramp proportional to the scan control output ramp to the laser diode current. This leads to a change of the refractive index n of the semiconductor material and thus to a change of the length of the internal resonator. This feature is known as feed forward [40]. Our Toptica DL-100 outputs tunable wavelength near 795 nm with an output power $<$ 100 mW. The laser spot size is elliptical, and approximately 3 mm x 5 mm = 15mm^2. The laser was typically tuned to the D1 ($F_g = 3$ to $F' = 2, 3$) Doppler-broadened absorption minima. This was done using the feed-forward function of the ECDL, where the laser current and external cavity length are swept simultaneously to prevent mode hopping. The final tuning was then adjusted to maximize the optical rotation signal.

3.3 Dichroic Atomic Vapor Laser Lock (DAVLL)

The dichroic atomic-vapor laser lock (DAVLL) system , operates in Doppler broadened mode, employing magnetic field induced circular dichroism and birefringence of the atomic vapor. The basic idea of the technique is that for an isolated atomic line, linear-optical circular dichroism induced by a longitudinal magnetic field has dispersive frequency dependence. The corresponding ellipticity induced in the transmitted light beam propagating along with the magnetic field turns to zero when the light is resonant with the atomic transition. A variant of the technique used to lock the frequency on the wings of an optical line uses linear-optical circular birefringence and the detection of optical rotation rather than induced ellipticity. For our setup, in order to control the laser frequency to a fraction of the Doppler-broadened linewidth of the relevant hyperfine atomic transition of the Rb D1-line, a frequency error signal is generated by taking usage of the Zeeman effect combined with circular dichroism of an atomic vapor which is exposed to a magnetic field [41]. The generated error signal passes through zero crossings as the laser frequency is coincide with the lock frequency. A feature of the optics setup of Ref. [41] is that the lock point can be adjusted by physically rotating optical elements to achieve the desired zero-crossing. The schematic diagram of the apparatus used in the DAVLL system is shown in Fig 3.3. Linearly polarized laser light is incident on a glass cell filled with Rb vapor surrounded by a set of permanent magnets . In this magnet arrangement a layer of ceramic magnets and a layer of flexible magnetic strips/sheets are placed one after another and a customized holder is used to hold the pieces together. A picture of the magnets and cell is shown in Fig. 3.4. The wave vector of the light is parallel to the axis of the magnetic field generated by the permanent magnets. After the interaction of the laser beam with the Rb cell, the beam passes through a quarter-wave plate before impinging on a polarizing beam splitter (PBS). In our experiments we used a polarizing cube beamsplitter. The linearly polarized beam incident can be split into two orthogonal circularly polarized beams by this arrangement. A set of photodiodes is used to

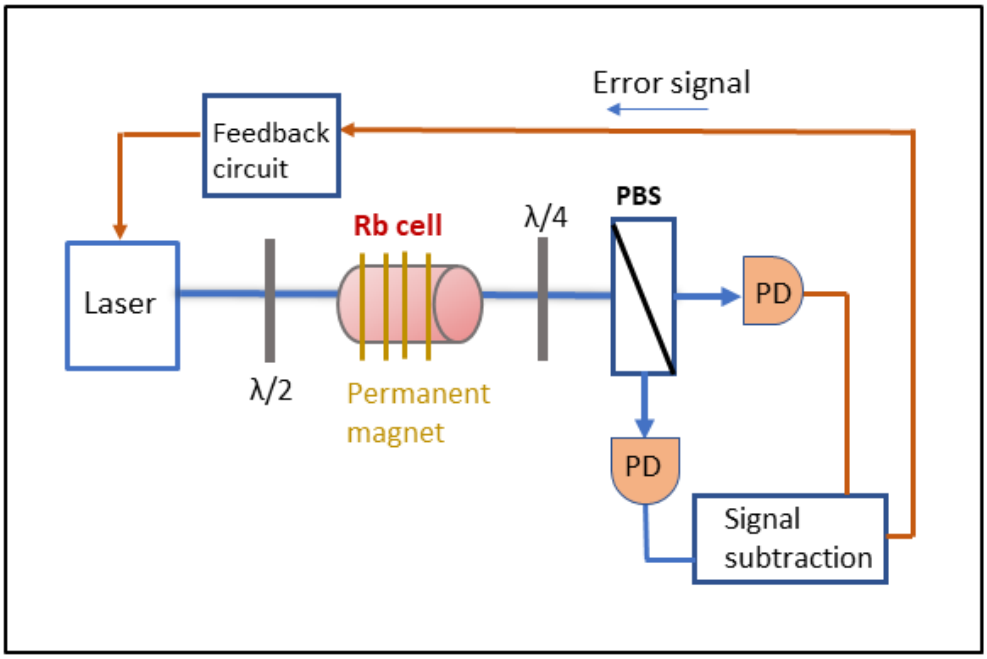

Figure 3.3: Schematic diagram of experimental setup for characterizing the DAVLL. PBS- polarizing beam splitter, PD- photodiode.

detect the intensity of the right and left circularly polarized beams. Both of the photodiodes are attached to a polarimeter board which is used to measure the difference in signals and amplifies it. A Tektronix TDS2024 oscilloscope is used for monitoring each photodiode signal as well as the difference output. The signal is then fed into a grating piezo which finally controls the laser diode current corresponding to a certain laser frequency.

3.4 Laser tuning and locking

In order to polarize atoms by optical pumping, it's important to tune the laser properly to the expected transition line. A photograph of the laser power supply and control system is shown in Fig. 3.5. The diode temperature and power both need to be adjusted to get the wavelength of interest. For our setup, the diode temperature was typically set to 20.1°C. The laser current is then adjusted to select the mode of the diode near the Rb D1 line. By adjusting the laser current and piezo-electric cavity length control, a mode-hop free

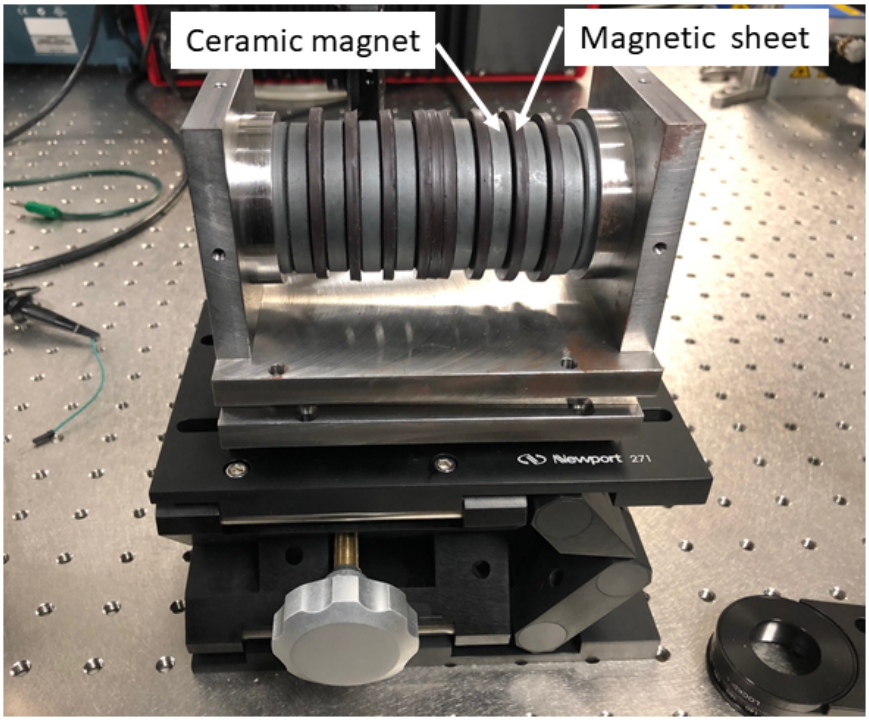

Figure 3.4: Picture of cell-magnet arrangement in the DAVLL system.

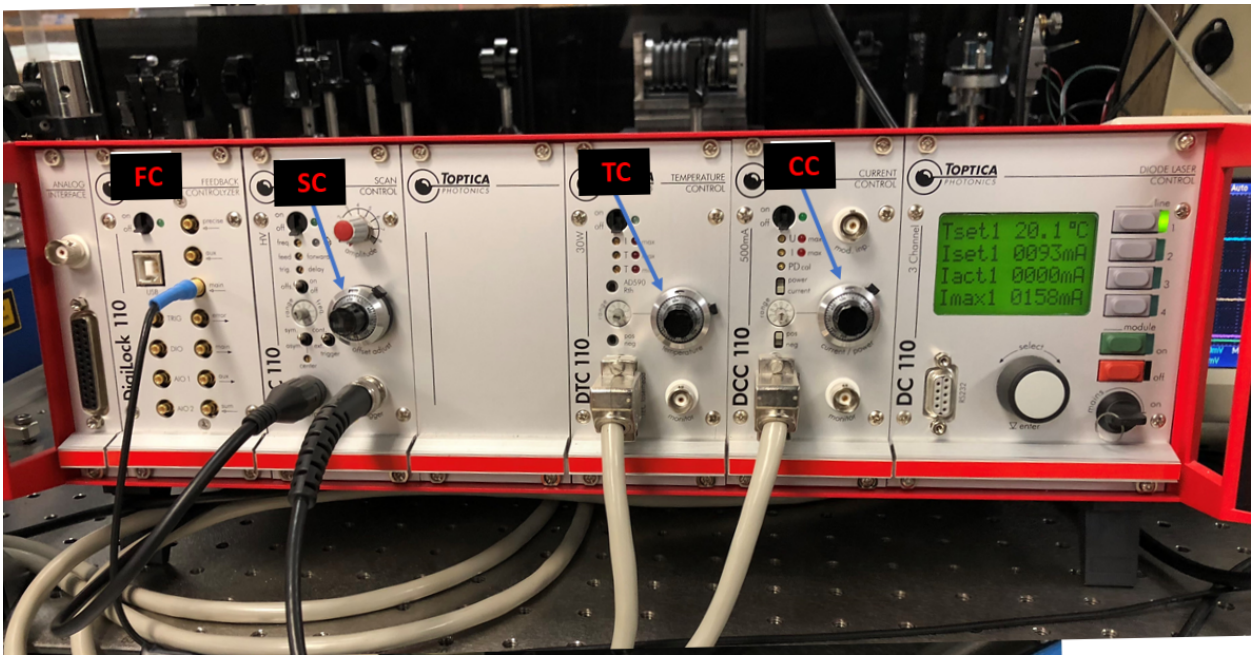

Figure 3.5: Diode laser controller unit consist of analog current control module (CC), scan control module (SC), temperature control module (TC), feedback controlyzer (FC) and Diode Laser Controller display.

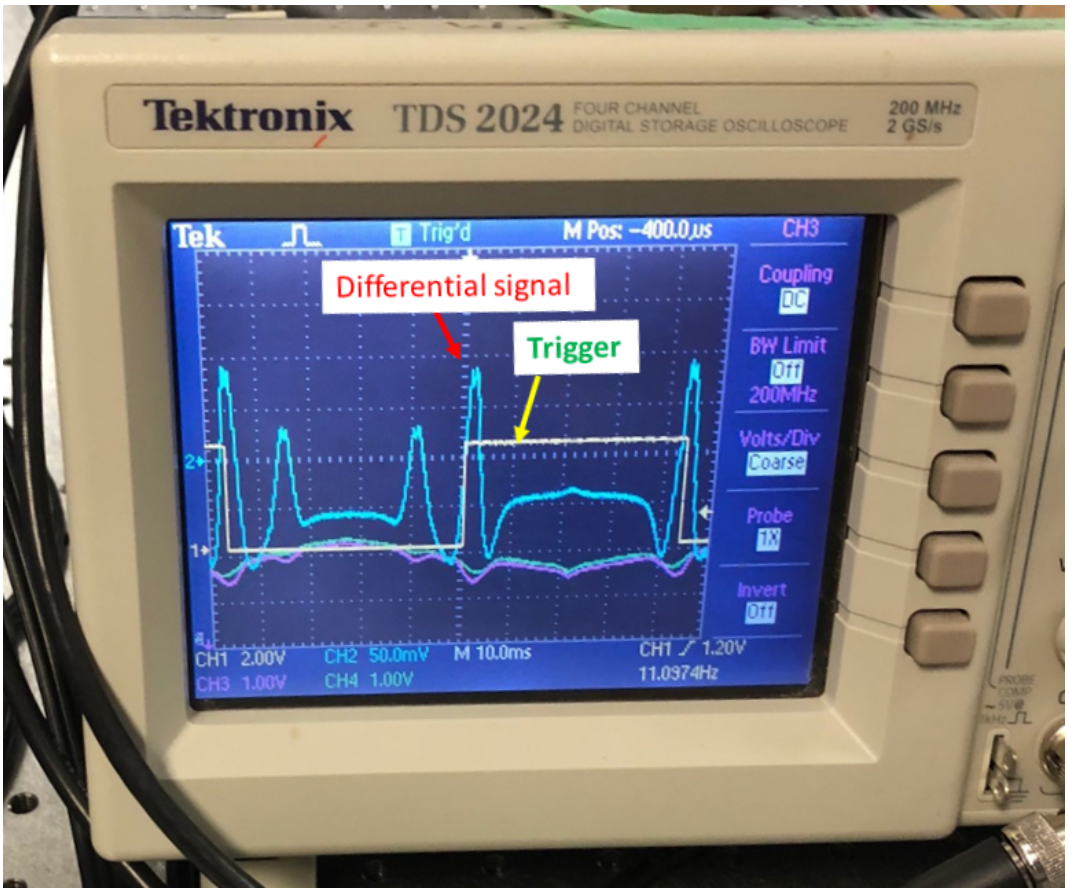

Figure 3.6: Oscilloscope trace of DAVLL signals during laser tuning.

region was selected for tuning. Tuning to the transition of interest was then done using "offset adjust" knob of the scan control system, which controls the feed-forward system described earlier, adjusting both the laser piezo voltage and current simultaneously with a fixed constant of proportionality between them.

Tuning is usually done while the piezo is scanning, by adjusting the offset while looking at the signals in the DAVLL system. An oscilloscope is used to observe the output of each PD and the differential amplifier of the DAVLL system. The scope is triggered by the trigger output on the scan control (SC) panel. The Laser current can be controlled by adjusting the current control knob until the spectral structure of ^{85}Rb appears (see Fig. 3.6). we need to keep adjusting the current control knob until a maximum symmetry between the upsweep and downsweep portions is achieved. After that, by adjusting the "amplitude" knob of the

Figure 3.7: Digilock graphical user interface.

SC panel, we can zoom into the structure and tune the central frequency of the scan to the absorption minima.

The Digilock 110 feedback controlyzer (FC) is used for laser locking, using a PID system. It offers graphical user interface shown in Fig. 3.7. The FC is connected by USB to a computer where Digilock software is installed. The output signal of the differential photodiode is fed into the FC main input. After connecting the DigiLock 110 I turn on its scan function and navigate to the autolock screen at the bottom [42, 43]. Then the the portion of the spectrum that I tuned earlier will appear (see Fig. 3.7). Then I select the crosshairs tool which allow us to drag the crosshairs on the part of the spectrum that we want to tune to. Finally for successful laser locking we need to click and select "PID lock to slope", selecting the

exact lock point on the computer screen. PID parameters were adjusted to give a relatively low-bandwidth lock. For most of the studies reported in this thesis we use the auto locking features of the DigiLock software.

3.5 Acousto-optic Modulator (AOM)

The acousto-optic modulator (AOM) offers a method of modulating the amplitude of the laser light. The AOM is used to modulate the amplitude of the pump beam. The pump beam is linearly polarized light, and so the amplitude is modulated at $2\omega_L$. For 1 μT field the AOM operation frequency is 9335 Hz and the AOM driving frequency is 2034 Hz when the magnetometer operate at 0.2 μT. The AOM itself operates at 80 MHz RF frequency. The "operation frequency" refers to the modulation frequency of the RF power. This form of pumping generates a coherent precession of an axis of alignment in the atoms in the Rb cell. In FID mode, once the coherence has been sufficiently established, the AOM may be switched off in order to measure the precession frequency of the state using the probe beam.

The principle of operation of an AOM is shown in Fig. 3.8. The AOM contains a crystal which has a piezoelectric transducer attached at the end that propagates acoustic waves within the medium. An RF signal in the MHz range is applied to the transducer to generate the acoustic wave. The compression and refraction of the sound waves result in periodic variations of the refractive index of the medium which form a diffraction grating. Incident laser light will be diffracted by the grating, generally providing a number of diffracted beams. The strength of the sound wave is directly related to the intensity of the defracted light. Depending on the interaction length L, laser wavelength λ in the medium and the sound wavelength Λ it is possible to operate AOM in two different modes, the Raman-Nath regime and the Bragg regime. For our experiment we operated in the Bragg regime.

In the Bragg regime ($L > \Lambda^2/\lambda$) the light beam enters the medium at one particular

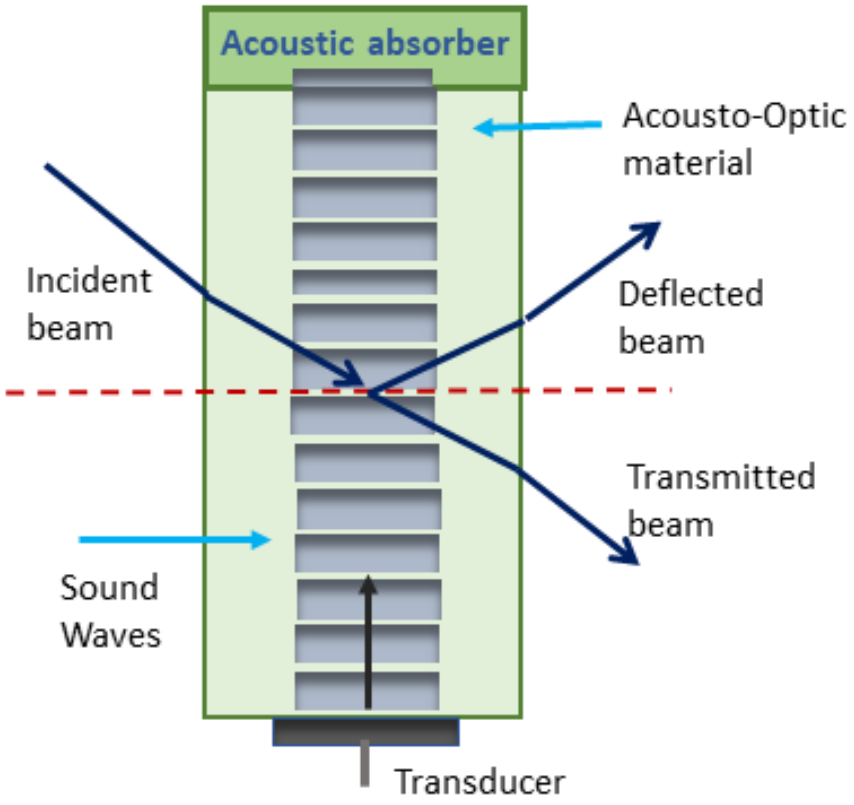

Figure 3.8: Principle of an acousto-optic modulator.

Bragg angle

$$\theta_B = \frac{\lambda}{2\Lambda}. \tag{3.1}$$

The observed diffraction pattern generally consists of two diffraction maxima; these are the zeroth and the first orders. In this case the possible maximum intensity of the first order diffracted light can be near 100%. Generally in our setup we generally achieve $\sim 10\%$. For FID measurement, the pump beam need to be completely off during probe time in order to avoid any disturbance in atoms quantum state due to the pump beam. Since no light remains in the first order diffraction when the power of the sound source vanishes, this first order can be used for amplitude modulation.

For this experimental setup, an Isomet 1205C-1 AOM is used with an RF center frequency of 80 MHz. The AOM uses a crystal of lead molybdate ($PbMoO_4$) for the optical interaction medium and lithium niobate as the piezoelectric transducer. The amplitude modulating pulses are driven with an Isomet 532C-2 AO driver. An Agilent 33522A function generator is used to control the AOM driver.

This amplitude modulation in our experiments was generally done by a square wave modulation with a duty cycle of 1-10%. For this specific model of AOM driver the RF rise/fall time is smaller than 6 nsec. The active aperture of the modulator is tiny (1 mm) and light is focused into the AOM and recollimated afterward. In order to reach maximum deflected light intensity small adjustments are made near the Bragg angle.

3.6 Rb Cell

When glass cell is used to store alkali atoms, the atomic mean free paths increase and alkali spins depolarize immediately after making non-elastic collision with the glass walls. Prolonging the atomic alignment is crucial to achieving ultra-narrow NMOR resonance widths. So it is necessary to prevent depolarizing collisions to achieve the longer lifetimes of atomic ground state coherences [44, 45]. This can be achieved by coating the inner walls of the cell

Figure 3.9: Paraffin coated Rb cell. The cell contains natural rubidium with stable isotopes ^{85}Rb and ^{87}Rb. The cell is cylindrical, 5 cm long and 5 cm in diameter with optical flats on the ends.

with anti-relaxation materials, in our case paraffin. Paraffin can preserve the polarization of the atoms after ~ 1000 wall bounces before depolarizing [44, 46].

A photograph of the paraffin-coated vapour cell used in this work is shown in Fig. 3.9. The cell contains natural rubidium with stable isotopes ^{85}Rb and ^{87}Rb. The cell is cylindrical, 5 cm long and 5 cm in diameter with optical flats on the ends. The cell was provided by D. Budker, having been prepared in a fashion similar to the cells described in Ref. [44]. For Ref. [39], our group characterized the cell using a method similar to Ref. [44], by measuring the relaxation of longitudinal polarization using optical rotation as a probe. The long time component of the relaxation was thereby found to decay with a time scale of 400 ms. Longer relaxation time indicates good quality of cell. It was also characterized magnetometrically using the zero-field mode of operation and found to have a width near zero field competitive with the typical 2 μG widths achieved by Budker [29]. The temperature of the vapour cell was determined by the ambient temperature of the surrounding room ($\sim 21^{\circ}$). At this temperature the vapour pressure is 1.83×10^{-7}. Rb vapor cell have lower vapor pressure than

cesium (Cs), causing them to be less sensitive at room temperature than Cs magnetometers [21] [47]. Since Cs naturally has a higher vapour pressure for future work we are planing to use Cs vapour cells. Heating the cell may cause the paraffin to melt if not controlled carefully. Heating also could require electrical currents that might generate magnetic backgrounds.

3.7 Magnetic field system

The magnetic field system consists of a four-layer μ-metal magnetic shielding, degaussing system and internal coils.

3.7.1 Magnetic Shielding

In precision magnetometry, magnetic shielding is required to achieve well characterized, stable magnetic field conditions independent of the EarthâĂŹs magnetic fields and environmental perturbations. A picture of the magnetic shield and internal coil system is shown in Fig. 3.10. Then endcaps of the shield have been removed for clarity. The white cylinder within the shield is where the internal coil has been wound. The photograph shows a different (lower quality) paraffin-coated cell than used in this work.

Fig. 3.11 shows a schematic diagram indicating the measurements of the magnetic shield system. The design process for the shield is discussed in Ref. [39]. The axial magnetic shielding factor was measured using the zero-field magnetometer in Ref. [39] and found to be 10^7, which is consistent with a relative magnetic permeability of $\mu_r = 20,000$ for the material used in the shielding layers. All access (for laser light and wires for coils) is made through holes in the endcaps. The innermost magnetic shielding layer is 4" in diameter and 8" long, limiting the space available for experimental equipment.

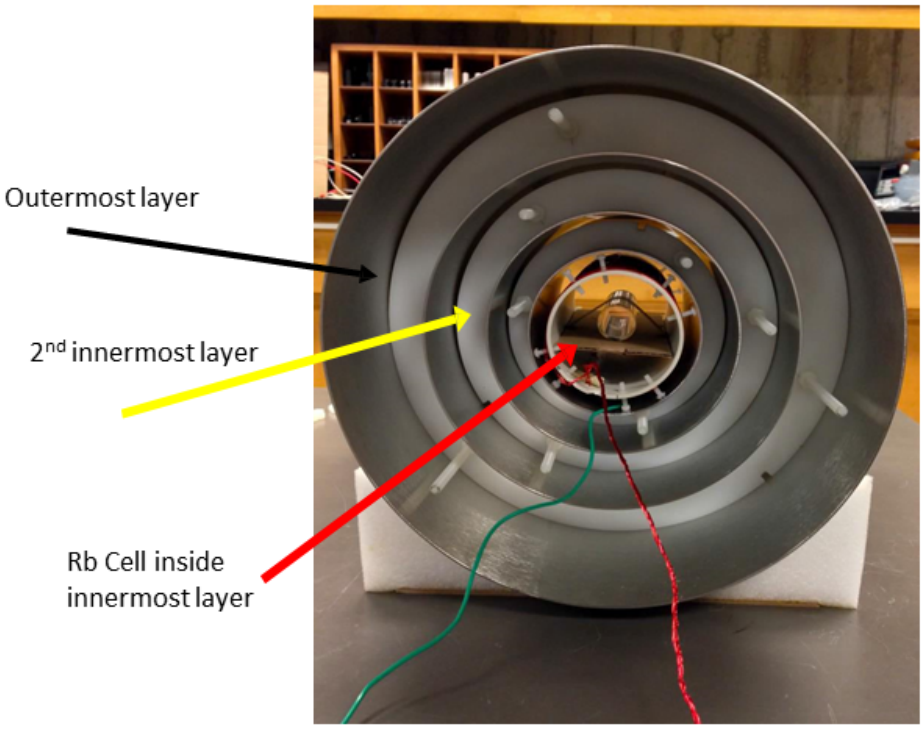

Figure 3.10: Four layer μ-metal magnetic shielding. The diameter of each endcap is larger by 0.1 cm to fit over its corresponding cylinder. The hole diameter and stovepipe length for each endcap are the same. High density polyethylene spacers and nylon thread rods/nuts are used to hold the shields and endcaps together.

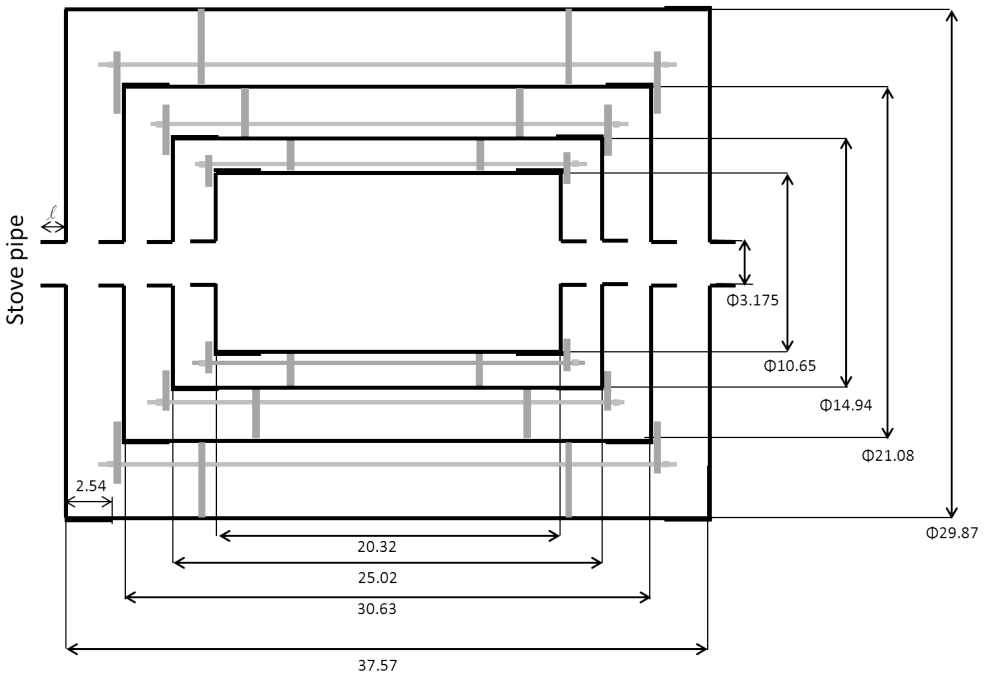

Figure 3.11: Schematic diagram of the 4-layer magnetic shield (dimensions in cm).

3.7.2 Degaussing system

Our four layer μ metal magnetic shield is designed to minimize the magnetic field at the cell, but magnetic hysteresis limits the ability to do so. A degaussing process is used to reset the magnetic properties of the material. Ideally the degaussing process reduces the remanent magnetic field in the volume surrounded by the innermost shielding layer.

Part of the work presented in this thesis relates to studies of the effectiveness and reproducibility of the degaussing system. The new system was developed subsequent to the results presented in Ref. [39].

The degaussing system consists of two coils. The most important of these is a 16-turn toroidal winding on the innermost magnetic shielding layer. The coil used in our experiments is similar to the white wire shown in Fig. 3.12. The windings conflict with the endcaps of the innermost shield, and so these were removed for most experiments reported in this thesis.

Since the endcaps of innermost shield are removed, magnetic coupling between the innermost volume and the second-to-innermost magnetic shielding layer is increased substantially.

Figure 3.12: Photograph of degaussing coil.

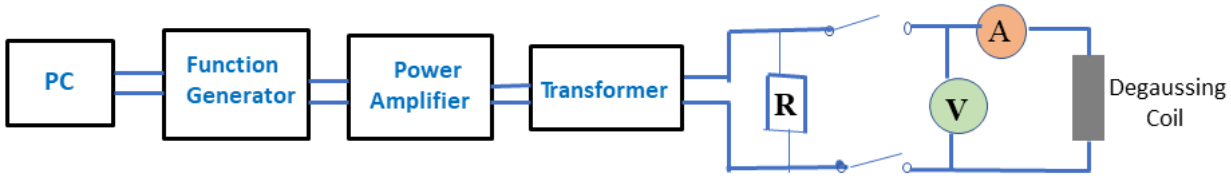

Figure 3.13: Schematic diagram of degaussing system consist of function generator, power amplifier, transformer, variable resistor (R), 1 Ω sense resistor (A), oscilloscope (V) and degaussing coil.

To potentially be able to degauss this and the other shield layers, a wire was wound in a single loop through the outer 3 layers of shielding.

Degaussing is achieved by supplying the coil with an oscillating current with a decreasing envelope over time. The current amplitude starts from a current that yields magnetic saturation inside the ferromagnetic material, and generally we used a linear envelope to decrease the amplitude to zero. Various parameters of the degaussing sequence were studied.

A schematic diagram of the degaussing system is presented in Fig. 3.13. An Agilent 33522A function generator provides a sinusoidal voltage output with a linearly decreasing envelope from 10 V amplitude to zero. The function generator controls a transimpedance power amplifier driving the degaussing coil. A DCP 260 Servowatt amplifier is used in

transimpedance (voltage to current) mode to output a current maximally ±5 A. The transimpedance gain is 0.5 A/V; *i.e.* for 10 V input, the current output is 5 A.

The transformer is a HS1B250 Hevi-Duty transformer which provides near-unity gain. This transformer is used to remove any possible dc offset of the power amplifier [48]. A double-pole, double-throw (DPDT) switch is used to electrically connect and disconnect the degaussing coil from the circuit. A rheostat of resistance 44 Ω was typically used to ramp the resistance of the system connected to the degaussing coil slowly to zero before opening the switch. This is believed to reduce transients injected into the degaussing coil which could be induced by opening the switch, although in our trials it seemed to have little effect and so it was not always used; part of the reason for this could be because the transformer itself has a resistance of only 5 Ω.

An oscilloscope measuring across the degaussing coil could be use to monitor the degaussing, or measuring across a 1 Ω resistor in series with the degaussing coil in order to measure current. The wires going to the degaussing coil are twisted together to avoid picking up noise.

Degaussing was normally conducted at 10 Hz. For a sinusoidal input of amplitude 10 V at 10 Hz, the measured current was observed to vary sinusoidally with amplitude 4.2 A. The discrepancy with the transimpedance gain mentioned above is believed to be dominated by losses in the transformer.

At 10 Hz, the coercivity is $H_c = 25 - 30$ A/m. This was measured by using a primary/secondary winding system similar to that shown in Fig. 3.12 in order to map out the full $B - H$ curve [49]. To degauss properly, it is important to drive the shield well into saturation, normally at 10 times the coercivity or larger. For a winding of N turns on a thin toroidal material of radius R, the H-field in the material is [50]

$$H(t) = \frac{NI(t)}{2\pi R}. \tag{3.2}$$

Setting	Value
Function generator	
Frequency	10 Hz
Sample rate	10000 samples/s
Initial amplitude	10 V

Table 3.2: Typical settings for the degaussing system. The envelope function was programmed into the function generator amplitude modulation system, which uses 10^6 individual points to define the envelope.

For our current of 4.2 A, and a 16-turn degaussing coil, wound on our innermost shield of radius 2", the H-field reaches a maximum of 210 A/m which is more than required. This was how the number of turns was selected to be 16, based on the capabilities of the current amplifier, and the coercivity of the material.

Example function generator settings are shown in Table 3.2. In the function generator we use an envelope function which has 1×10^6 points. The degaussing linear ramp sequence uses the initial 5×10^5 points, and the envelope is set to zero for the other 5×10^5 points in order to give the user sufficient time to decrease the rheostat resistance and open the manual DPDT switch. It was found that if the function generator output was turned off, this would give a clearly observable spike if the switch had not been opened by that time.

The "sample rate" setting affects how quickly we move through this waveform. For example, if the sample rate is set to 10000 samples/s, it will take 50 s to complete the degaussing ramp sequence. If the frequency of the carrier wave is set to 10 Hz then it means 500 cycles were completed. A typical recommended number of cycles for good degaussing is 500-1000 cycles [48]. In studies where we vary the sample rate, it is essentially the number of cycles which we are varying.

3.7.3 Internal coil

For the Rb atomic magnetometer an internal coil referred to as z-coil is used to provide the magnetic field along the axis of light propagation direction (z-direction). This coil was designed to produce a uniform field in the central region of the Rb cell. The z-coil was wound

on a 7.62 cm diameter, 20.32 cm long ABS plastic pipe. Seven turns of 26 AWG magnet wire were wound at 2.54 cm spacing, with 1.27 cm spacing from the magnetic faces of the endcaps of the innermost magnetic shield. The spacings were chosen so that, in the infinite permeability limit, and in the limit where the axial aperture holes in the endcaps are small, the boundary conditions would produce image currents forming an infinitely long solenoid. This was the configuration used in Ref. [39]. For those measurements, homogeneity of the residual field and magnetic field generated by the coil system was measured by scanning a fluxgate magnetometer along the axis of the system with and without the coil energized. At a field of 1 μT, the axial field generated by the coil was uniform to the 1% level.

Unfortunately this is not true for the data presented in this thesis, because the endcaps are removed. The homogeneity is expected to be $\lesssim 5\%$ which is adequate for our experiments. As implied earlier, the main problem found in removing the endcaps has to do with degaussing the second-to-innermost shield which is magnetically coupled to the z-coil when the endcaps are removed.

Two saddle coils were wound on the same cylindrical ABS pipe in order to control transverse fields (along the x- and y-directions) internally; these were normally disconnected during precision measurements. They were used also for the tilted field measurements.

The internal coil system was calibrated using a three-axis fluxgate magnetometer at fields of 100 nT. The calibration constant for the z-coil is 48 nT/mA and the calibration constant for x- and y-coil is 25 nT/mA. The calibration of the z-coil was verified using our magnetometer the known gyromagnetic ratio of ^{85}Rb.

3.8 Lock-in Amplifier

For the 0.2 μT magnetic field and higher measurements, we used a SR830 DSP lock-in amplifier to demodulate the signals. The lock-in amplifier is able to suppress noise contributions which differ from the reference frequency. A reference signal is applied to the lock-in

amplifier which may be done by an internal or external oscillator. In this magnetometry setup, the sync output of the function generator is used as external reference signal for forced-oscillation scans. The external reference signal is monitored by a phase-locked loop (PLL) which provides the internal reference of the lock-in. The lock-in amplifier has two phase sensitive detectors providing two output signals (X and Y). To generate the X signal the internal reference signal is multiplied with the input signal and then the signal pass a low-pass filter where the AC contributions to the signal are being removed. To generate the Y signal, the same process is done for a reference signal phase shifted by 90°. The X signal is often called the "in-phase" and the Y signal the "out-of-phase" or "quadrature" signal.

3.9 Optical Rotation and Balanced Polarimeter

Sensitive magnetometry based on optical rotation requires the accurate detection of small optical rotation angles. We use a balanced polarimeter technique. Transmitted light was analyzed for optical rotation by a balanced polarimeter system containing a Wollaston prism and a Newport model 2307 balanced photo-receiver. The Wollaston prism separates incident light into its horizontal (X) and vertical (Y) polarization components, and the difference of these signals is reported by the balanced photo-receiver. If incident light is linearly polarized with an angle $\pi/4$ between the plane of polarization and axis of the prism, the X and Y intensities will be equal and the differential photodiode will report zero output. If the plane of polarization is then rotated by a small angle α relative to the initial $\pi/4$ angle (a total angle $\theta = \alpha + \pi/4$ from the X axis), the X and Y intensities selected by the prism are

$$I_X = I_0 \sin^2(\alpha - \frac{\pi}{4}) \tag{3.3}$$

and

$$I_Y = I_0 \cos^2(\alpha - \frac{\pi}{4}) \tag{3.4}$$

where $I_0 = I_X + I_Y$ is the intensity of the incident light. The intensities I_X and I_Y would be detected by respective photodiode channels. For small rotations $\alpha \ll 1$ we can write

$$\alpha \approx -\frac{I_X - I_Y}{2(I_X + I_Y)}. \tag{3.5}$$

In general, we measured the balanced photoreceiver output, which is proportional to $I_X - I_Y$. Hence most "optical rotations" are measured in Volts in this thesis. In cases where the lock-in amplifier is used, the demodulated signals are also sometimes referred to as "optical rotation" although in reality they are proportional to the demodulated $I_X - I_Y$.

Chapter 4

Magnetometer Operation

In this Chapter I describe the different ways in which the magnetometer was operated. Some of these modes of operation were applied to further experiments, which are reported in Chapter 5. Some of the modes were simply used to perform a basic characterization of the magnetometer and to compare with the results of other groups which were discussed in the literature review in Chapter 2.

The main purpose of this Chapter is to give an overview of the many parameters which can affect the performance of the magnetometer. Chapter 5 goes into further detail on studies of specific performance metrics under modification of additional parameters.

The main operation modes of the magnetometer reported in this Chapter are:

- Near-zero-field operation. In this mode, the magnetic field must be swept in order to calibrate the magnetometer. The dynamic range of the magnetometer in this case is $|B_z| \lesssim 0.2$ nT.
- Amplitude modulated NMOR, which itself was used in two distinct modes:
  - Continuously pumped (a.k.a. forced oscillation) mode. In this mode, the amplitude of the pump beam was modulated continuously and the optical rotation signal was demodulated resonantly at the same frequency.

– Free-induction decay (FID) mode. In this mode, the amplitude of the pump beam is modulated for a time and then switched off. The oscillation frequency of the optical rotation signal is then measured non-resonantly.

In these modes, the magnetometer was generally operated at 0.2 μT or 1.0 μT, which is of considerably more relevance to the nEDM experiment.

In Chapter 5, most of the measurements will relate to our studies using FID mode. The exception is that some degaussing studies will be done near zero field and hence will use that mode.

4.1 NMOR near zero field and degaussing studies

During this measurement the pump beam was switched off and the probe beam is used as its own pump.

I used the magnetometer in this mode to study the function of the degaussing system described in Section 3.7.2.

The experiment was carried out as follows:

1. The laser beam was tuned for maximum optical rotation and stabilized using the DAVLL system. The beam power was ~ 20 μW.

2. Optical rotation of the probe beam was monitored throughout the experiment via an oscilloscope monitoring the differential photodiode signal.

3. The innermost magnetic shield was degaussed with various parameters for the sequence. The operation of the degaussing circuit was described in Section 3.7.2. After completing the degaussing sequence a switch is opened to electrically isolate the degaussing coil.

4. The magnetic field along the z-direction (defined in Section 3.7.3) is swept in order to calibrate the differential photodiode signal as a function of applied B_z. In this way the initial magnetic field after degaussing may be deduced.

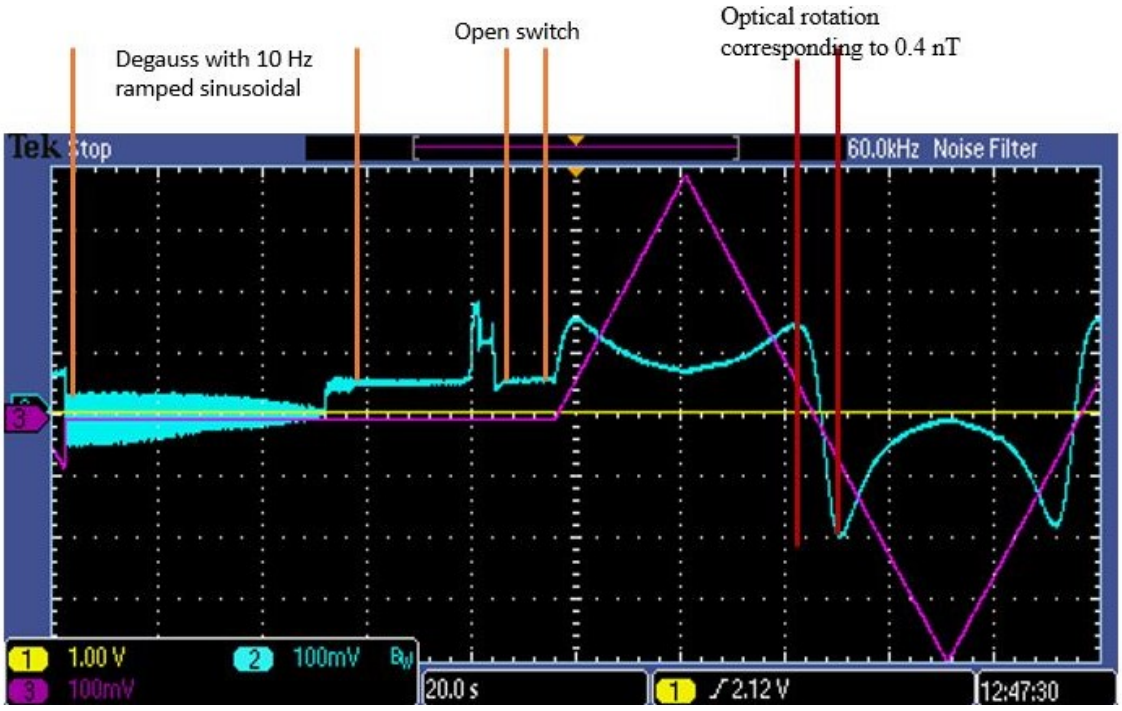

Figure 4.1: Oscilloscope trace of measurement OR near zero field. The purple curve shows the voltage across the 10 kΩ resistor in series with the z-coil, from which the magnetic field ramp of 1.9 nT peak to peak can be deduced. The blue trace indicates the differential photodiode signal which is proportional to the optical rotation. The left side of the traces show the impact of the degaussing procedure, while the right side shows the calibration procedure.

Fig. 4.1 displays the sequence of measurement events in time, along with the differential photodiode signal (in Volts), which is proportional to optical rotation. Also shown is a voltage applied to the z-coil with a 10 kΩ resistor in series which dominates the resistance of the circuit. Recall that the coil constant of the z-coil is ~ 48 nT/mA (see Section 3.7.3). The sweep range of this trace is therefore 1.9 nT peak to peak.

In the first section of the oscilloscope trace, the impact of the degaussing procedure inducing noise in the optical rotation signal can be seen. The next section involves the ramping down of a variable resistor, followed by opening the switch to isolate the degaussing coil. Then the magnetic field B_z is swept and the characteristic dispersive Lorentzian shape of NMOR is observed.

In this measurement NMOR signal is used to determine effectiveness of degaussing pro-

cedure. After the degaussing procedure the observed OR signal is non-zero while the applied field B_z was zero which indicates the existence of a remnant field. The effect of degaussing parameters sensed by the magnetometer is discussed further in Section 5.5.

Fig. 4.2 shows an example of the calibration of the differential photodiode signal to the field applied by the z-coil, for data where the degaussing part of the sequence have been removed. The field is calibrated to the voltage signal as described above. In Fig. 4.2, the data have been fitted to a dispersive Lorentzian shape given by the function

$$\text{Signal (V)} = \frac{a(B - B_0)}{1 + a(B - B_0)^2} \cdot l + C, \tag{4.1}$$

where a, B_0, C, and l are fit parameters. A key measure of magnetometer performance is the valley-to-peak distance, which in this case is about $\Delta B = \frac{2}{a} = 0.49$ nT. The other key measure in this case is the deduced field at zero crossing given by the fit parameter $B_0 = 0.019$ nT. Thus, after degaussing, a remanent field of 19 pT is found. This is only the on-axis field. It is possible that transverse fields can be larger, and these tend to make the width ΔB of the zero-field curve larger.

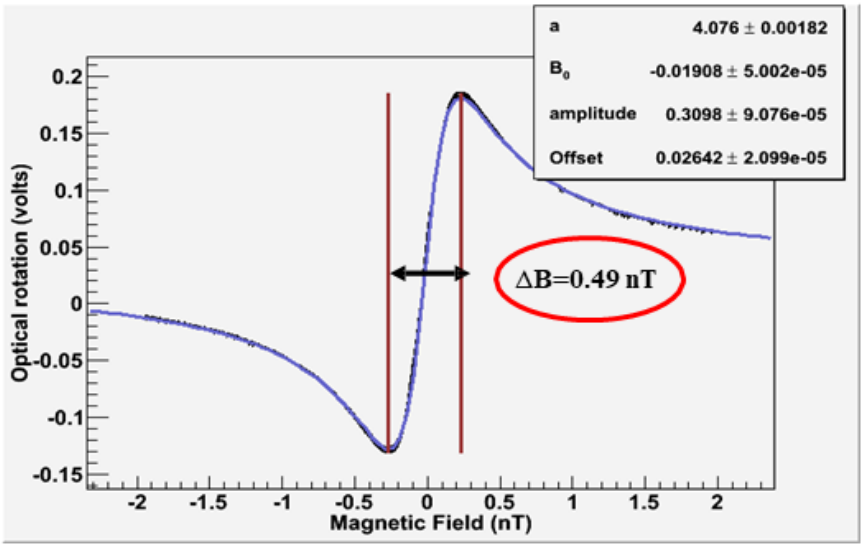

Figure 4.2: Optical rotation as a function of magnetic field applied along the direction of the laser beam. The signal looks like a pure dispersive Lorentzian curve. The measured resonance width is 0.49 nT and the measured remanent field is 0.019 nT.

In order to determine the sensitivity, a magnetometer can be operated in different modes. Most of them found their application during the time this Master's thesis was prepared. Although the main focus of this work was to study magnetometer performance in Free Induction Decay (FID) mode.

4.2 Amplitude Modulated NMOR: Forced-Oscillation Mode

In forced-oscillation measurement mode, the pump beam amplitude is modulated and the differential photodiode signal is demodulated at the same frequency Ω_m using a lock-in amplifier. The modulation/demodulation frequency is near twice the Larmor frequency of the atoms in the magnetic field.

For a forced-oscillation scan, a frequency range and frequency increments are entered into a custom Python code. Via a USB connection, the function generator driving the AOM is set to the appropriate frequencies in sequence. This thereby changes frequency of modulation Ω_m of the pump beam in the magnetometer. The reference signal of the function generator is used as the reference signal for the lock-in amplifier. The differential phototdiode output is demodulated at the reference frequency. The resulting in-phase (X) and quadrature (Y) outputs are collected from the lock-in amplifier by the Python code via GPIB. A settling time of at least 5 lock-in time constants ensures that no memory of the previous frequency is retained by the lock-in amplifier.

Fig. 4.3 shows an example of the resultant X (red) and Y (blue) outputs for the various Ω_m settings. The range of drive frequencies used in Fig. 4.3 was 9.31 kHz to 9.409 kHz, corresponding to an applied magnetic field of $\sim$ 1 μT directed along light propagation direction. The pump beam was modulated with a square wave with duty cycle 1%. The small duty cycle is used to reduce the influence of the pump beam on the probe measurement.

As can be seen in Fig. 4.3, the X output reaches a maximum and the Y output crosses zero near $\Omega_m = 2\Omega_L$. The data are fitted in order to determine the resonant frequency and

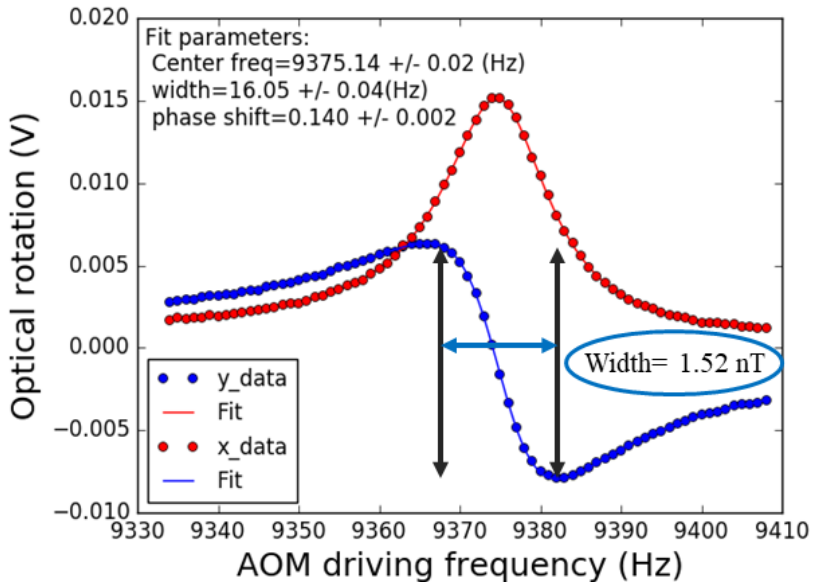

Figure 4.3: Demodulated components of the differential photodiode signal, as a function of the forced-oscillation frequency. The red points indicate the demodulated X output. The blue points indicate the Y output. The data are fitted using the fit function described in the text in order to determine the resonant frequency. The results of the fit are shown in the red curve drawn through both the X and Y points. The fit parameters for this fit are shown in the legend of the graph and are discussed further in the text. The vertical lines indicate the peak-to-valley distance in frequency, and are translated into a magnetic field width of 1.72 nT using the gyromagnetic ratio.

other parameters.

The functions being fitted simultaneously are [21]:

$$\phi_Y = \frac{A_0(f-f_0)\Delta f}{2(f-f_0)^2+(\Delta f)^2/4}\cos\theta - \frac{(\Delta f)^2 A_0}{(f-f_0)^2+(\Delta f)^2/4}\sin\theta + C \tag{4.2}$$

and

$$\phi_X = \frac{A_0(f-f_0)\Delta f}{2(f-f_0)^2+(\Delta f)^2/4}\sin\theta + \frac{(\Delta f)^2 A_0}{(f-f_0)^2+(\Delta f)^2/4}\cos\theta + D. \tag{4.3}$$

Here, $\phi_{X,Y}$ represent the lock-in amplifier outputs, which are measured as a function of frequency f. The fit parameters are: A_0 which represents the maximum amplitude of the purely absorptive curve, Δf the width of resonance (FWHM), f_0 the central resonance frequency, a phase shift θ and offsets C and D.

For the fit presented in Fig. 4.3, the fit parameters are $f_0 = 9375.14$ Hz, $\Delta f = 16.05$ Hz, $\theta = 0.14$ radians. The small phase shift θ is likely induced by the finite duty cycle of the pump beam, and small time delays in the system. The offsets C and D are small, and are likely induced by small voltage offsets in the oscilloscope or lock-in outputs (which can be re-zeroed freely).

A technical detail of the simultaneous fitting process is that the ϕ_X and ϕ_Y data are catenated into a single array of values, which are then fitted in different regions using the two different functions above, in a single overall least-squares fit. The process is similar to that described in Ref. [21].

Based on this measurement, the magnetic field is 1.004318 μT which is translated from central frequency $f_0 = 9.37514$ kHz. The corresponding B-field uncertainty is 2.1 pT. The error calculation is done by chi-square minimization and based on the assumption that data are statistically distributed. The width $\Delta f = 16.05$ Hz is important, because the narrower the width, the more precise the measurement of the magnetic field would be. The width can also be translated into magnetic field using the relation $\Delta B = \Delta f/2\gamma$ where γ is the gyromagnetic ratio of Rb as discussed in Section 2.1. This results in a value of 1.72 nT for

the width.

In general, measurements of the magnetic field that are a factor of a thousand more precise than the width are possible in forced oscillation mode. As discussed in Chapter 2, in Ref. [21], a statistical precision of about 0.17 pT was achieved in scans of this form. Rather than fully optimizing this method, we decided instead to focus on the free-induction decay mode of operation, described in the next section.

4.3 Free Induction Decay

The focus of this thesis was to study the magnetometer operation in free induction decay (FID) mode. In FID mode, the quantum state of the Rb atoms inside the cell is prepared using the pump beam, and then the pump beam is switched off and the precession frequency of the coherent state is measured using the probe beam. The measured precession frequency then determines the field via the gyromagnetic ratio.

Fig. 4.4 shows an example of a pump/probe measurement cycle in FID mode at a field of $\sim 0.2\ \mu$T. The signal in the differential photodiode output is seen to grow when the AM pump beam is switched on. After the pump is switched off, the collection of the FID signal begins. The differential photodiode signal continues to oscillate and decays away exponentially in time. The measurement of the oscillation frequency of the probe beam in the FID signal region gives the magnetic field.

In Fig. 4.4, the differential photodiode signal has been demodulated using a lock-in amplifier whose frequency has purposely been set to be about 100 Hz away from the oscillation frequency of the atoms.

Table 4.1 shows the function generator (fed to the AOM driver) and lock-in amplifier settings for FID measurement at 0.2 μT.

The amplitude of the pump beam is again modulated at $\Omega_m \approx 2\Omega_L$, using again a square-wave with low duty cycle. Generally, the oscillation frequency is adjusted initially to

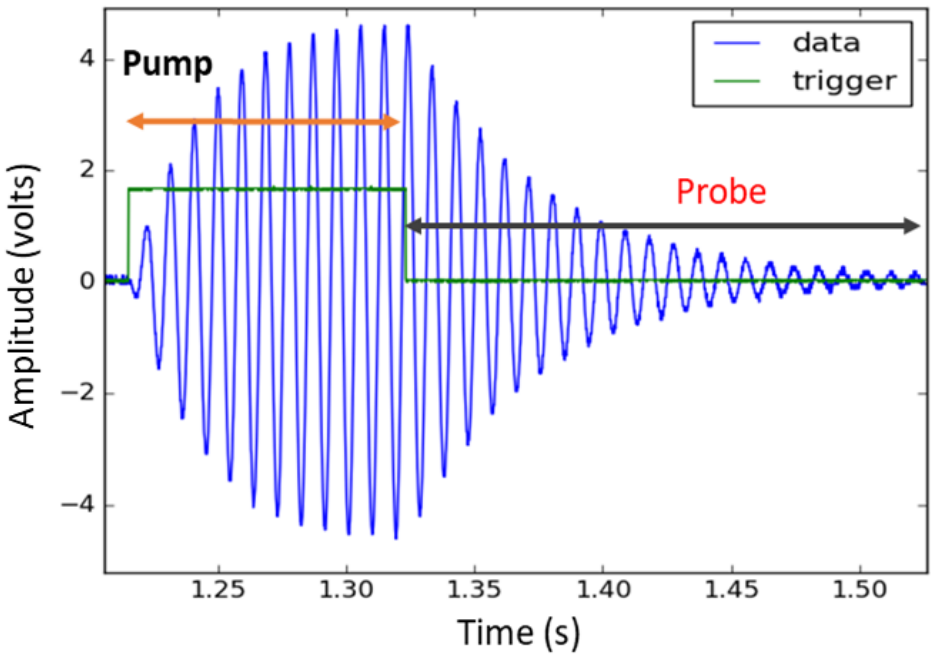

Figure 4.4: Sample FID measurement cycle. The curve labelled "data" (blue) indicates the differential photodiode signal, as demodulated in the lock-in amplifier. Only the X (in-phase) signal is shown. The curve labelled "trigger" is a signal which indicates a non-zero value when the pump beam is on and with the amplitude modulation described in the text. The pump phase is indicated by the orange arrow "Optical Pumping" which persisted for times from 0.0 s to 0.1 s. The probe phase is indicated by the black arrow "FID" which was done for the subsequent 0.2 s. The applied magnetic field during the measurement is 0.2 μT.

SETTING	VALUE
Function generator	
Frequency	2.034 kHz
Waveform	Square
Amplitude	1 V_{pp}
Offset	500 mV
Phase	0°
Trigger	Manual
Burst	220 cycle
Amplitude modulation	On
Lock-in amplifier	
Lock in frequency	1.9439 kHz
Time constant	300μs
Sensitivity	500 mV

Table 4.1: Setting for FID at 0.2 μT field.

maximize the initial amplitude of the FID once the pump beam has been switched off.

The reference signal on the lock-in amplifier has further to be set slightly off resonance ($\sim$ 100 Hz) in internal frequency mode. The frequency offset may be adjusted in order to enhance the number of zero crossing of the FID signal and hence get a better measurement of the beat frequency. In Section 5.7 I study the impact of this setting further.

The X and Y outputs of the lock-in amplifier are recorded using a Tektronix oscilloscope. A Python script may be used to transfer the data from the oscilloscope to computer for further analysis.

In Fig. 4.4, the FID signal recorded by the X channel is sinusoidal with an exponentially decaying envelope, and may be fitted in order to determine the beat frequency ω

$$X(t) = X_0 + Ae^{-(t-t_0)/\tau}\sin(\omega t + \phi_0), \tag{4.4}$$

where X_0, τ, and ϕ_0 are the other fit parameters. The parameter t_0 allows to adjust the start time of the fit. To gain in precision, the signal from the Y channel is also recorded and

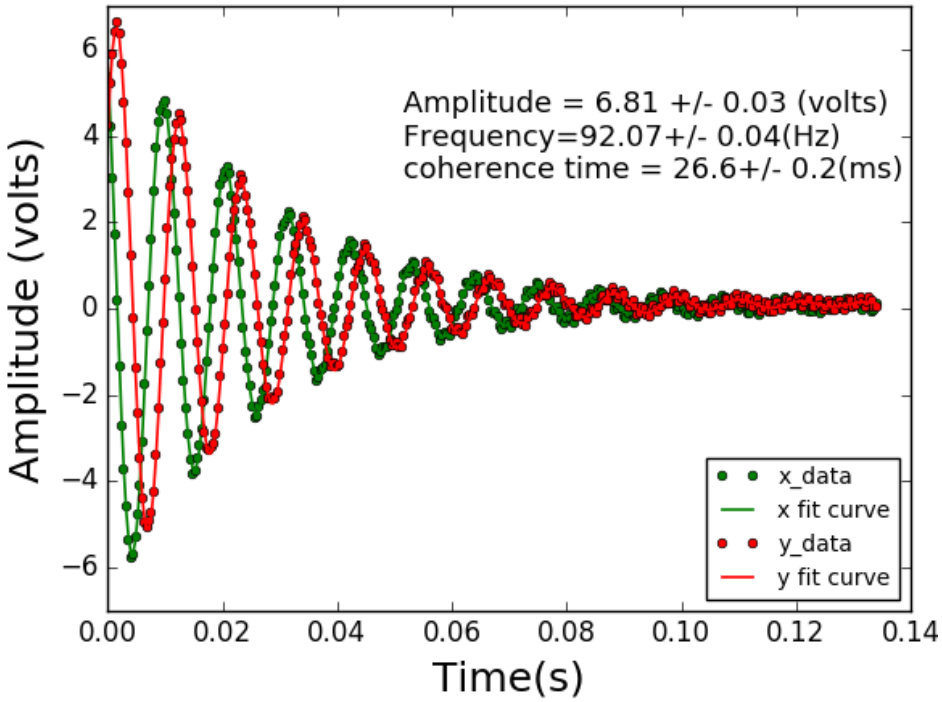

Figure 4.5: Simultaneous fit of X and Y signal. The green and red points are the X and Y data respectively. Green and red lines represent the simultaneously fitted curves. The important fit parameters are displayed in the figure and discussed further in the text. The lock-in frequency setting was $f_0 = 1943.90$ Hz.

may be simultaneously fit to a decaying cosine wave

$$Y(t) = Y_0 + Ae^{-(t-t_0)/\tau}\cos(\omega t + \phi_0), \tag{4.5}$$

where Y_0 describes a possible offset in the Y channel.

Fig. 4.5 shows an example least square fit of a FID signal where both X and Y output of lock-in are displayed.

The data fitting procedure were done in two ways in order to study a variety of systematic effects that were encountered. One method is to take a least square fit of X and Y data separately to a decaying sin and cosine wave respectively. Another way of data fitting is to fit X and Y data simultaneously, which is what has been done in Fig. 4.5. The fit parameters determined in Fig. 4.5 are $A = 6.81$ V, $\tau = 26.6$ ms, and beat frequency $f = 92.07$ Hz.

The fitted oscillation frequency $f = \omega/2\pi$ is then is used to determine the magnetic field

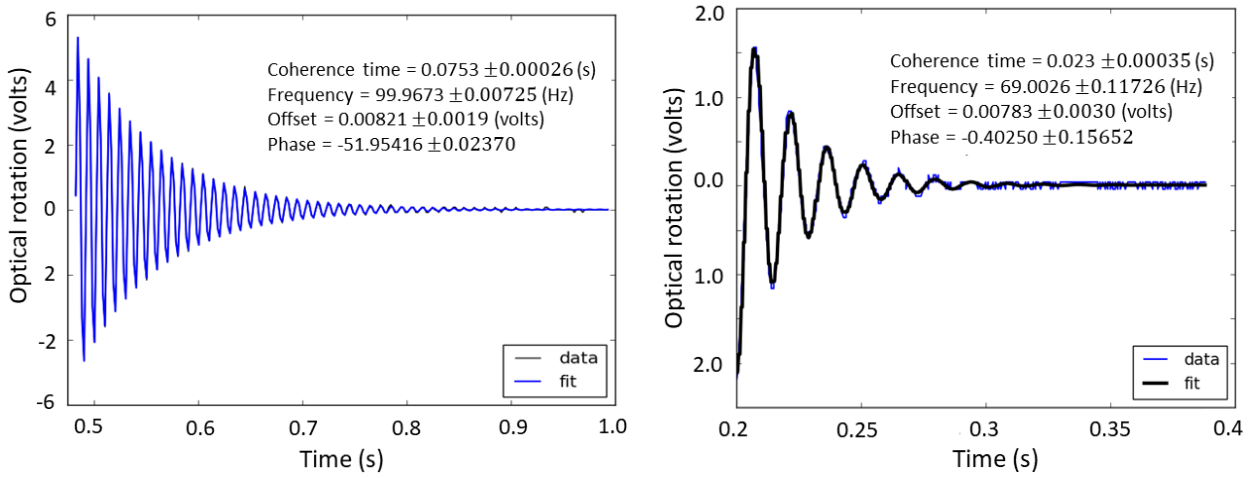

(a) (b)

Figure 4.6: FID measurements obtained with a probe power of 22 μW, pump power of 40 μW (time-averaged over the pump period). The pump and probe beam both are linearly polarized. Acquired at (a) 0.2 μT and (b) 1 μT. The coherence time is larger for smaller field whereas for larger magnetic field the coherence time becomes small. (Note that the time base is different for each FID.)

via

$$B = \frac{f + f_0}{2\gamma} \tag{4.6}$$

where f_0 is lock-in frequency setting and γ is the gyromagnetic ratio of Rb vapor (see Section 2.1). The calculated value of the magnetic field for Fig. 4.5 is 0.218105 μT while the uncertainty in field is 4 pT. The field uncertainty is large because during this measurement the beam power was not optimized. For optimized pump power I was able achieve B-field uncertainty below 1 pT (see figure 4.6a). The error calculation is done by chi-square minimization and based on the assumption that data points are statistically distributed.

The magnetometer can also be operated at 1 μT in FID mode. Fig 4.6 shows the FID signal for two different field. At 0.2 μT field the coherence life time τ is 75 ms and when the applied magnetic field is 1 μT, τ is 23 ms. It is natural for τ to depend on field because it may be limited by spin-exchange collisions in the Rb vapour and/or by magnetic inhomogeneity which is also generally worse at larger fields.

Generally we operated the magnetometer at either 0.2 μT or 1.0 μT during most of our

measurements. The design magnetic field for the nEDM experiment is 1.0 μT.

4.3.1 FID in a tilted magnetic field

The magnetometer as presented is a scalar magnetometer. The precession frequency being sensed is proportional to the local scalar field. However, as shown in Ref. [38] , magnetometers of this sort can also be used to sense the component of fields transverse to the laser beam axis.

Being able to sense transverse fields could have applications in nEDM experiments, as discussed in Chapter 2, Section 2.3. One example is that it could give more information about magnetic field gradients, which may generate false EDM's. Another example is that it could determine gradients that do not have any z-component. Although these do not generate any false EDM's, the uncertainties in these difficult to measure fields tend to drive transverse field corrections when comparing the comagnetometer and neutron precession frequencies. In past experiments, the transverse field correction was measured using fluxgate magnetometers.

Recall from Section 2.3, in the work of Ref. [38] , it was discovered that resonances in continuously driven FM-NMOR occur at both $\Omega_m = 2\Omega_L$ and $\Omega_m = \Omega_L$, where the growth of the resonance at $\Omega_m = \Omega_L$ signifies a tilted field in the plane defined by the polarization axis and the beam propagation direction.

In our experiments, we know that the polarization axis must be either at $\pm 45^{\circ}$relative to the horizontal plane. We positioned our two coil sets (our x- and y-coils) close to this orientation. As shall be described, we saw this growth of the resonance for $\Omega_m = \Omega_L$ for one of the coils (the y-coil) and therefore we assume this must have defined the polarization direction.

Based on this, we defined a coordinate system for these measurements. The z-direction is the direction of propagation of the laser light. The y-direction is the incident laser polarization direction (or the direction of the y-coil). The x-direction points perpendicular to the

plane defined by these directions (or the direction of the x-coil). A tilted field oriented in the yz-plane is defined by the one has an observable effect.

Our goal was to learn to make tilted field measurements using the pump-probe (FID) measurement scheme above. When making our tilted field measurements, we used the same pump-probe scheme as described in Section 4.3, with a few key changes to mimic the setup of Ref. [38]. In addition to modulating the pump beam at $\Omega_m \approx 2\Omega_L$, we conducted measurements also at $\Omega_m \approx \Omega_L$. In order to see the effect on the FID signal, we purposely did not use the lock-in amplifier to demodulate the signal but rather recorded the differential photodiode signal directly in the oscilloscope. A Python script was used to transfer the data presented on the oscilloscope screen to the computer for further analysis.

Fig. 4.7 shows oscilloscope traces of such measurements. The magnetic field has been oriented in the yz-plane at an angle of 15° relative to the z-axis (the beam axis). In the upper trace of each scope screen-shot, the entire pump-probe cycle may be seen. In the lower trace, the scope trace has been zoomed in on the FID measurement region.

In Fig. 4.7(a), the modulation frequency has been set near Larmor frequency of the total field. In the FID, two frequency components can clearly be seen. The dominant component is at $2\Omega_L$ and the component arising due to the tilted field is at Ω_L. The phase relation between the two components is consistent with that measured by Ref. [38] . Fig. 4.7(b) shows the FID for an excitation frequency near $\Omega_m = 2\Omega_L$. The component in the FID at Ω_L has disappeared.

While the data are reminiscent of the previous work of Ref. [38], to our knowledge they represent the first measurement of a tilted field using FID mode. An interesting aspect not discussed in Ref. [38] is the persistence of the $2\Omega_L$ component even when the modulation frequency is near Ω_L. We analyze data as a function of tilt angle in both the yz- and xz-planes further in Section 5.8.

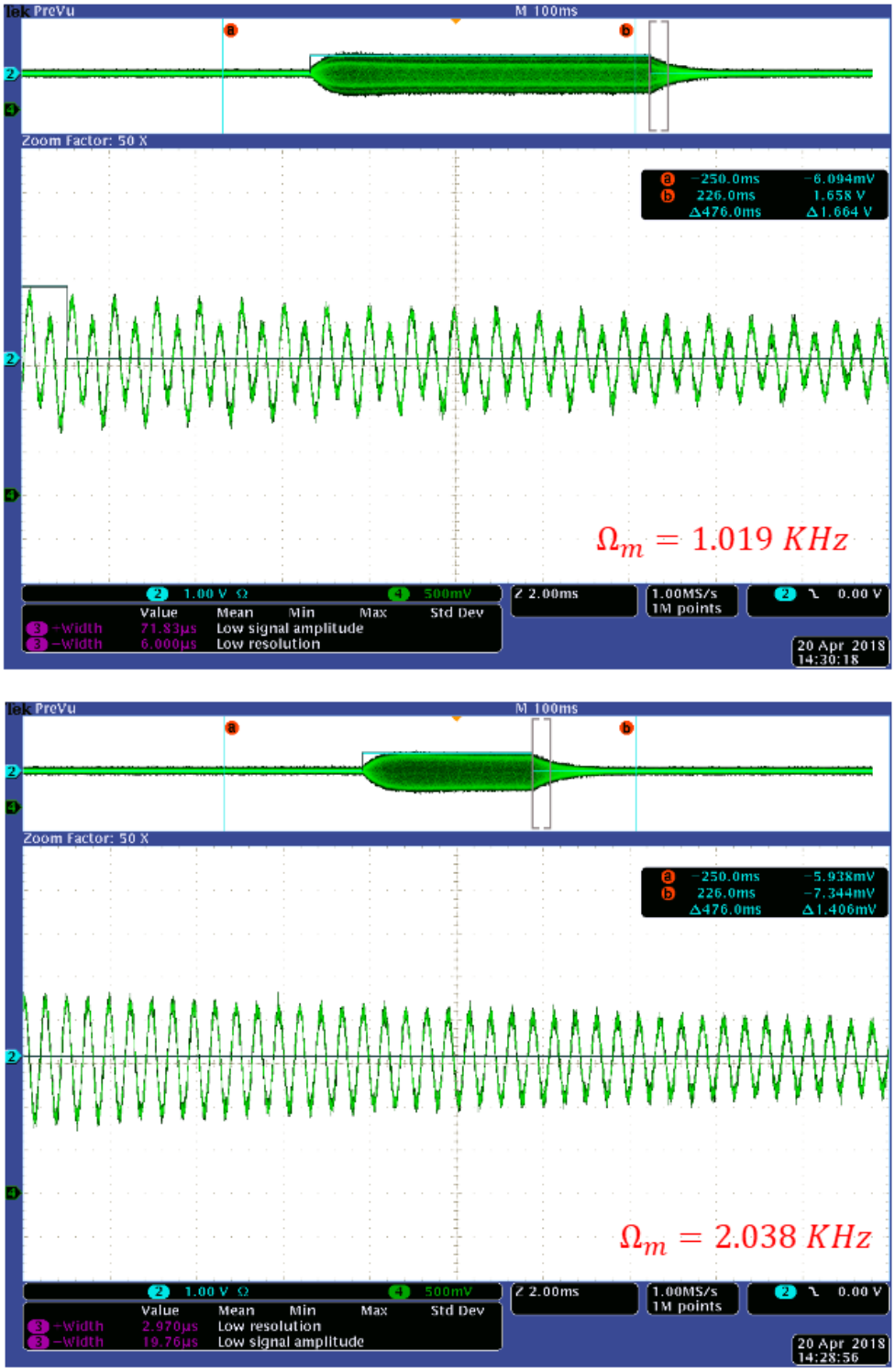

Figure 4.7: (a) Optical rotation as a function of time at Ω_L in the yz plane at tilt angle 15° with light propagation direction. (b) Optical rotation as a function of time at $2\Omega_L$ for same tilt angle.

Chapter 5

Experiments using the magnetometer

In this Chapter, I present the main results on measurements of the properties of the magnetometer, optimization studies, and applications of the magnetometer to characterize magnetic fields. The main studies that are presented are:

- Measurements of magnetic fields over long timescales using FID mode.
- Adjustment of the pump and probe timescales in order to measure the field faster.
- Magnetometer drift compared with drifts in the coil current and room temperature. This study aimed at finding sources of drifts.
- Studies of degaussing, which in part tell the story of our degaussing development and learning. This includes studies of:
  - the degaussing setup and testing it near zero field
  - initial operations at non-zero field, and
  - final degaussing procedure, in which degaussing the next to innermost shield was studied.
- Studies of laser locking and tuning, and the requirements on tune stability

- Studies pushing below 1 pT in an individual FID measurement. This includes adjustment of the pump and probe powers, and lock-in amplifier settings. As will be shown, this study revealed problems in the procedures used to determine the precession frequency at such high precision and suggests avenues for further study.

- Finally, I show my studies which revealed a way to use FID mode to measure transverse fields.

Each study will now be presented in turn and conclusions will be summarized in Chapter 6.

5.1 Long-term FID measurements

A forced-oscillation scan or an acquisition of a single FID give a measurement of the magnetic field within a relatively short time period (< 1 s). For nEDM experiments, it is important to get information about the change in the average magnetic field over time periods of 100 s and longer.

In order to study the fluctuations and drifts in the magnetic field over time, and to search for possible drifts in the magnetometer itself, repeated measurements of FID's were made and recorded.

During this long term process the laser frequency was tuned for maximal FID amplitude, and locked using the DigiLock 110 module. In order to observe the FID signal, a Tektronix DPO 2014 oscilloscope was connected to X and Y output of output of lock-in amplifier. A Python script was used to set up the function generator and to trigger data acquisition using the oscilloscope. The same script is also used to transfer data continuously from oscilloscope to the computer. For further data analysis another Python script was used to process each FID. A least-squares fit was done for each FID for each X and Y pair. The measured oscillation frequency of the decaying oscillating signal was then converted to magnetic field using Equation (4.6).

The magnetometer settings for these runs were: Pump power ~ 40 μW, pump time 0.49 s,

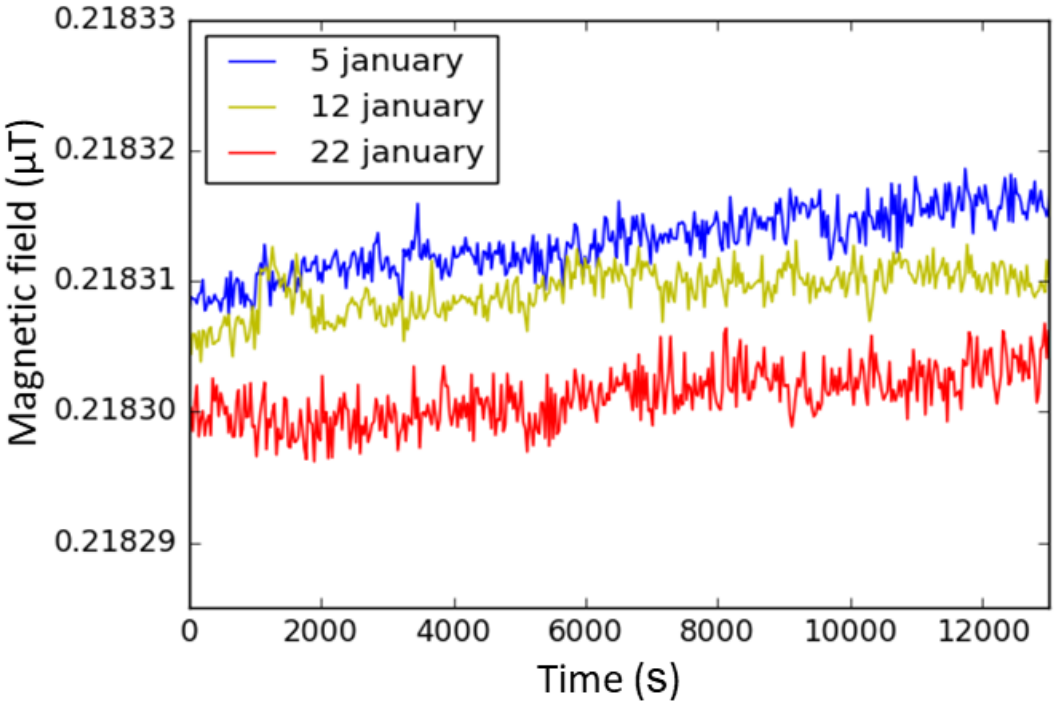

Figure 5.1: Magnetic field recorded over 4 hours on three different days. The observed field drift is similar ($\sim$ 15 pT) for each day.

probe power $\sim$ 20 μW, probe time 0.5 s, lock-in frequency is 1929.5 Hz, AOM frequency 2038 Hz, and lock-in time constant 300μs.

Fig. 5.1 shows the magnetic field recorded over 4 hours on three different days. Each data points in the graph corresponds to a single FID measurement. The observed field drift is similar ($\sim$ 15 pT) for each day. The measurement was conducted at 0.2 μT magnetic field.

The Allan deviation was used to further quantify the long-term stability [12] (see also Appendix A). Allan deviations characterize changes in the measured quantity when the data are averaged on different timescales. When the data behave statistically on short timescales, the Allan deviation is equal to the standard deviation. If drifts occur, normally on longer timescales, the Allan deviation grows linearly with a slope that is $1/\sqrt{2}$ times the slope of the drift in time.

Fig. 5.2 shows the Allan deviations of the measurements field presented in Fig. 5.1. The minimum in the Allan deviation occurs when statistical behavior is overtaken by drift. Fig. 5.2 shows that this transition generally occurs after 10-60 s of averaging, corresponding

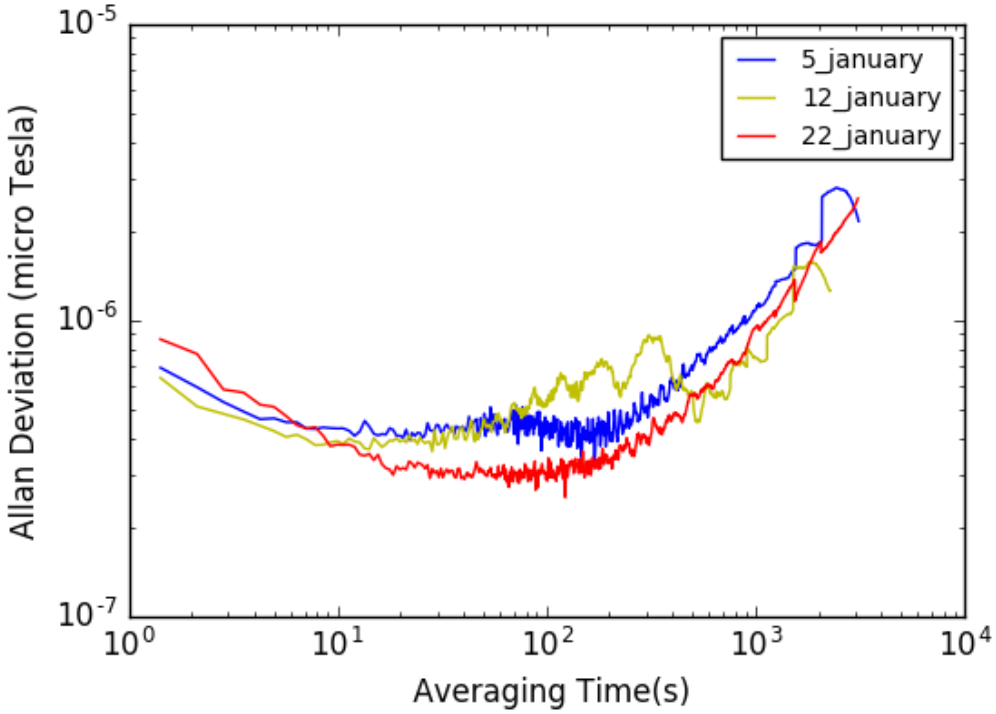

Figure 5.2: Allan deviation of recorded magnetic field vs. averaging time for the time-series data presented in Fig. 5.1.

to a precision in magnetic field of 300-500 fT at the Allan minimum.

For an nEDM experiment, the goal precision is $\sim$ 20 fT for the average field over the 100 s neutron free-precession measurement cycle. This is not likely to be equivalent to the Allan deviation minimum of our one magnetometer, because the long-term drift is driven in part by the drift of the magnetic field within the shield. The goal of subsequent work was:

- to attempt to identify some of the sources of drift. This included searching any sources that might be caused by the magnetometer itself, but also included the effects of room temperature,current,degaussing.

- to improve the single FID performance so that fields could be measured faster.

In terms of the Allan deviation, it means trying to move the Allan minimum lower and to the right.

5.2 Optimization of cycle time

The goal of this optimization study was to reduce the cycle time without sacrificing too much precision in the single-FID frequency measurement. If more measurements can be made more quickly, the precision of the magnetometer over time would be improved.

During this study the magnetometer was operated in FID mode at 0.2 μT field. An example of our initial settings is shown in Fig. 5.3a. The pump time is 0.49 s and the probe time is 0.4 s. The amplitude of the differential photodiode signal is seen to saturate well within 0.1 s. The coherence time, indicated by the decay time of the oscillating signal, is about 0.06 s. Fig. 5.3b shows a more optimized the FID signal for 0.1 s pump time and 0.2 s probe time.

In Fig. 5.4 a histogram of measured magnetic fields by making subsequent measurements over 100 s is shown for different pump times. The longer pump time is 0.49 s (5.4(a)) and the shorter one is 0.1 s (5.4(d)).

From Fig. 5.4, the pump time, when varied over this limited range, does not strongly affect the precision of the individual FID measurements. However, it allows us to take measurements faster because previously the duration for one FID measurement was 1 s while after optimization it only takes 0.35 s.

It is not surprising that the precision does not change much because the amplitude of the differential photodiode signal during the pump phase has saturated.

5.3 Magnet field compared with current in the z-coil

5.3.1 Current drift

The idea was to determine the impact of possible current drifts. An Agilent B2962A power supply was used to supply DC electrical current to the z-coil. Fig. 5.5 shows the current supplied to the z-coil over a measurement period of 10000 s. The current in the power supply

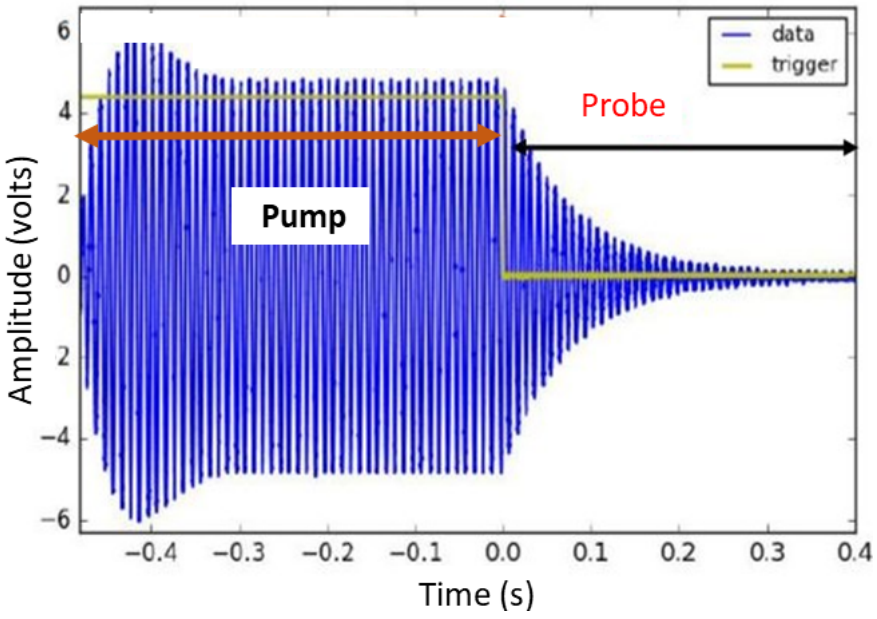

(a)

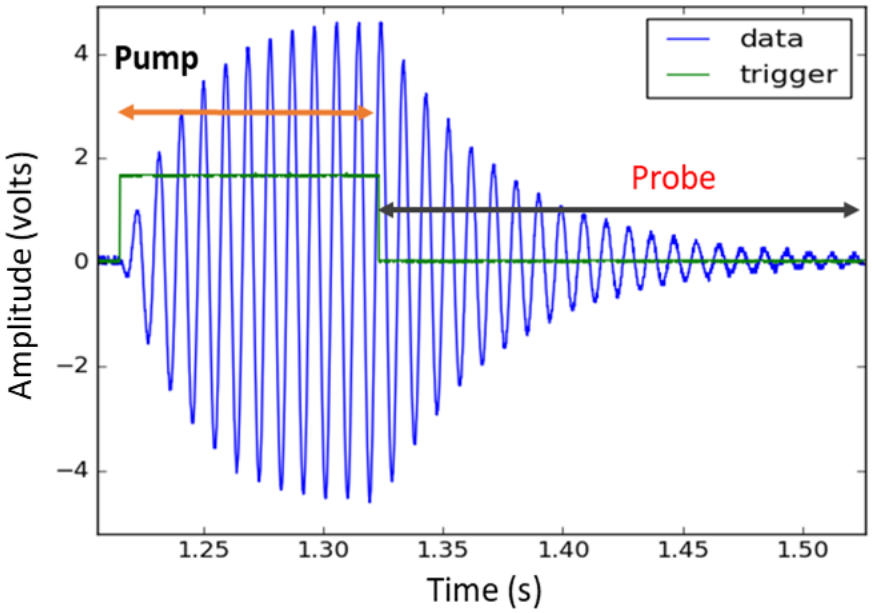

(b)

Figure 5.3: (a) FID signal for pump time 0.49 s and probe time 0.4 s. (b) FID signal for pump time 0.1 s and probe time 0.2 s. Both measurements were conducted at 0.2 μT magnetic field.

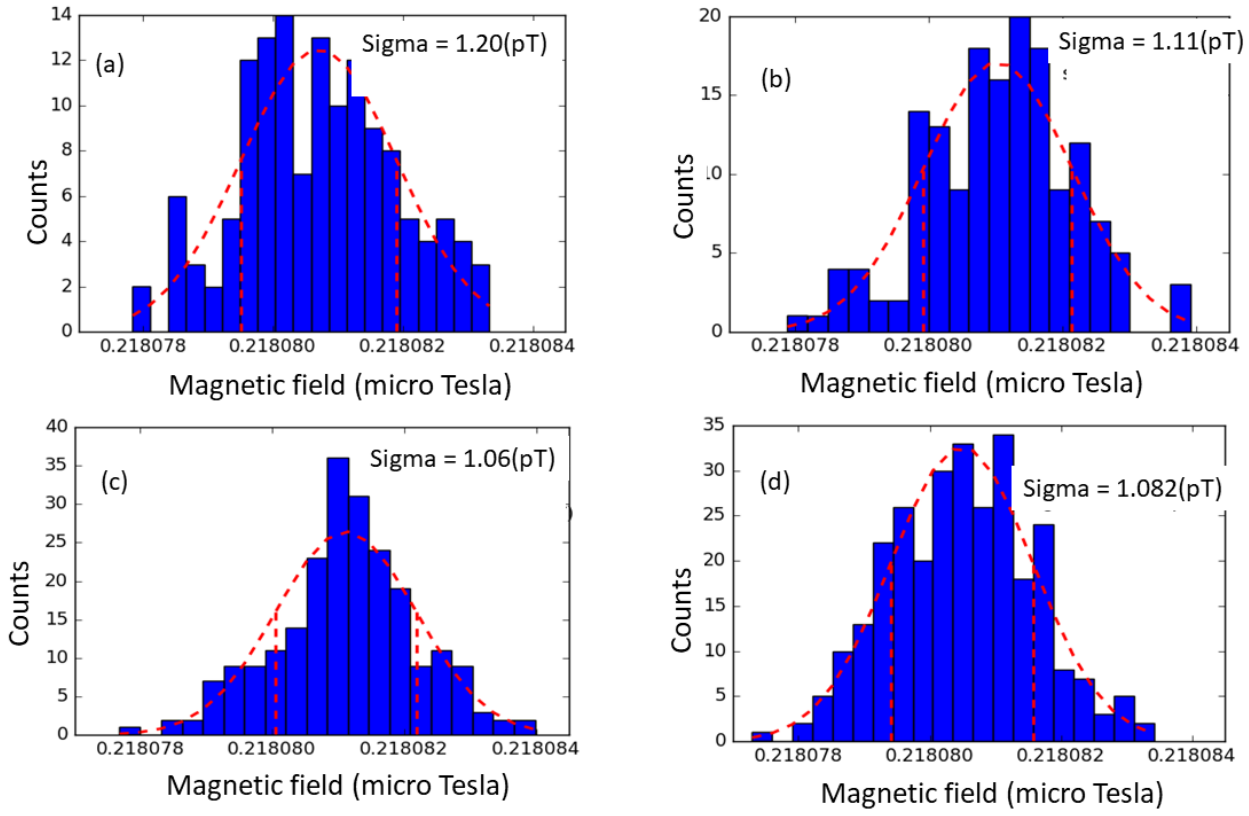

Figure 5.4: Histograms of measured B-field for different pump times. For a measurement time of 100 s. (a) is a pump time of 0.49 s (b) is a pump time of 0.39 s (c) is a pump time of 0.2 s (d) is a pump time of about 0.1 s. The probe time in each case is about 0.25 s. The number of measurements taken in each case is estimated to be (a) 137 (b) 158 (c) 224 (d) 287. The standard deviation of each set of measurements is indicated in the respective figure.

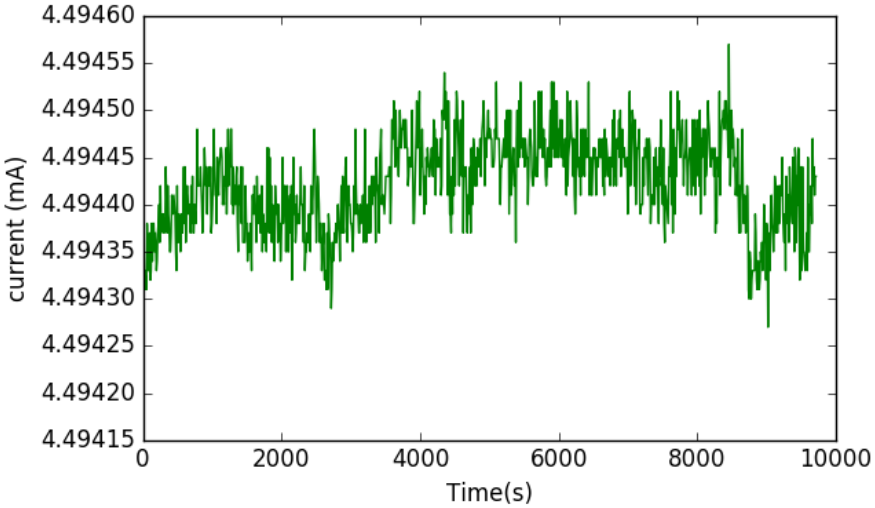

Figure 5.5: Recorded coil current as a function of time when the current source has been set to 4.50000 mA.

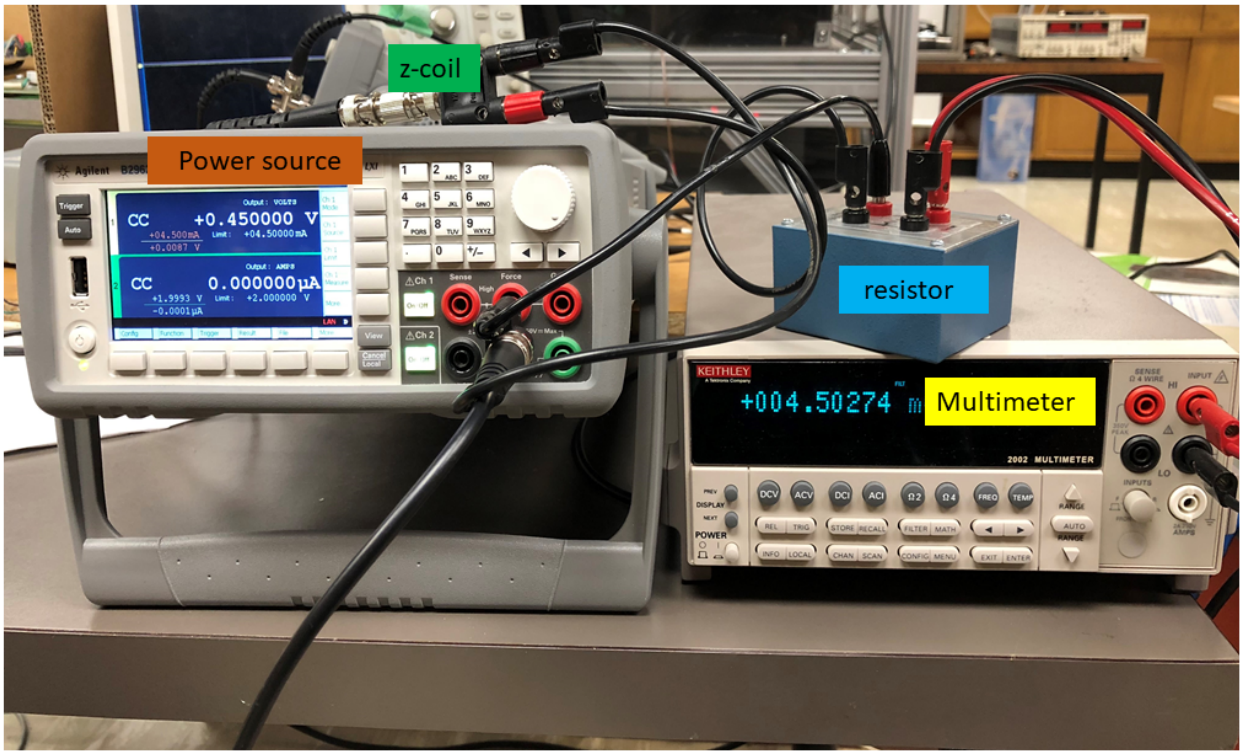

Figure 5.6: Photograph of equipment arrangement used to control and measure the current in the z-coil.

was set to 4.50000 mA, which was operated in a current-controlled mode. The current has been measured by measuring the voltage drop across a Vishay metal-foil 100 Ω resistor in series with the z-coil using a Keithley 2002 8-digit multimeter. A photograph of this system is shown in Fig. 5.6, although with an alternate resistor which we tried. The Vishay resistor is 1% absolute precision, but the values reported in Fig. 5.5 have been converted to currents using an exact value for the resistance of 100.000 Ω. The main feature of this resistor is that it possesses a low temperature coefficient of 2 ppm/°C. Measurements recorded by this system are expected to be reliable on the $\sim \pm 2$ ppm level given the resistor and multimeter being used and the typical temperature fluctuations in the room.

The current of 4.5 mA achieves a magnetic field of 0.2 μT. From Fig. 5.5, the maximum current excursion during the measurement period was 300 nA. Likely these fluctuations are given by the stability of the power supply. Converted to magnetic field, it would represent a $\sim$ 10 pT fluctuation in field. Unfortunately, during this measurement time, the magnetometer

and degaussing system could not be operated sufficiently well in concert with the current measurement system to determine whether or not the current fluctuations were correlated to field changes. Principally this was a problem of the data acquisition system. Clearly, field changes as large as 10 pT should be observable, given the statistical precision of the magnetometer. Future work would be on improving the data acquisition system.

5.3.2 Change in magnetic field driven by larger changes in coil current

A study was conducted to determine the field change by changing the coil current by a known amount. The main objective of this study is to confirm the Rb magnetometer performance on magnetic field measurement. For this measurement coil current was changed periodically by ± 0.001 mA steps. Based on the coil constant, field changes of 48 pT were expected to be observed in the magnetometer, corresponding to frequency shifts of 0.5 Hz.

The laser frequency was tuned for maximum FID amplitude, then locked using the DAVLL system. All other magnetometer settings were similar to the previous studies in Section 5.3.1. During this study the magnetometer has been operated in FID mode. The lock-in frequency was 1950 Hz and time constant was 300 μs. The AOM frequency was tuned initially to maximal optical rotation and found to be 2049 Hz. The probe beam power was 20 μW and pump power $\sim$ 40 μW. The pump and probe times were both 0.5 s. Only X data was fitted to determine the magnetometer frequency.

Fig. 5.7 presents the magnetic field change over time for different coil current. For better understanding Fig. 5.7 has been divide into five different regions where a number of different coil currents were set near 4.50000 mA in steps of 0.00100 mA. It is clear from the figure that the field has been changed by $\sim$ 50 pT on each transition. This measurement proves rather conclusively that changes in the magnetic field with large current changes are indeed reproduced correctly. It should be noted that up to 30 s of data have been omitted near each transition.

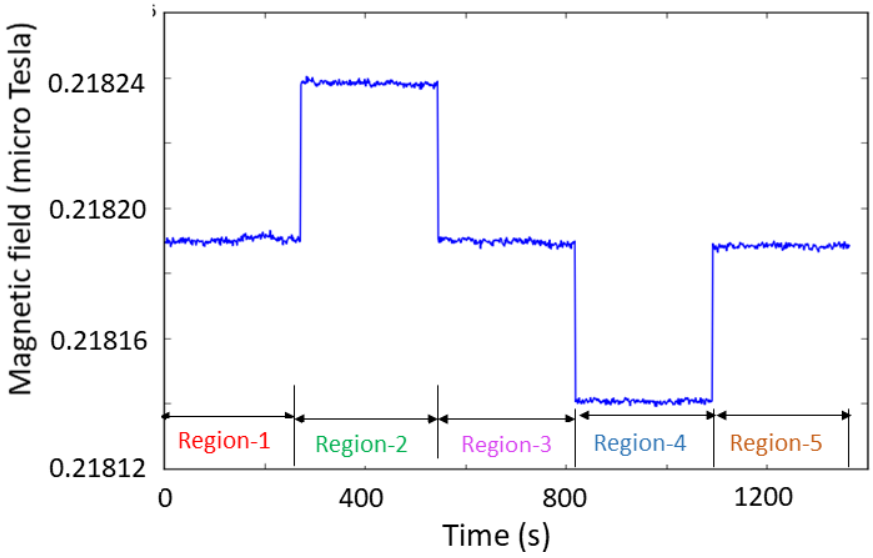

Figure 5.7: Change in magnetic field measured by the magnetometer by step changes in the z-coil current. In Regions 1, 3, and 5, the current was set to 4.50000 mA on the power supply. In Region 2, the current was changed to 4.50100 mA. In Region 4, the current was 4.44900 mA.

5.4 Study the effect of room temperature on magnetic field measurement.

The goal of this study was to search for any correlation between the magnetic field measured by the magnetometer and ambient temperature flucturations near the magnetometer.

Fig. 5.8 displays the measured temperature at various locations vs. time. It can be seen that room temperature fluctuations are 1°C while temperature measured on the outside of the magnetic shielding is about 0.8°C. The optics table is covered by a clean enclosure, which makes the temperature measured on the top of the magnetic shield slightly warmer than the rest of the room. The temperature on top of the shield is measured by a T-type thermocouple that was held to the shield using tape and thermally connected by thermal grease. We often use T-type thermocouples because they are non-magnetic, as opposed to K-type which are magnetic.

For room temperature measurement a precision thermometer was connected to a Agilent

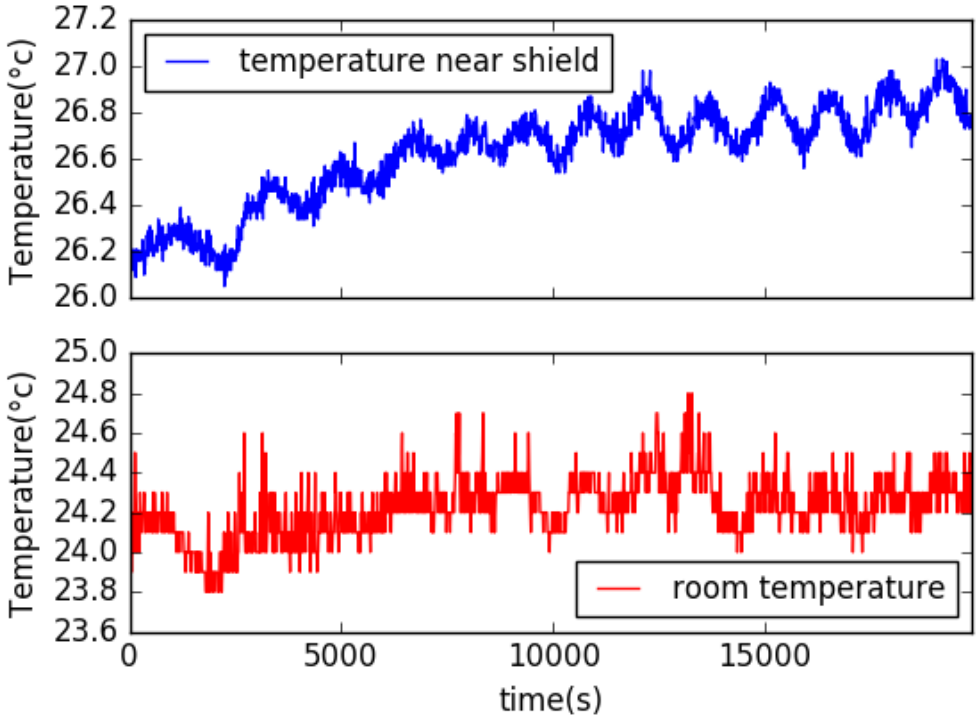

Figure 5.8: Temperature measurements as a function of time. The upper graph (blue) shows the temperature measured on the outermost magnetic shield. The lower graph (red) shows the temperature in the room outside the laser hut, near the power supply and function generator system.

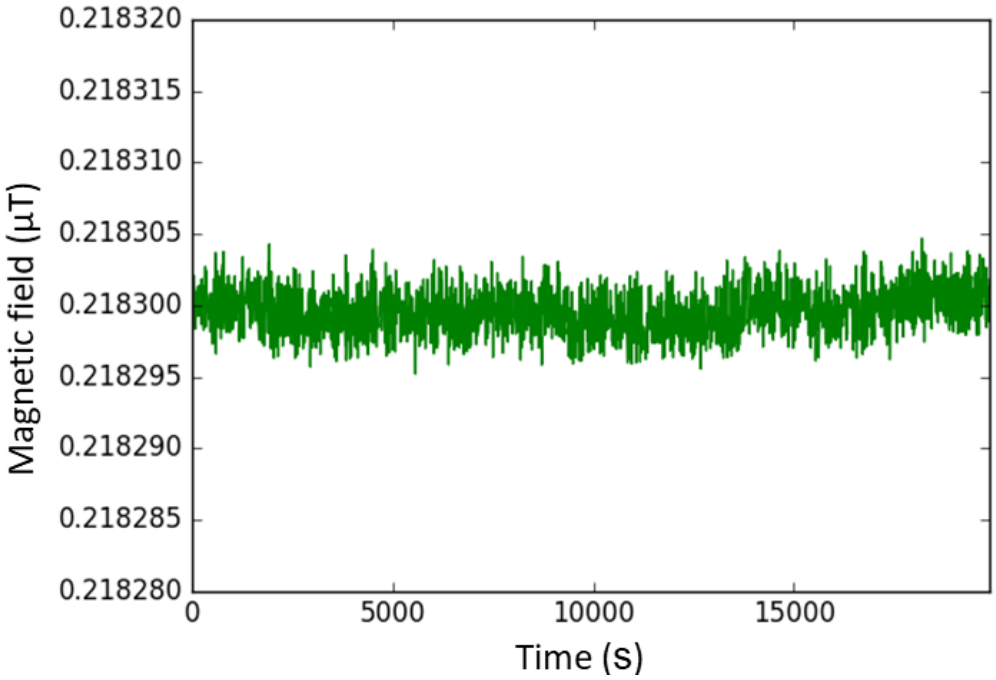

Figure 5.9: Field measurement

34410A $6\frac{1}{2}$ Digit Multimeter. A Python script configured the multimeter for a 2-wire RTD measurement, triggered the meter, and transferred the reading to the computer. The T-type thermocouple on the shield was connected to an Arduino Uno located outside the laser table enclosure. For configuring this device and then transferring the reading to the computer a different part of the same Python script was used. After an acquisition of the two temperatures, the script paused for 10 s, so that measurements came approximately every 12.3 s.

Fig. 5.9 shows the magnetic field measured by the magnetometer in FID mode vs. time in similar times as the temperature measurement was made. The magnetometer settings were the same as in the previous section, with the caveat that the frequency of the AOM was adjusted for best FID amplitude (2036 Hz) and lock-in adjusted to keep the FID demodulated frequency near 90 Hz (1929.5 Hz).

The FID measurements were taken using an oscilloscope. The oscilloscope would be read occasionally. No data is shown twice in Fig. 5.9, but time jumps in the data did occur at random intervals. Thus any correlation with temperature is qualitative. The meausrements

were taken over approximately the same time as the temperature measurements.

The asynchronous data acquisition systems mean that time was defined with factor of 2 level accuracy. Nonetheless, a the correlation of the field measurement is ruled out at approximately the 5 pT/°C level.

5.5 Degaussing studies

5.5.1 Initial tests using the magnetometer near zero field

We used the procedure described in Section 4.1. To remind the reader, the procedure is:

- Initiate the degaussing sequence in one channel of the function generator.
- Once complete, ramp the rheostat to zero and open the switch.
- Pressing a button on the computer initiates the ramp of the z-coil on the second channel of the function generator, which calibrates the optical rotation to field.
- Both the current in the z-coil and the differential photodiode signal are monitored at all times using an oscillscope.

Optical rotation as a function of magnetic field for different sample rate is shown in Fig. 5.10. Recall that the sample rate determines the rapidity with which the 5×10^5 individual samples of the linear degaussing envelope function are stepped through. A sample rate of 10,000/s therefore represents a degaussing time of 50 s. Since the carrier wave in all cases is 10 Hz, it means that 500 cycles were used. The sample rate of 80,000/s represents a degaussing time of 6.25 s and 62.5 cycles.

It should also be noted that the data were acquired in order of increasing sample rate, and that many additional degaussing sequences were conducted which are not shown in Fig. 5.10.

We had expected that larger sample rate would manifest itself as a worse degaussing resulting possibly in worse magnetometer performance. Paradoxically, the resonance width

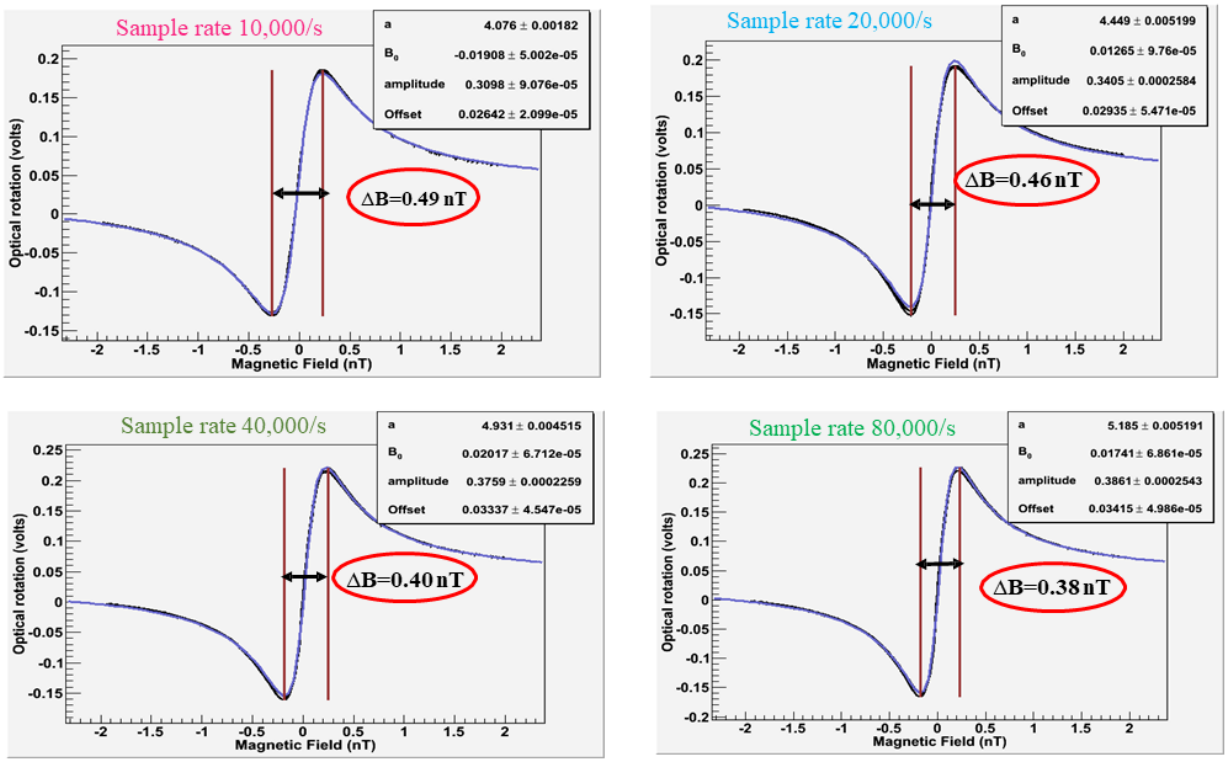

Figure 5.10: Optical rotation vs. measured B-field for different sample rate. The data were taken in order from smaller sample rate to higher sample rate. The numbers written in the red circles indicate the distance in magnetic field from the optical rotation minimum to the optical rotation maximum ΔB, as deduced from the fit parameter a. The fit parameter B_0 indicates the remnant field sensed by the horizontal offset of the dispersive shape, reported in nT.

ΔB, the difference between two peak of the dispersive curve, reduced very slightly as the sample rate was increased. It can be seen from Fig. 5.10 that, the resonance width is about 0.49 nT for sample rate 10,000/s and the resonance width is 0.38 nT for sample rate 80,000/s. This is likely an indication of a small reduction in the transverse fields or generally an improvement the homogeneity of the field. This is consistent with the observation that the amplitude grows slightly, which is another indication of the improved field quality, all other magnetometer settings being equal.

The remnant field B_0 is an indication of the average longitudinal field (along the laser beam axis) and is within 20 pT of zero. It increased with the sample rate from a starting negative value to a positive value.

The conclusion of this study was that additional degaussing, as long as it has a reasonable number of cycles, tends not to affect the field or it might improve slightly the homogeneity of the field. Generally the field is reduced below 20 pT.

5.5.2 Measurements at 0.2 μT and initial studies of the effect of degaussing on field stability

The previous results implied that additional (even poor) degaussing had little impact if the previous degaussing was done adequately. To address this, we began to do studies where the internal z-coil field was purposely ramped to a large value, then reset to a low value for measurements at non-zero field. The idea here was to use the z-coil itself to magnetize the shields, and to measure drifts at non-zero field, which is the chief interest for nEDM experiments.

Fig. 5.11 shows an example of such a study. In all three cases shown in Fig. 5.11, the magnetometer settings are similar in each case. The AOM frequency was adjusted slightly to optimize the FID amplitude for each measurement, but the lock-in frequency and most other settings were left the same.

In the 1st part of this study the magnetometer was operated in FID mode at 0.2 μT field,

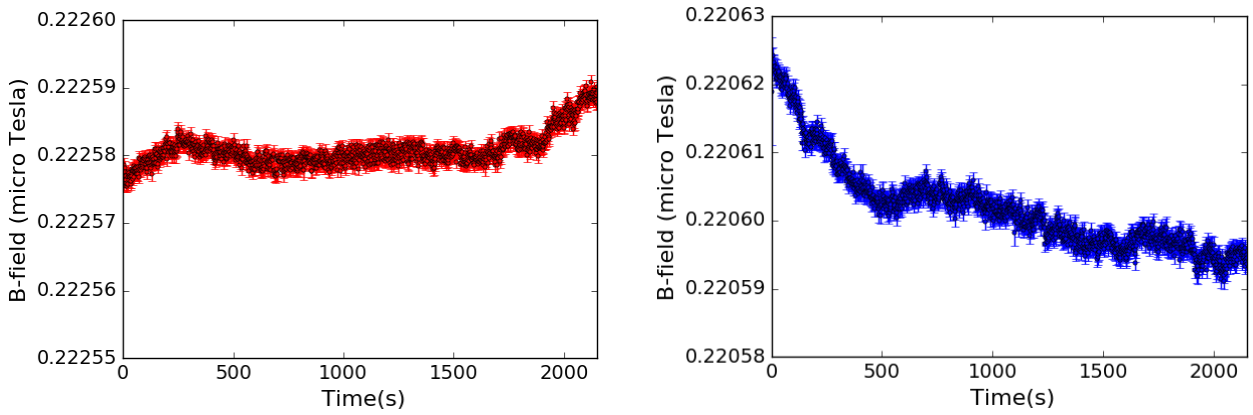

(a)

(b)

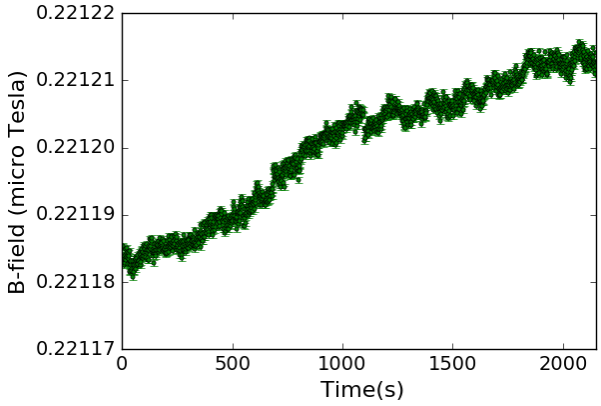

(c)

Figure 5.11: Measurements conducted in time order from (a) to (b) to (c) under different degaussing conditions at $B_z = 0.2$ μT magnetic field: (a) no degaussing, (b) ramp B_z from 0.2 μT to 10 μT then again set it to 0.2 μT and collect FID signal before degaussing, and (c) after degaussing.

at a point in time when the magnetometer had been operated in a quiet shielded environment for at least a month below 1 μT, over the course of which the shield had been degaussed a number of times.

The recorded magnetic field measurement over a 2200 s period in this condition is shown in Fig. 5.11a. It can be seen from Fig. 5.11a that the magnetic field increased linearly for first 300 s then showed a decrease in field. The field was pretty stable between 600 s and 1800 s and after that the field showed an increase. The overall field change is about 15 pT during the measurement. In Fig. 5.11b, data was acquired by ramping B_z from 0.2 μT to 10 μT then down again to 0.2 μT and collect FID signal. Since the z-coil is coupled to the inner shield system, this should magnetize the shields. By doing this field ramping we intentionally perturb the magnetic field environment inside the shield. After this field ramping the long term field measurement has been conducted for another 2200 s. In this case, the field showed a downward drift of about 35 pT. Thus field ramping did seem to change the magnetic environment inside the magnetic shielding.

Finally, for Fig. 5.11c, the innermost magnetic shield was degaussed with degaussing parameters stated in Table 3.2 Before starting field measurement via FID mode degaussing was done multiple times (4-5 times) repeatedly but during the measurement no degaussing was done.

While this changed the direction of the drift, it did not change the magnitude of the drift which was again 35 pT over 2200 s.

During this time we began to develop a hypothesis about magnetic couplings inside the magnetic shielding. We realized that the z-coil, which had been designed to be coupled to the innermost shield, was now more strongly coupled to the second innermost shield. This is because most of the flux in the solenoidal winding exits the end of the innermost shield, whose endcaps have been removed in order to accommodate its degaussing coil.

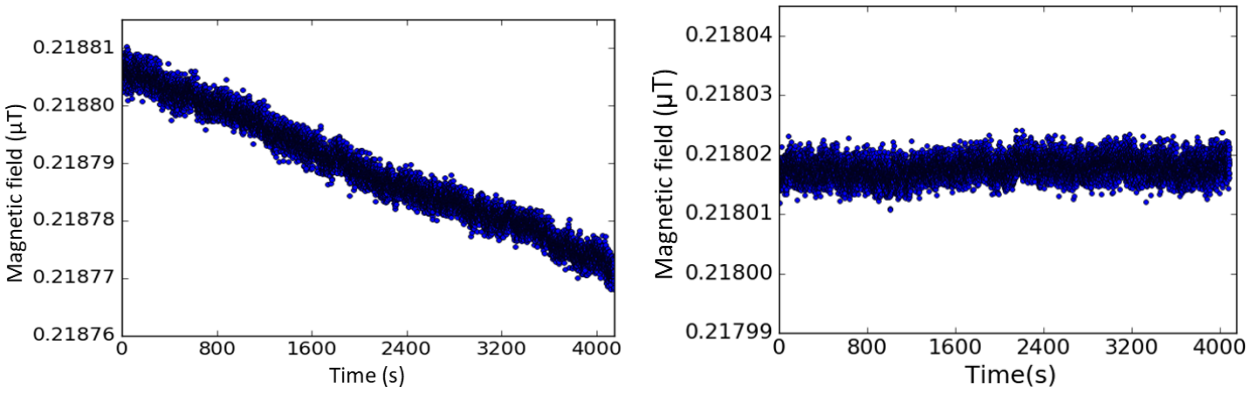

(a) (b)

Figure 5.12: Magnetic field vs. time (a) after degaussing the innermost shield, and (b) after additionally degaussing the remaining layers of magnetic shielding with a single loop of wire wound through all three layers. During this study the signal amplitude was relatively low ($\sim$ 3 V) likely due to poor laser alignment through the AOM or other settings. As a result the fluctuations in magnetic field were larger than the usual 1-2 pT.

5.5.3 Effect of degaussing the three outermost shields

If the system had been kept at low field for several days, the usual field drift was about 15 pT over 3000 s (as discussed in Sections 5.5.2 and 5.1). After doing a transverse field study (applying current to x- and y-coils along with z-coil, like that reported in Sections 4.3.1 and 5.8) the magnetic field environment became even more unstable.

Fig. 5.12b shows about 50 pT drift in magnetic field in 4000 s. Although before start taking field measurement degaussing innermost layer of mu-metal is done multiple times in order to cancel background field inside the shield but still the field drift problem can be seen. Then degaussing the other three shielding layers is done with a single loop of wire wound through all three. The maximum current achieved in this coil was equivalent to the maximum current in the innermost shield deguassing sequence. However since a single loop is wound through all three outermost shields, it is unlikely that any of the three shielding layers are ever saturated. Nonetheless, this seemed to reduce the field drift after degaussing the outer three shielding layers, as shown in Fig. 5.12b. During those measurements the lock-in reference frequency was set to 1938.5 Hz and lock-in time constant is 300 μs.

The conclusion is that degaussing the outer three shields is equally as important as the degaussing of the innermost shield. This is not surprising since the endcaps of the innermost shield were removed.

Our current degaussing system was designed after the magnetic shields and the inner coil systems had been designed. Based on my work, a clear recommendation to future designs is to design the degaussing system at the same time as the magnetic shielding. A key requirement of EDM experiments is field stability which is totally driven by the ability to degauss reproducibly.

5.6 Laser tuning

In the course of tuning the laser for maximum FID amplitude, some studies were conducted where the laser was purposely mistuned in order to check the effect on the measured FID fit parameters. In general, for the particular magnetometer settings otherwise in use, it was found that detuning from the maximum amplitude tended to increase the coherence time (1/e decay time of the oscillating FID signal), although on occasion shorter coherence times could be observed. By taking measurements in rapid succession, it was also found that the FID frequency did not change considerably at the 0.01 Hz (sub-pT) level.

We started doing studies like this because there was some (mistaken) belief that the laser tune significantly altered the FID measured frequency. This was based on data like that shown in Fig. 5.13.

Fig. 5.13 indicates a 120 pT drift in magnetic field over 12 hours. The laser frequency is believed to drift because the amplitude of the FID decreased by a factor of 2.5 over the course of the measurement, while the resonant frequency only changed by 1.5 Hz. The fact that the amplitude has decreased is indicated by the relevant fit parameter which is not shown, but can be seen from the additional statistical noise on the field measurements at long times compared to short times. The question was if this possible drift in tune was

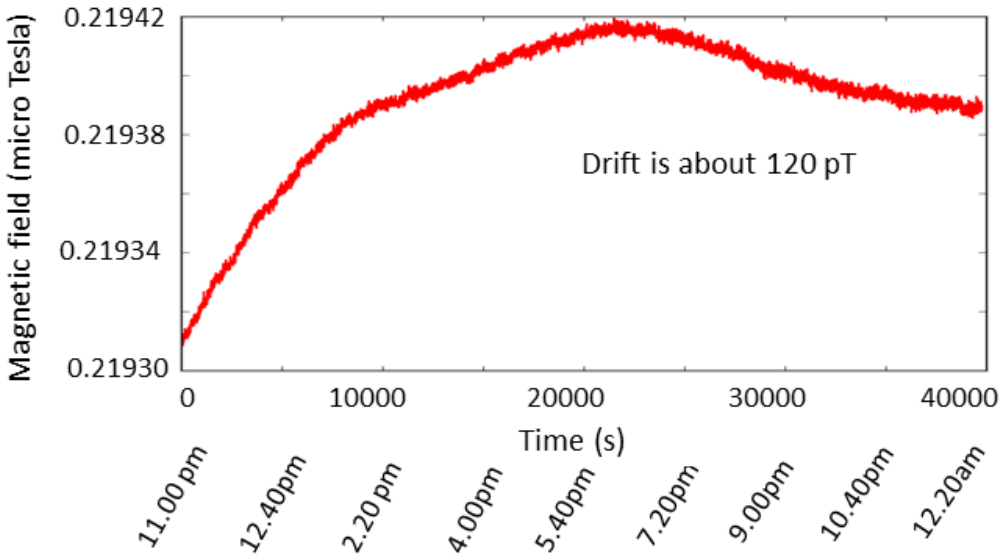

Figure 5.13: Magnetic field recorded over 12 hours. In this measurement the observed field drift is about 120 pT.

causing any frequency drift or not.

We suspected the tune might be drifting because we use a polarizing beamsplitter cube in our DAVLL system which may possess poor stability over long time periods [51].

In order to test the hypothesis that the frequency of the laser might be drifting, I did a study where I manually adjusted the frequency of laser light to maximize optical rotation. The DAVLL and Digilock system were not used to lock the laser during this study. Rather, periodically, the data acquisition was paused, and the laser frequency was adjusted manually to maintain the same (largest) differential photodiode amplitude. The data acquisition was then restarted.

The results of the measurement are shown in Fig. 5.14. Fig. 5.14b shows the fitted initial amplitude (after the pump beam has been switched off) as determined by the fit to the decaying oscillating function. The spikes in Fig. 5.14b indicate times when the retuning of the laser was conducted, as described above. A time jump (not shown) of a random by relatively short interval also occurs for each retuning, which is not shown.

Fig. 5.14a shows the result of the frequency measurement, when translated into magnetic

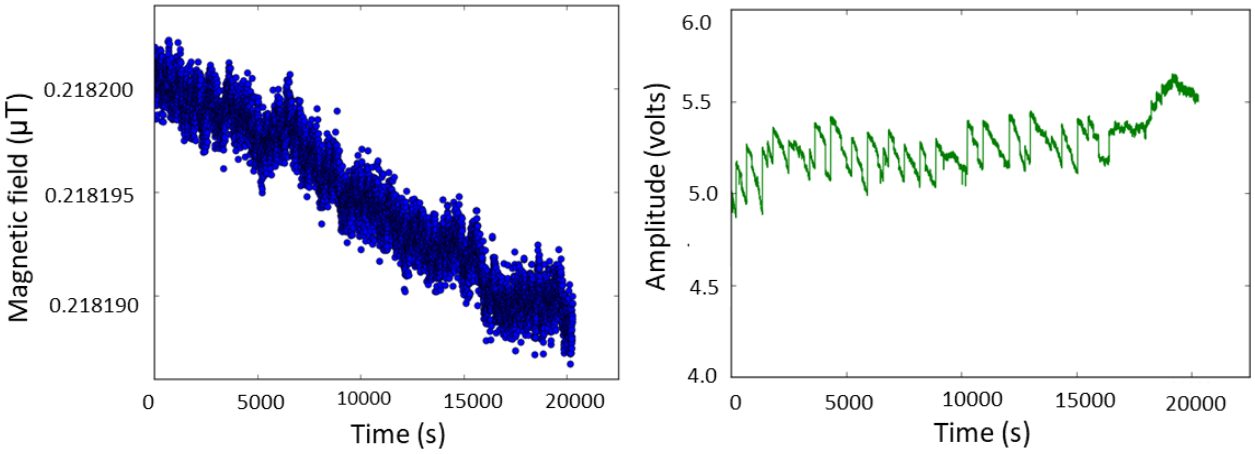

(a) (b)

Figure 5.14: (a) magnetic field vs. time. (b) Amplitude of recorded FID NMOR signal over 20000 s. During this study laser tuning is maintained manually, as can be seen from the jumps in the amplitude which occur upon retuning.

field. It can be seen that as the amplitude of the fit decreases (presumably due to a drift in the laser frequency), the statistical fluctuations in the field measurement increase. This would be expected because a small fit amplitude will make the frequency statistically more difficult to measure.

Clearly the field measurement in Fig. 5.14a does not drift in the same way as the FID amplitude in Fig. 5.14b. Thus we conclude that the field measurement in FID mode is relatively insensitive to the frequency tuning of the laser, except that if the tune drifts, the frequency measurement becomes statistically less precise.

5.7 Improving the precision of individual FIDs, and problems encountered in doing so

5.7.1 Optimization of pump and probe beam power

A study has been performed to determine how optimization of the pump and probe beam power effect on precise field measurement. During this study, the magnetometer has operated

Probe power (μW)	Coherence time (ms)	Amplitude (V)
2	84	2.13
5	82	2.11
10	68	4.06
15	59	5.8
35	32	10

Table 5.1: Single FID fit parameters as a function of probe beam power.

in FID mode.

In Fig. 5.15 the measured magnetic field has been displayed for two different probe beam power. Fig. 5.15a presents the measured field over 100 s with 15 μW probe power while Fig. 5.15b display the measured field over 100 s for probe power 30 μW. In both cases, the pump beam power the same ($\sim$ 40 μW). Each blue points in this graph represent a single FID scan. As can be seen from Fig. 5.15 the magnetic field were more scattered for high probe beam power. The standard deviation of the data was 7.2 pT for probe beam power 30 μW while for low beam power of 15 μW the standard deviation was 3.01 pT.

The apparently worse statistical precision for higher probe beam power can be traced in part to its effect on the individual FID signals of each measurement. Table 5.1 displays the coherence time of the FIDs for different probe power while the pump beam power was held constant (120 μW). For these settings, the coherence time is seen to increase for decreasing probe power, which acts to improve the statistical precision. However, it is counteracted by a corresponding decrease in the FID amplitude which acts to worsen the statistical precision. The trade off of these two effects must be considered when selecting the probe power for a given pump power. In general it is expected that a probe power in the μW range would be optimal.

The effect of pump beam power was also studied with the probe beam power ($\sim$ 15 μW) held constant. The pump beam power was changed by changing the duty cycle of the square wave modulation used for the AOM. When duty cycle is set to 5% the pump beam power is roughly 40 μW and for 16% duty cycle power is roughly 130 μW. During this measurement the lock-in reference frequency was set to 1943.9 Hz while the AOM frequency was 2036 Hz.

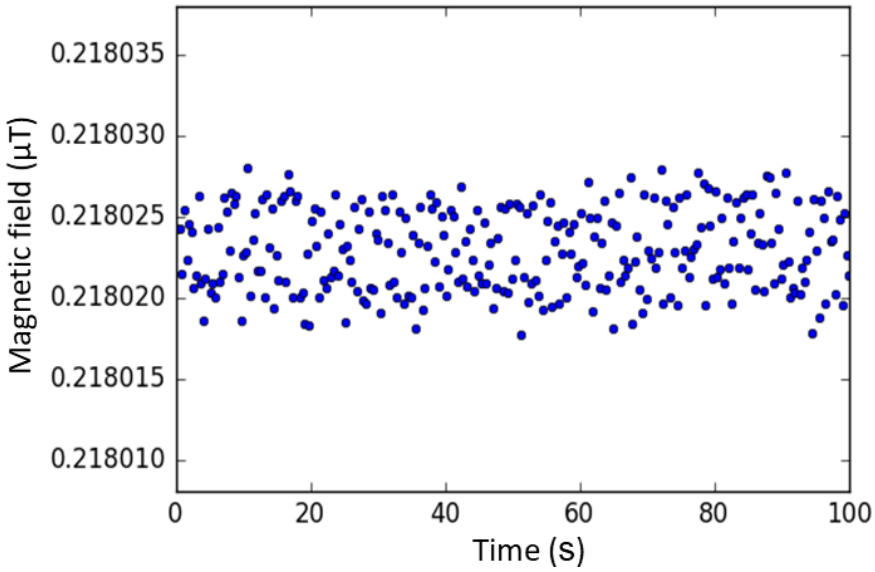

(a)

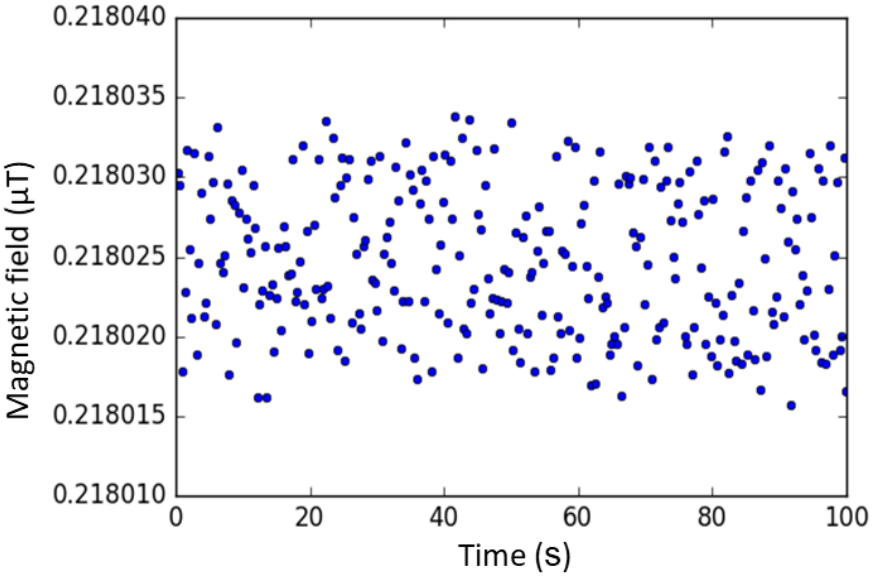

(b)

Figure 5.15: Magnetic field as a function of time for different power of probe beam: (a) 15 μW, the standard deviation of the data is 3.01 pT (b) 30 μW, the standard deviation is 7.2 pT.

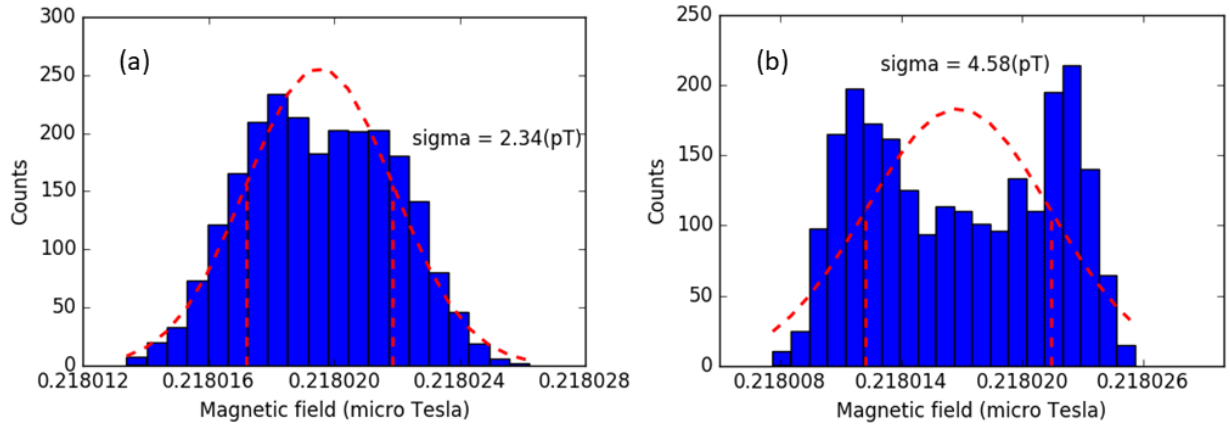

Figure 5.16: Magnetic field histograms for different pump beam duty cycles (a) 5% (b) 16%. Numbers written on the graph report the standard deviation of each distribution.

The histogram of measured magnetic field for two different pump beam powers is shown in Fig. 5.16. The standard deviation becomes larger for higher duty cycle while it becomes narrower for small duty cycle. It is clear from the plot that the data points are not statistically distributed.

It was observed very clearly during these studies that when a pump beam with a higher duty cycle was used, the FID amplitude increased until a saturation point. The data in Fig. 5.16(b) are close to this saturation point. But the problem of non-statistical behavior is also more apparent. So it can be concluded that using higher duty cycle is likely statistically more robust, revealing new systematic errors in field measurement which led to the next studies.

5.7.2 Reference frequency of lock-in amplifier and precision frequency measurement

The measurement technique of FID signal was discussed in Section 4.3. In order to capture the FID signal, the reference frequency of lock-in amplifier is normally set to $\sim$ 100 Hz apart from the resonance frequency. Also the lock-in time constant was set to 300 μs. Technically, this time constant too low. It admits frequency components beyond the reference frequency

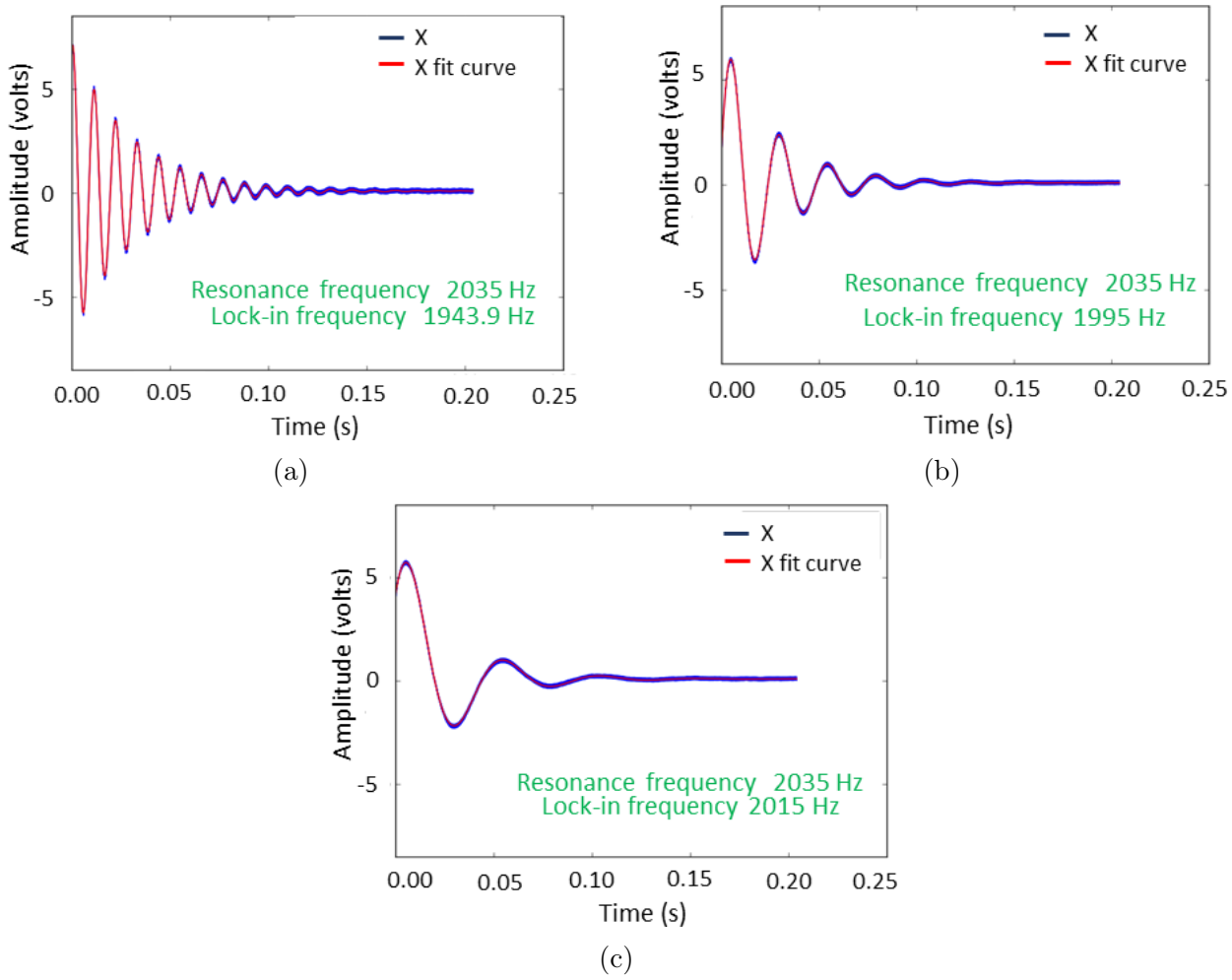

Figure 5.17: FID signal for different reference frequency settings of the lock-in amplifier, while the true magnetometer resonance frequency was roughly 2035 kHz (which was the AOM frequency setting) (a) lock-in reference frequency 1943.9 Hz (b) 1995 Hz, and (c) 2015 Hz.

which is typically 2000 Hz, if the magnetic field being measured is of order 0.2 μT. Because of the bimodal structure seen in Figs. 5.15 and 5.16, we began to suspect that some noise was creeping into the frequency measurement through the lock-in amplifier.

This led us to increase the lock-in time constant, which in turn led us to want to reduce the frequency difference between the lock-in reference frequency and the atoms.

The FID signal for different reference frequency of lock-in amplifier is shown in Fig. 5.17. The data are fitted in order to determine the frequency of oscillation. In this case the pump power was 60 μW and the probe power was 30 μW. We decided to study these settings in

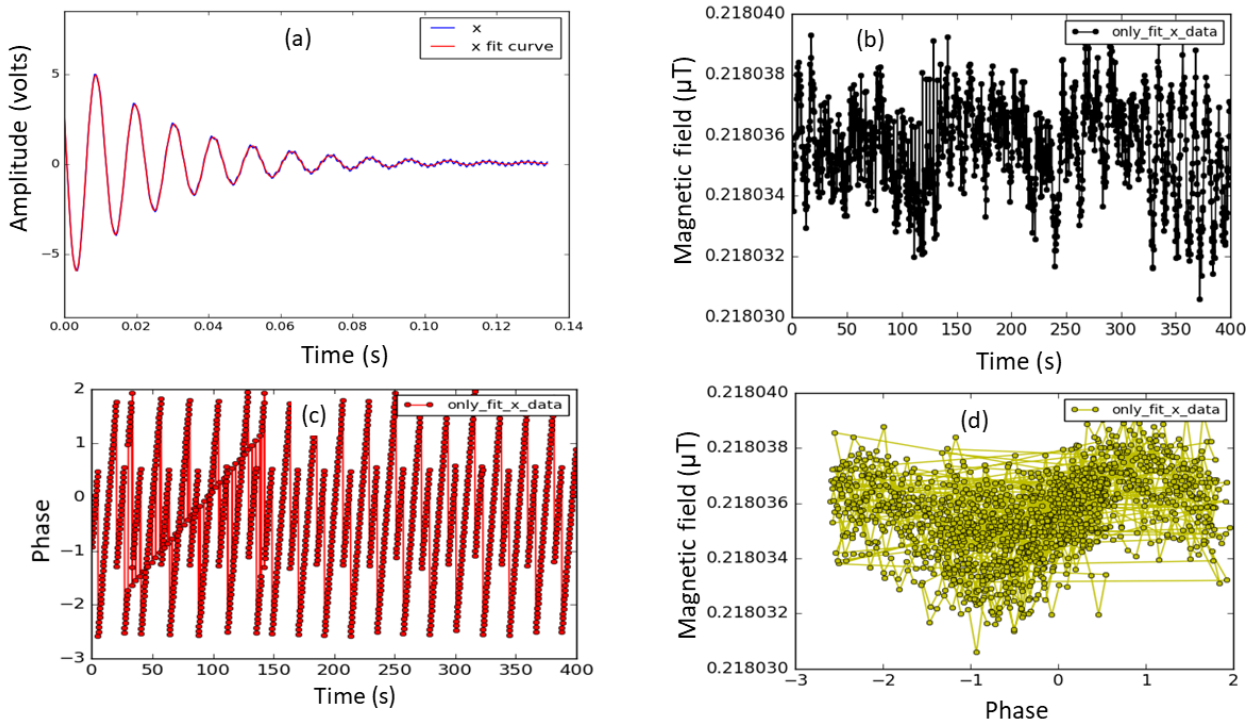

Figure 5.18: Lock-in reference frequency and time constant are 1943 Hz and 300 μs respectively. Only X data were fitted. (a) example of an FID and individual fit (b) frequency measurement translated to magnetic field (c) phase of fit (d) magnetic field vs. phase.

more detail.

Fig. 5.18 displays study over time of the 1943 Hz lock-in amplifier frequency setting. In the example FID in Fig. 5.18(a) some high frequency periodic noise can be seen. In Fig. 5.18(b) some non-statistical sinusoidal behavior can be seen. We eventually realized that this was correlated with the phase determined by the fit. The phase as a function of time is shown in Fig. 5.18(c). The correlation of field with phase is shown in Fig 5.18(d). An indication of correlation between field and phase can be seen here.

Clearly it is possible for the frequency to be pulled by the phase of the fit, given that the precision of the frequency fit is determined in part by the number of zero-crossings in the individual FID signals. The phase could certainly affect the number of zero crossings which are statistically relevant to the fit.

We decided to try to reduce the dependence on phase by fitting both the X and Y signals simultaneously. Fig. 5.19 shows this study. From Fig. 5.19(c), it can be seen that

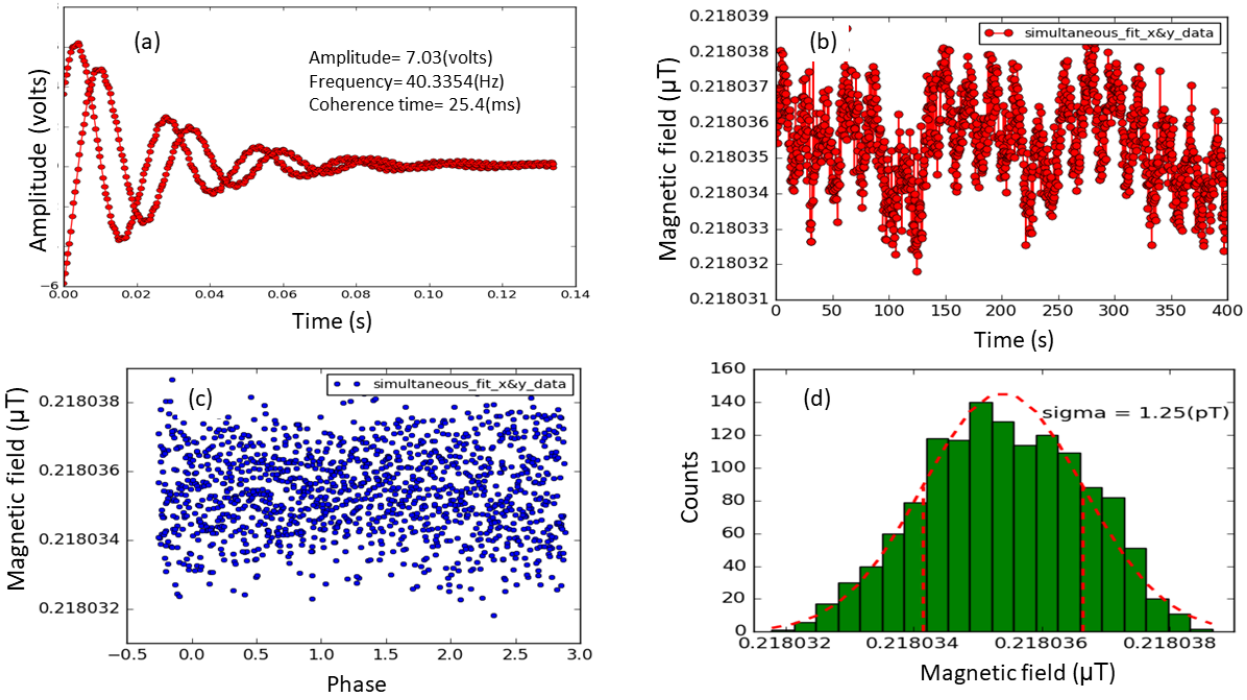

Figure 5.19: Lock-in reference frequency and time constant are 1943 Hz and 300 μs respectively. X and Y data were fitted simultaneously. (a) example of an FID and its fit (b) frequency measurement translated to magnetic field (c) magnetic field vs. phase determined by fit (d) histogram of field measurements.

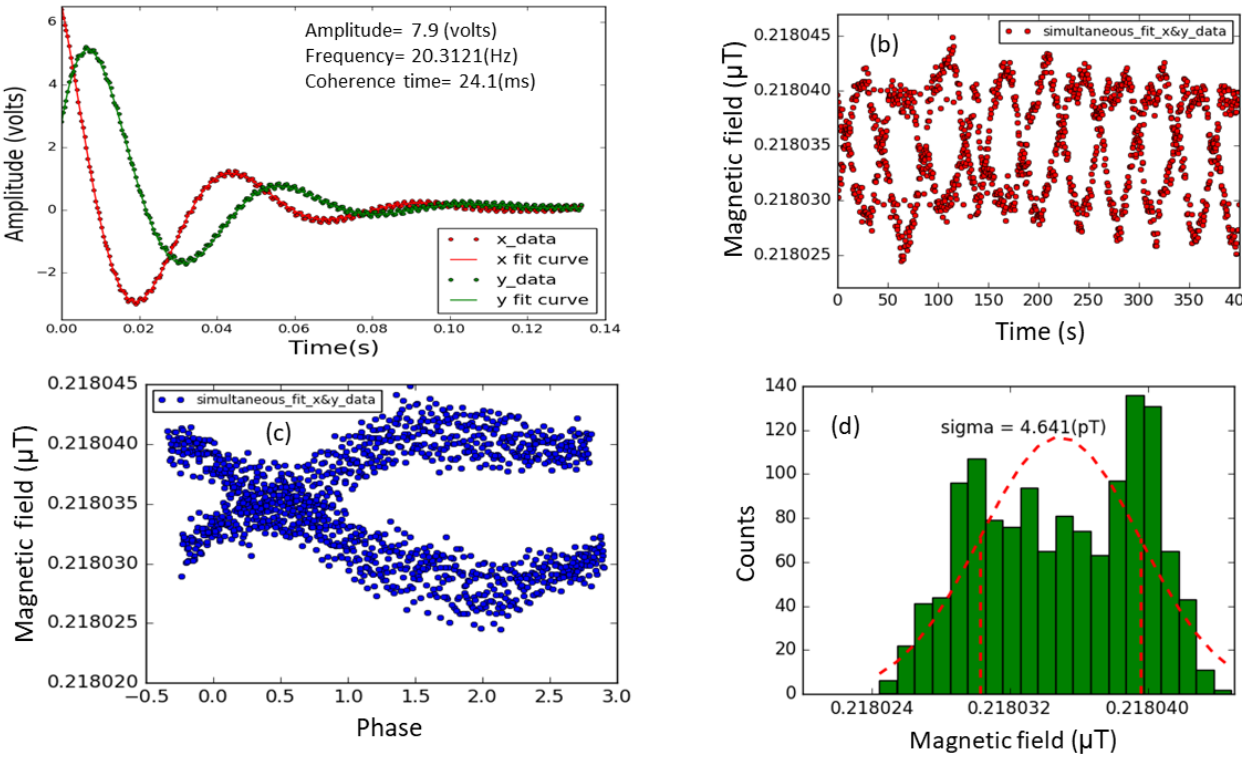

Figure 5.20: Lock-in reference frequency and time constant are 2015 Hz and 300 μs respectively. X and Y data were fitted simultaneously. (a) example of an FID and its fit (b) frequency measurement translated to magnetic field (c) magnetic field vs. phase determined by fit (d) histogram of field measurements.

the correlation of frequency with phase has been reduced significantly, so that the data look statistical when histogrammed, as is done in Fig. 5.19(d). But Fig. 5.19(b) still clearly shows that there is non-statistical behavior in the frequency (field) measurements. We though this might yet be due to the periodic high-frequency noise seen if Fig. 5.19(a). Based on this we decided to increase the lock-in time constant, and tried increasing the lock-in reference frequency to have more flexibility to change the time-constant.

In Fig. 5.20, the lock-in reference frequency has been changed to 2015 Hz, without yet changing the lock-in time constant. The interesting feature here is that, although the X and Y data are fitted simultaneously, there is a very clear phase dependence to the field measurements. The "best" choice of phase appears to be about 0.5 radians. It is not unexpected to have such a phase dependence, given that there are so few zero-crossings in the FID signal that can be used to constrain the frequency.

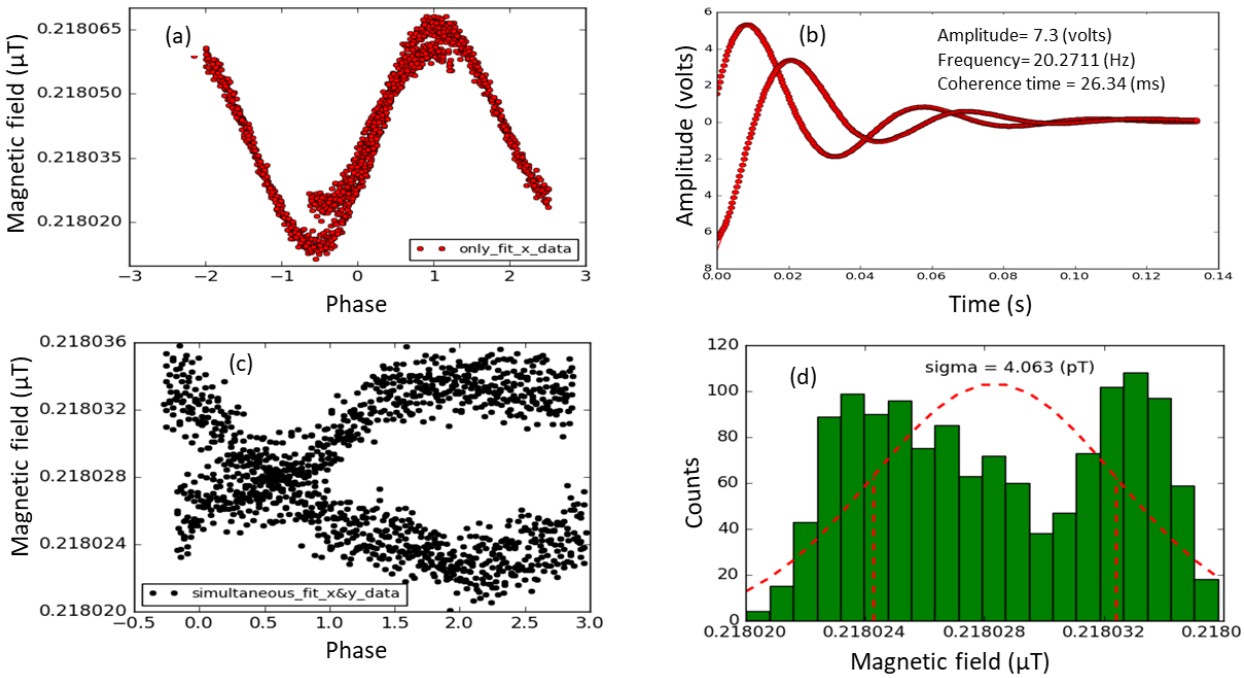

Figure 5.21: Lock-in reference frequency and time constant are 2015 Hz and 1 ms respectively. (a) frequency measurement determined by fit of X data only as a function of the phase also determined by that fit (b) example of an FID and its fit, where both X and Y data has been fitted simultaneously (c) magnetic field vs. phase determined by the simultaneously fitted X and Y data (d) histogram of field measurements arising from the simultaneous fit of the X and Y data.

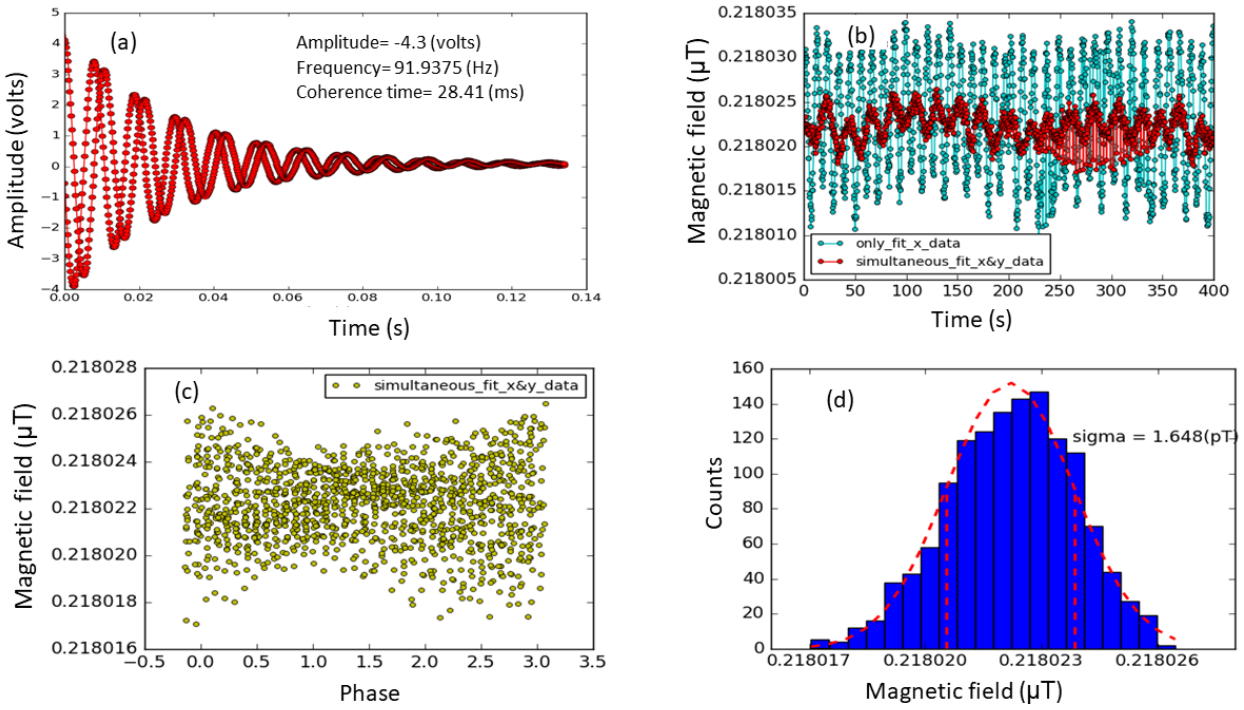

Figure 5.22: Lock-in reference frequency and time constant are 1943 Hz and 1 ms respectively (a) example of an FID and its simultaneous fit to the X and Y data (b) frequency measurement translated to magnetic field, in red are shown the results of the simultaneous fit to the X and Y data, in cyan are the results of the fit to the X data only (c) magnetic field vs. phase determined by the simultaneous fit to the X and Y data (d) histogram of field measurements for the simultaneously fitted X and Y data.

In Fig. 5.21, the lock-in reference frequency of 2015 Hz has been retained, but the lock-in time constant has now been increased to 1 ms. The same large phase dependence can be seen. Fig. 5.21(a) additionally shows the phase dependence of the fit to the X data only, which is even larger. Aside from the strong phase dependence, the data do appear to be non-statistical in nature.

In Fig. 5.22 the lock-in reference frequency has been set to 1943 Hz and the lock-in time constant to 1 ms. Compared with the 300 μs settings which were shown in Figs. 5.18 and 5.19, the phase dependence has been accentuated by the longer lock-in time constant. Another feature is that the amplitude of the fitted data has been reduced, seen particularly in Fig. 5.22(a).

The main conclusion of these studies was that the frequency fitting procedure is quite

sensitive to the lock-in time constant and frequency settings, which may induce errors if not adjusted carefully. These could give rise to additional systematic errors. This would be one of the main topics for further study in order to push the precision of the magnetometer to its limits. Generally these effects manifest themselves as fairly obvious nonstatistical behaviors in the data either as a function of time or when histogramming the field measurements. They also tend to become an issue with frequency measurements of precision below 1 Hz are made on each individual FID measurement.

It is also worth noting that all the above studies were done for a considerable larger probe power than the optimal low value. As a consequence the coherence times are rather short compared to the values used for most other studies in this thesis. The frequency measurements of the other studies are less affected by these phase effects as a result.

5.8 Tilted field measurements

In Section 4.3.1 we described magnetometer operations for tilted field, where we did not use the lock-in amplifier. We showed an example where the field was tilted in the yz-plane which is defined by the laser propagation direction (z) and the y-coil direction.

When the pump beam is modulated at $\Omega_m \approx \Omega_L$, the FID signal shows two frequency components: one near $2\Omega_L$ and one near Ω_L. The amplitude of these frequency components is sensitive to the tilt angle. One of them is the FFT of FID signal and the other one is the fit FID signal using

$$X(t) = A_1 e^{-t/\tau_1} \sin(\omega_1 t + \phi_1) + A_2 e^{-t/\tau_2} \sin(\omega_2 t + \phi_2) + C, \tag{5.1}$$

where $X(t)$ is the differential photodiode signal as a function of time, and A_1, A_2, ω_1, ω_2, ϕ_1, ϕ_2, τ_1, and τ_2 are fit parameters. A 10th order Infinite Impulse Response (IIR) Butterworth filter was used at times to reduce background noise from the signal [52].

Fig. 5.23 shows the FID signal for different tiled angle in two different tilt directions.

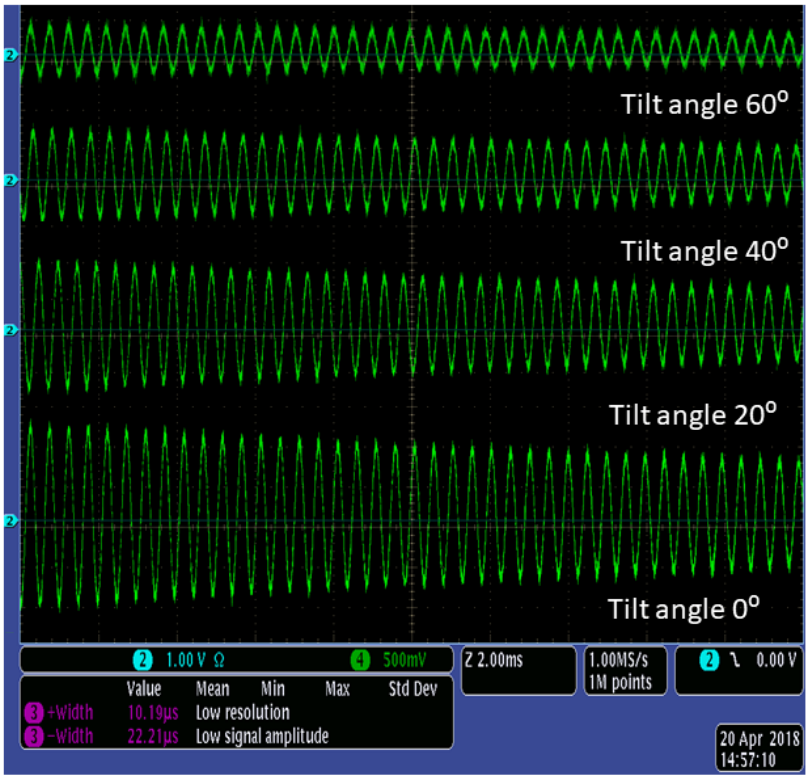

(a)

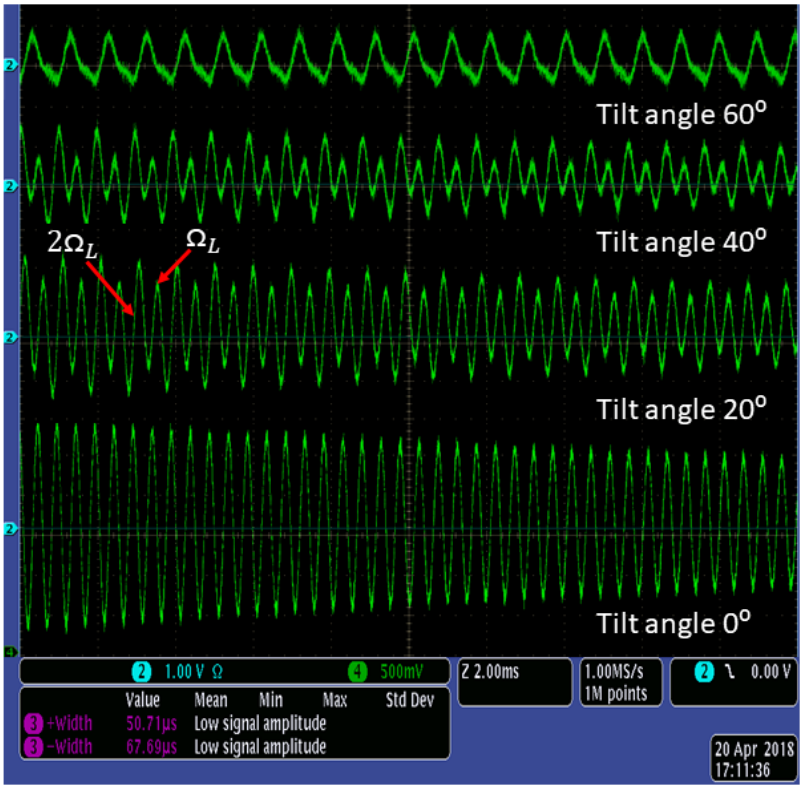

(b)

Figure 5.23: FID signal recorded for different tilt angles of the magnetic field in the (a) xy plane and (b) yz plane.

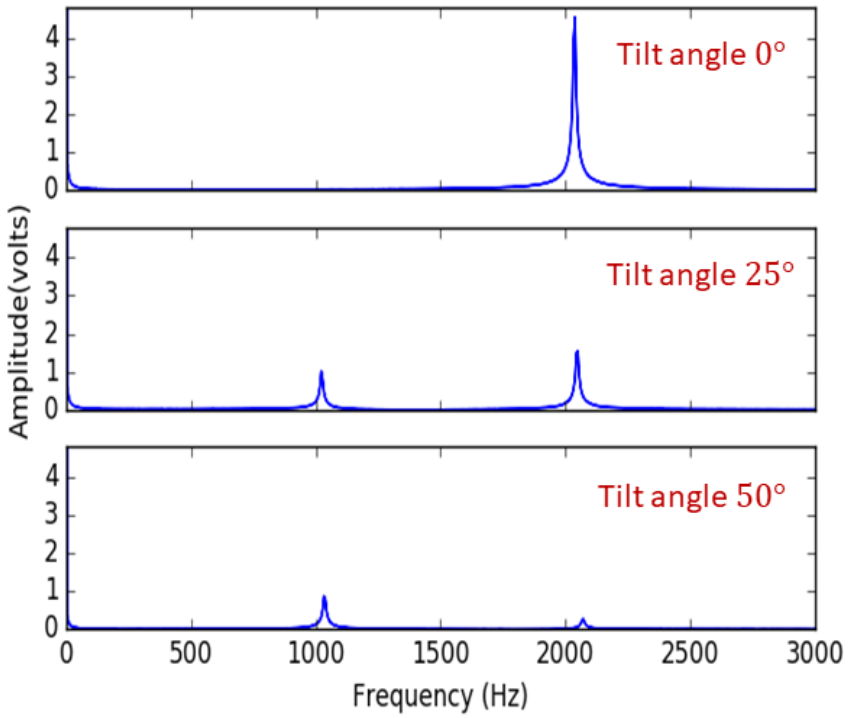

Figure 5.24: FFT of FID signal in the presence of transverse field after amplitude modulation at frequency $\Omega_m = 1019$ Hz. The topmost figure shows when the field is oriented along the z-axis (the axis of the laser beam path). The middle figure shows when the field has been oriented at a 25˚angle relative to the z-direction in the yz-plane. The bottom figure shows when the field has been oriented at a 50˚angle relative to the z-direction in the yz-plane.

When the magnetic field is tilted toward the polarization axis (y axis) an additional resonance appears at Ω_L (see figure 5.23b). The amplitude of this resonance becomes more pronounced with increasing the angle, while the amplitude of the resonance at $2\Omega_L$ decreases. When the magnetic field is tilted by more than 60Âř the amplitude of the resonance recorded at Ω_L also starts to decrease and reaches zero when the magnetic field is directed along the y axis.

Now when the magnetic field is tilted toward the plane perpendicular to the light polarization axis resonance appears only at $2\Omega_L$ (see figure 5.23a). The amplitude of this resonance decreases with increasing tilted angle.

Fig. 5.24 display the FFT of resonance signal for three different tilt angles of 0°, 25° and 50° in the yz-plane. It can be seen from the plot that at 0° tilt angle there is only one frequency component while for others two peaks correspond to two frequency components.

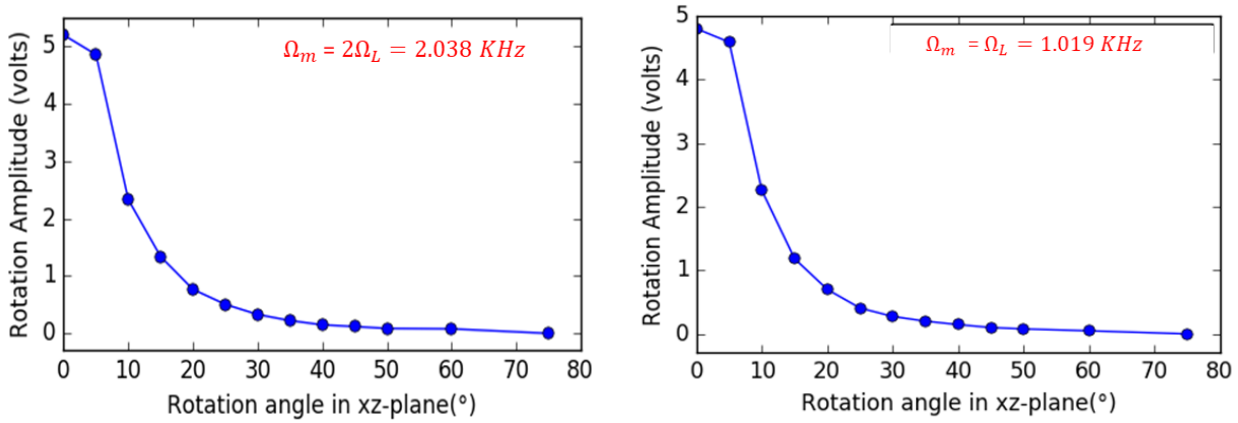

(a) (b)

Figure 5.25: The amplitude of the FID NMOR signals seen near $2\Omega_L$ as a function of tilt angle recorded at (a) $\Omega_m \approx \Omega_L$ and (b) $\Omega_m \approx 2\Omega_L$ vs. the tilt angle of the magnetic field in the plane defined by the light-polarization and light propagation vectors (xz-plane). The amplitude of the FID signal at Ω_L was small.

Fig. 5.25 shows the amplitude of the FID signal for the magnetic field tilted in the xz plane (which we assume means out of the polarization plane) at various angles to the light propagation direction at modulation frequencies $\Omega_m = 2\Omega_L$ and Ω_L. It can be seen from the figure that the amplitude of the FID signal decreases with increasing tilt angle for both modulation frequencies. It is dominated by a single frequency component near $2\Omega_L$.

Fig. 5.26(a) indicates the signal amplitude vs. different tilt angle at $\Omega_m = 2\Omega_L$. The amplitude of fitted FID signal at $2\Omega_L$ decreases as the angle between magnetic field and the light propagation direction increases.

Fig. 5.26(b) shows the FID amplitudes for a pumping frequency $\Omega_m = \Omega_L$. The FID at $2\Omega_L$ decreases with increasing tilt angle in yz-plane, while the FID amplitude at Ω_L increases till 30° and after that the amplitude starts to decrease, but still dominates over the signal at $2\Omega_L$. For both cases (Fig. 5.25 and Fig. 5.26) the signal amplitude has been extracted as a fit parameter when data was fitted to the fit function 5.1

Figs. 5.27 and 5.28 show examples of the quality of fit for unfiltered data, and the quality of the data after filtering respectively.

The conclusion is that pumping at $\Omega_m = \Omega_L$ followed by detection of the FID at frequen-

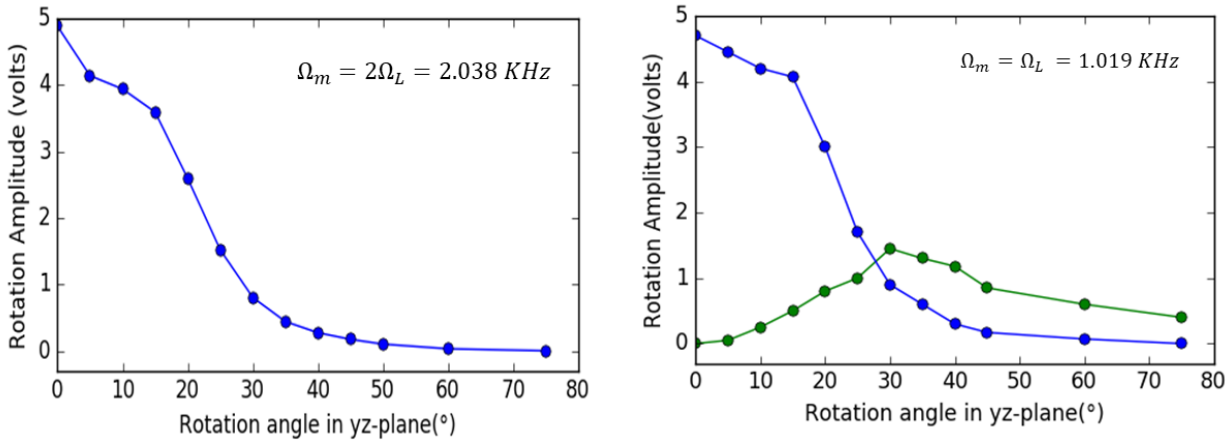

(a) (b)

Figure 5.26: The amplitude of the FID NMOR signal for pumping frequencies near (a) $\Omega_m = 2\Omega_L$ and (b) Ω_L vs. the tilt angle of the magnetic field in the plane defined by the light-polarization and light propagation vectors (yz-plane). For the data in (a), a single frequency component at $2\Omega_L$ tended to dominate, and the amplitude of this signal is shown. For the data in (b), two frequency components in the FID signal were seen. The amplitude of the signal at $2\Omega_L$ is shown in blue and the amplitude of the signal at Ω_L is shown in green.

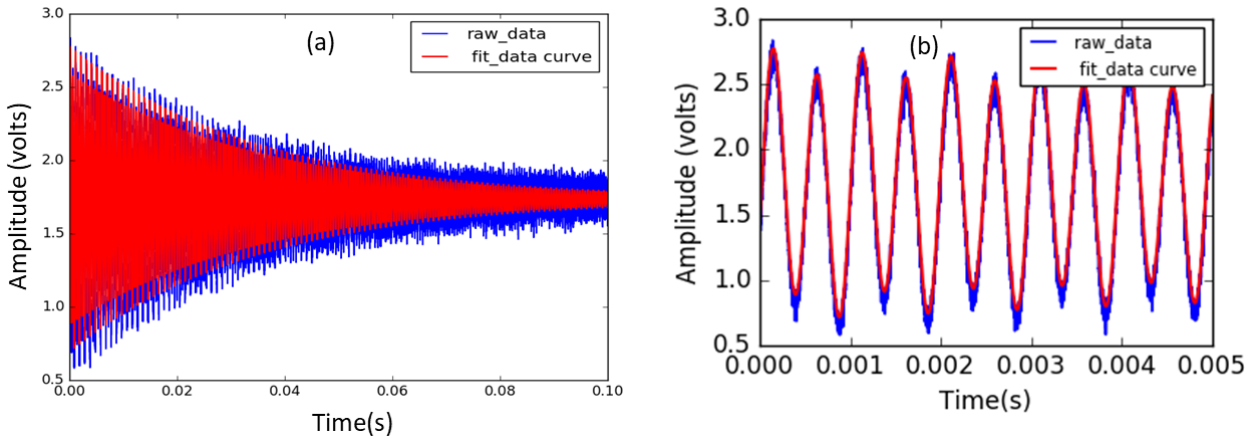

Figure 5.27: Fitted FID signal using Eq. 5.1. (b) The zoomed version of (a). The blue line indicates raw data while the red one indicates fitted curve.

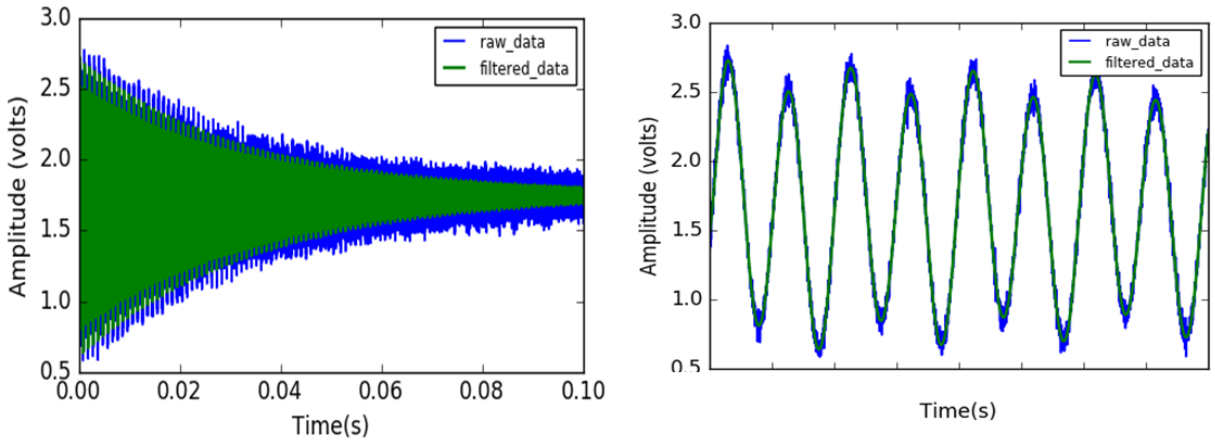

Figure 5.28: (a) Raw and filtered FID signal. (b) zoomed version of (a).

cies $2\Omega_L$ and Ω_L would allow detection of the field and its angle in the yz-plane simultaneously. While this is consistent with previous work in the literature, it represents the first use of FID measurements to make the deduction.

In the future, further improvements to the calibration of the measurements would be made in order to see whether how small a tilt angle could be measured. In the nEDM experiment, the field magnitude is 1 μT, and if this magnetometer could sense transverse fields at the 1 nT level, it would be a new application of such magnetometry techniques.

Chapter 6

Conclusion

6.1 Summary of Results of the Thesis

The study based on the adjustment of the pump and probe time discussed in Section 5.2 allowed us to measure the field faster. Previously each measurement cycle was about 1 s but now the optimized cycle time which include pump and probe time is about 0.35 s which allowed us to take the field measurement about 3 times faster.

In order to find out any correlation between coil current drift and magnetic field drift the stability of coil current further should be studied very carefully again now that the degaussing system seems to have improved. Fluctuations should be easily observable. Improvements to data acquisition system are easy and should be pursued. Larger changes in coil current were easily observable and seemed to agree with expectation based on the measured coil constant.

It can be concluded for the study discussed in Section 5.4 that magnetometer drift compared with drifts of temperature is $\lesssim 5$ pT/°C.

Studies regarding degaussing (Section 5.5), which in part tell the story of our degaussing development and learning.

From Section 5.5.1 it can be concluded that we set up the degaussing system and tested mainly sample rate (related to number of oscillations) stated to be important in Ref. [48].

We found that if the innermost shield was already degaussed that additional poor or rapid degaussing did not make the field quality as badly as we expected.

The conclusion of the study discussed in Section 5.5.2 regarding initial operations at non-zero field, and ramp field to large values, without degaussing the field drift was bad. After degaussing the direction of the field drift changed but the field was unstable about at the same level as before degaussing.

The conclusion of the another study, reported in Section 5.5.3, in which degaussing additionally all three outermost shields was done in an unoptimized system is that the field quality seemed to improve after degaussing. The field drift reduced by a factor of 4.

From the studies discussed in section 5.6 regarding laser locking and tuning, and the requirements on tune stability can be found that lock point or laser seems to drift over time, which could be due to the polarizing beam splitter cube used in the DAVLL system. A drift of about 120 pT was observed where statistical error gets worse. We demonstrated conclusively that this level of drift cannot be due to a drift in the tune of the laser by some additional studies where the tune was purposely varied. In order to understand whether the drift of lock points affects measured field another study has done by manual locking. We found that lock drift does not affect measured field drift very much, but does affect statistical precision of magnetometer.

The minimum in the Allan deviation of our Rb magnetometer occurs at 300 fT after 10 s of averaging. The result is comparable to the sensitivity of Cs magnetometer of PSI nEDM group.

Studies attempting to push below 1 pT in an individual FID measurement by adjusting pump and probe powers and lock-in amplifier settings. This includes adjustment of the pump and probe powers, and lock-in amplifier settings. This study revealed problems in the procedures used to determine the precession frequency at high precision and suggests avenues for further study.

Future work is to finalize these studies in order to further reduce the errors. Finally,

I showed my studies which revealed a way to use FID mode to measure transverse fields. Further work is required to push to nT scale transverse fields relevant for nEDM experiments.

6.2 Recommended future work for the Rb magnetometer studies

A finite element analysis simulation of the z-coil in the current configuration should be carried out. The homogeneity of z-coil in this shielding configuration is not measured with endcaps of innermost shield removed. Coupling to second to innermost shield is also believed to be a problem and the degree of coupling could be calculated in such a simulation.

The homogeneity measurement of z-coil in shield has been done before with basic degaussing system which is slightly different than our present degaussing system. A further study could be done to measure homogeneity of this z-coil with our present degaussing system.

Study magnetometer performance with self-shielded coil inside the shield instead of our present z-coil. The idea is to study whether decoupling the coil from the shield has any impact on long-term stability.

The data fitting procedure of field measurement shows a sensitivity to the lock-in time constant and reference frequency which has been discussed in Section 5.7. In the future removing the lock-in amplifier from data acquisition system of field measurement could be a better idea for avoiding such systematic error. The signal could be collected directly from photodiode and use digital and/or analogue filters for further data analysis instead of demodulating the FID signal through lock-in amplifier.

For nEDM experiment, the operated magnetic field is 1 μT and if our magnetometer could sense transverse field in the range of 1 nT, it would be a new application of such magnetometry techniques. So another important future study could be done to find out how precisely the transverse field measurement can be done with this magnetometry system.

6.3 Farther future: implementation in the nEDM experiment at TRIUMF

The work presented in this thesis is based on measuring magnetic field stability and homogeneities which is a part of the TUCAN's future nEDM measurement at TRIUMF. Measuring nEDM within the sensitivity level of 10^{-27} e·cm is the goal for this experiment. Study magnetic field stability is very crucial in order to avoid systematic effects (discussed in Chapter 1) in nEDM experiment.

A fiber-coupled multiple magnetometer system will be implemented into the nEDM system, which is based on this work. It will lead to a determination of both field stability and gradients to the required levels.

Appendix A

Calculation of Allan deviation

Suppose a time series of measurements y_i is acquired at times ti for $i = 1, ..., M$ [53]. Normally data are acquired for even time steps $t_{i+1} - t_i = \Delta t$. Consider a subset of N data points. Now we can write,

$$\bar{y}_1 = \sum_{i=1}^{N} \frac{y_i}{N} \tag{A.1}$$

For the next N data points an average can be written as

$$\bar{y}_2 = \sum_{i=N+1}^{2N} \frac{y_i}{N} \tag{A.2}$$

or, in general,

$$\bar{y}_n = \sum_{i=(n-1)N+1}^{nN} \frac{y_i}{N} \tag{A.3}$$

The Allan deviation can be express as

$$\sigma_y(\tau) = \sqrt{\sigma_y^2(\tau)} = Var_y(\tau) \tag{A.4}$$

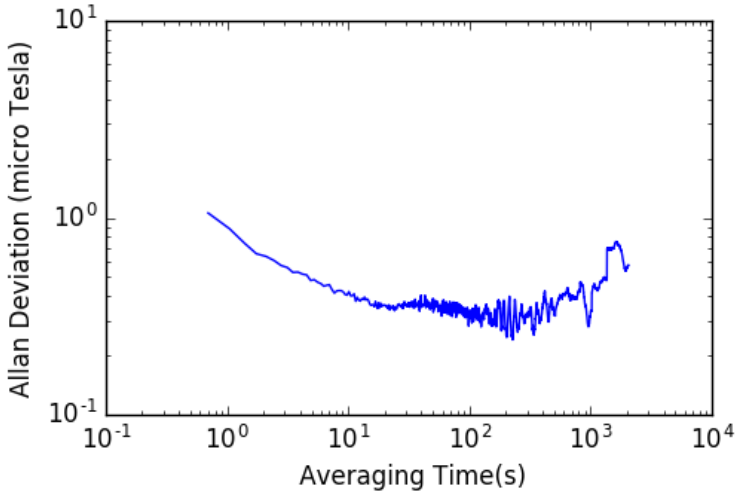

Figure A.1: Allan deviation vs. averaging time(s)

Where σ_y is the Allan deviation, τ the time of each frequency estimate and Var_y is the variance of the observed data points.

$$\sigma_y^2(\tau) = \frac{1}{2}(\bar{y}_{n+1} - \bar{y}_n) \tag{A.5}$$

where $\bar{y}_n$ is the fractional frequency average over the observation time τ. Allan deviation formula for sinusoidal waveform: Suppose

$$y(t) = A\cos(\omega t + \phi) \tag{A.6}$$

The average of this function over a time-interval is

$$\bar{y}_n = \frac{2A}{\tau\omega} cos(\omega(t_n + \frac{\tau}{2}) + \phi) sin(\frac{\omega\tau}{2}) \tag{A.7}$$

and

$$\bar{y}_{n+1} = \frac{2A}{\tau\omega} cos(\omega(t_{n+1} + \frac{\tau}{2}) + \phi) sin(\frac{\omega\tau}{2}) \tag{A.8}$$

Now from equation(5.5) and (5.6) we can write

$$\bar{y}_{n+1} - \bar{y}_n = \frac{2A}{\tau\omega} sin(\frac{\omega\tau}{2})[cos(\omega(t_{n+1} + \frac{\tau}{2}) + \phi) - cos(\omega(t_n + \frac{\tau}{2}) + \phi)] \tag{A.9}$$

Thus Allan deviation can be written as

$$\sigma_y^2(\tau) = \frac{1}{2}(\bar{y}_{n+1} - \bar{y}_n) = (\frac{4A}{\tau\omega} sin^2(\frac{\omega\tau}{2}))^2 \sin^2(\frac{\omega(t_{n+1} + t_n + \tau)}{2}) + \phi) \tag{A.10}$$

For a large number of randomly distributed tk the average of the sine-squared function is

$$\sin^2(\frac{\omega(t_{n+1} + t_n + \tau)}{2}) + \phi) = \frac{1}{2} \tag{A.11}$$

We therefore find that

$$\sigma_y^2(\tau) = (\frac{2A}{\tau\omega} sin^2(\frac{\omega\tau}{2}))^2 \tag{A.12}$$

In FID mode, the resonance signal looks like a decaying sine wave. By fitting the NMOR signal with a damped sine wave the oscillation frequency has been extracted and finally this oscillation frequency has been translated to field.The Allan deviation of the measure field has been plotted in Figure 5.23.

Bibliography

[1]M. D. Schwartz, "Quantum Field Theory and the Standard Model", (2013).

[2]M. Kobayashi and T. Maskawa, "Cp-violation in the renormalizable theory of weak interaction", Progress of Theoretical Physics **49**, 652–657 (1973).

[3]C. A. Baker, D. D. Doyle, P. Geltenbort, K. Green, M. G. D. van der Grinten, P. G. Harris, P. Iaydjiev, S. N. Ivanov, D. J. R. May, J. M. Pendlebury, J. D. Richardson, D. Shiers, and K. F. Smith, "Improved experimental limit on the electric dipole moment of the neutron", Phys. Rev. Lett. **97**, 131801 (2006).

[4]J. M. Pendlebury, S. Afach, N. J. Ayres, C. A. Baker, G. Ban, G. Bison, K. Bodek, M. Burghoff, P. Geltenbort, K. Green, W. C. Griffith, M. van der Grinten, Z. D. Gruji ć, P. G. Harris, V. Hélaine, P. Iaydjiev, S. N. Ivanov, M. Kasprzak, Y. Kermaidic, K. Kirch, H.-C. Koch, S. Komposch, A. Kozela, J. Krempel, B. Lauss, T. Lefort, Y. Lemière, D. J. R. May, M. Musgrave, O. Naviliat-Cuncic, F. M. Piegsa, G. Pignol, P. N. Prashanth, G. Quéméner, M. Rawlik, D. Rebreyend, J. D. Richardson, D. Ries, S. Roccia, D. Rozpedzik, A. Schnabel, P. Schmidt-Wellenburg, N. Severijns, D. Shiers, J. A. Thorne, A. Weis, O. J. Winston, E. Wursten, J. Zejma, and G. Zsigmond, "Revised experimental upper limit on the electric dipole moment of the neutron", Phys. Rev. D **92**, 092003 (2015).

[5]T. Chupp, P. Fierlinger, M. Ramsey-Musolf, and J. Singh, "Electric Dipole Moments of the Atoms, Molecules, Nuclei and Particles", (2017).

[6]N. Cabibbo, "Unitary symmetry and leptonic decays", Phys. Rev. Lett. **10**, 531–533 (1963).

[7]M. Pospelov and A. Ritz, "Electric dipole moments as probes of new physics", Annals Phys. **318**, 119–169 (2005).

[8]D. E. Morrissey and M. J. Ramsey-Musolf, "Electroweak baryogenesis", New J. Phys. **14**, 125003 (2012).

[9]E. Kolb and M. S. Turner, "The early universe", Front. Phys., Vol. 69, **-1** (1983) 10.1038/294521a0.

[10]A. D. Sakharov, "Violation of CP Invariance, C asymmetry, and baryon asymmetry of the universe", Pisma Zh. Eksp. Teor. Fiz. **5**, [Usp. Fiz. Nauk161,no.5,61(1991)], 32–35 (1967).

[11]N. F. Ramsey, "A molecular beam resonance method with separated oscillating fields", Phys. Rev. **78**, 695–699 (1950).

[12]M. L. Lang, *Development of active magnetic shielding for the neutron electric dipole moment experiment at triumf*, https://mspace.lib.umanitoba.ca/xmlui/handle/1993/23223, Jan. 2014.

[13]K. Green, P. G. Harris, P. Iaydjiev, D. J. R. May, J. M. Pendlebury, K. F. Smith, M. van der Grinten, P. Geltenbort, and S. Ivanov, "Performance of an atomic mercury magnetometer in the neutron EDM experiment", Nucl. Instrum. Meth. **A404**, 381–393 (1998).

[14]G. Ban et al., "Demonstration of sensitivity increase in mercury free-spin-precession magnetometers due to laser-based readout for neutron electric dipole moment searches", Nucl. Instrum. Meth. **A896**, 129–138 (2018).

[15]J. M. Pendlebury, W. Heil, Y. Sobolev, P. G. Harris, J. D. Richardson, R. J. Baskin, D. D. Doyle, P. Geltenbort, K. Green, M. G. D. van der Grinten, P. S. Iaydjiev, S. N. Ivanov, D. J. R. May, and K. F. Smith, "Geometric-phase-induced false electric dipole moment signals for particles in traps", Phys. Rev. A **70**, 032102 (2004).

[16]F. Bloch and A. Siegert, "Magnetic resonance for nonrotating fields", Phys. Rev. **57**, 522–527 (1940).

[17]S. Afach et al., "A measurement of the neutron to ^{199}Hg magnetic moment ratio", Phys. Lett. **B739**, 128–132 (2014).

[18]T. Hayamizu, *Xe/hg dual-comagnetometer for the triumf neutron edm experiment*, presented at nEDM2017 Conference, 2017.

[19]S. Afach, C. A. Baker, G. Ban, G. Bison, K. Bodek, Z. Chowdhuri, M. Daum, M. Fertl, B. Franke, P. Geltenbort, K. Green, M. G. D. van der Grinten, Z. Grujic, P. G. Harris, W. Heil, V. Hélaine, R. Henneck, M. Horras, P. Iaydjiev, S. N. Ivanov, M. Kasprzak, Y. Kermaïdic, K. Kirch, P. Knowles, H.-C. Koch, S. Komposch, A. Kozela, J. Krempel, B. Lauss, T. Lefort, Y. Lemière, A. Mtchedlishvili, O. Naviliat-Cuncic, J. M. Pendlebury, F. M. Piegsa, G. Pignol, P. N. Prashant, G. Quéméner, D. Rebreyend, D. Ries, S. Roccia, P. Schmidt-Wellenburg, N. Severijns, A. Weis, E. Wursten, G. Wyszynski, J. Zejma, J. Zenner, and G. Zsigmond, "Measurement of a false electric dipole moment signal from ^{199}Hg atoms exposed to an inhomogeneous magnetic field", European Physical Journal D (2015).

[20]J. Martin, R. Mammei, W. Klassen, C. Cerasani, T. Andalib, C. Bidinosti, M. Lang, and D. Ostapchuk, "Large magnetic shielding factor measured by nonlinear magneto-optical rotation", Nuclear Instruments and Methods in Physics Research Section A: Accelerators, Spectrometers, Detectors and Associated Equipment (2015).

[21]M. Sturm, "Measurements and characterization of a laser-based cs-atomic magnetometer", MA thesis (Oct. 2013).

[22]S. Groeger, G. Bison, J.-L. Schenker, R. Wynands, and A. Weis, "A high-sensitivity laser-pumped mx magnetometer", The European Physical Journal D - Atomic, Molecular, Optical and Plasma Physics **38** (2006).

[23]D. A. Steck, *Rubidium 87 d line data*, `https://steck.us/alkalidata/rubidium87numbers.1.6.pdf`, Sept. 2001.

[24]S.-K. L. V. V. Yashchuk and E. Paperno, *Magnetic shielding*, `http://www.ee.bgu.ac.il`.

[25]D. Budker and D. Kimball, *Optical magnetometry*, Optical Magnetometry (2013).

[26]D. Budker, D. J. Orlando, and V. Yashchuk, "Nonlinear laser spectroscopy and magneto-optics", American Journal of Physics **67**, 584–592 (1999).

[27]D. Budker, W. Gawlik, D. F. J. Kimball, S. M. Rochester, and V. V. Yashchuk, "Jun 2002 resonant nonlinear magneto-optical effects in atoms", in (2002).

[28]D. Budker, D. F. Kimball, S. Rochester, V. Yashchuk, and M. Zolotorev, "Sensitive magnetometry based on nonlinear magneto-optical rotation", **55** (2000).

[29]D. Budker, V. Yashchuk, and M. Zolotorev, "Nonlinear magneto-optic effects with ultranarrow widths", Phys. Rev. Lett. **81**, 5788–5791 (1998).

[30]D. Budker, D. F. Kimball, V. Yashchuk, and M. Zolotorev, "Nonlinear magneto-optical rotation with frequency-modulated light", **65** (2002).

[31]D. F. J. Kimball, L. R. Jacome, S. Guttikonda, E. J. Bahr, and L. F. Chan, "Magnetometric sensitivity optimization for nonlinear optical rotation with frequency-modulated light: rubidium d2 line", Journal of Applied Physics **106** (2009).

[32]S. Pustelny, A. Wojciechowski, M. Gring, M. Kotyrba, J. Zachorowski, and G. Wojciech, "Magnetometry based on nonlinear magneto-optical rotation with amplitude-modulated light", **103** (2007).

[33]S. Pustelny, A. Wojciechowski, M. Kotyrba, K. Sycza, J. Zachorowski, G. Wojciech, A. Cingoz, N. Leefer, J. Higbie, E. Corsini, M. Ledbetter, S. Rochester, A. O. Sushkov, and D. Budker, "All-optical atomic magnetometers based on nonlinear magneto-optical rotation with amplitude modulated light", **6604** (2006).

[34]B. Patton, E. Zhivun, D. C. Hovde, and D. Budker, "All-optical vector atomic magnetometer", Phys. Rev. Lett. **113**, 013001 (2014).

[35]D. Budker, D. F. Kimball, S. M. Rochester, V. V. Yashchuk, and M. Zolotorev, "Sensitive magnetometry based on nonlinear magneto-optical rotation", Phys. Rev. A **62**, 043403 (2000).

[36]J. M. Higbie, E. Corsini, and D. Budker, "Robust, high-speed, all-optical atomic magnetometer", Review of Scientific Instruments **77**, 113106 (2006).

[37]A. L. Bloom, "Principles of operation of the rubidium vapormagnetometer", Appl. Opt. **1**, 61–68 (1962).

[38]S. Pustelny, W. Gawlik, S. M. Rochester, D. F. J. Kimball, V. V. Yashchuk, and D. Budker, "Nonlinear magneto-optical rotation with modulated light in tilted magnetic fields", Phys. Rev. A **74** (2006).

[39]J. W. Martin, R. R. Mammei, W. Klassen, C. Cerasani, T. Andalib, C. P. Bidinosti, M. Lang, and D. Ostapchuk, "Large Magnetic Shielding Factor Measured by Nonlinear Magneto-optical Rotation", Nucl. Instrum. Meth. **A778** (2015).

[40]T. P. AG, *Dl 100 grating stabilized diode laser head manual*, `http://www.toptica.com`.

[41]C. Lee, G. Z. Iwata, E. Corsini, J. M. Higbie, S. Knappe, M. P. Ledbetter, and D. Budker, "Small-sized dichroic atomic vapor laser lock", Review of Scientific Instruments **82**, 043107 (2011).

[42]T. photonics, *Digilock basic locking*, 2011.

[43]T. P. AG, *Digilock 110 feedback controlyzer manual*, `http://www.toptica.com`.

[44]M. T. Graf, D. F. Kimball, S. M. Rochester, K. Kerner, C. Wong, D. Budker, E. B. Alexandrov, M. V. Balabas, and V. V. Yashchuk, "Relaxation of atomic polarization in paraffin-coated cesium vapor cells", Phys. Rev. A **72**, 023401 (2005).

[45]M. V. Balabas, K. Jensen, W. Wasilewski, H. Krauter, L. S. Madsen, J. H. Müller, T. Fernholz, and E. S. Polzik, "High quality anti-relaxation coating material for alkali atom vapor cells", Opt. Express **18** (2010).

[46]M. A. Bouchiat and J. Brossel, "Relaxation of optically pumped rb atoms on paraffin-coated walls", Phys. Rev. **147**, 41–54 (1966).

[47]P. D. D. Schwindt, L. Hollberg, and J. Kitching, "Self-oscillating rubidium magnetometer using nonlinear magneto-optical rotation", Review of Scientific Instruments **76**, 126103 (2005).

[48]F. Thiel, A. Schnabel, S. Knappe-Grfffdfffdneberg, D. Stollfufffdfffd, and M. Burghoff, "Demagnetization of magnetically shielded rooms", Review of Scientific Instruments **78**, 035106 (2007).

[49]H.Sanness Salmon, *Coercivity frequency dependence*, 2016.

[50]T. Andalib, J. W. Martin, C. P. Bidinosti, R. R. Mammei, B. Jamieson, M. Lang, and T. Kikawa, "Sensitivity of Fields Generated within Magnetically Shielded Volumes to Changes in Magnetic Permeability", Nucl. Instrum. Meth. **A867**, 139–147 (2017).

[51]P. C. Hobbs, *Building electro-optical system: making it all work* (2008).

[52]D. C. M. Ostapchuk, Private communication, July 2018.

[53]J. M. T. Andalib, *Allan deviation: denition and theoretical forms*, 2016.